

**A Theoretical and Experimental Study of the
Stability of Converging Cylindrical
Shock Waves**

Zubair Ahmad

A Thesis

in

The Department

of

Mechanical Engineering

**Presented in Partial Fulfillment of the Requirements
for the degree of Master of Engineering at
Concordia University
Montreal, Québec, Canada**

December 1984

© Zubair Ahmad, 1984

-1-

ABSTRACT

A Theoretical and Experimental Study of the
Stability of Converging Cylindrical Shock Waves

Zubair Ahmad

The stability of converging cylindrical shock waves is studied both theoretically and experimentally by placing cylindrical rods in their path and observing the behaviour of the shocks as they progress.

The theoretical analysis is based on Whitham's Ray-Shock theory and the well known Chester-Chisnell-Whitham's A-M relationship. Wave diagrams are constructed for various rod diameters to determine the growth or decay of perturbations, the shape of the shock as it progresses, the trajectories of the inner and outer triple points and the final shape of the shock before it collapses. Experimentally, the cylindrical shocks are produced in a 152 mm diameter shock tube using a three-element area contraction for turning the annular plane shock into a cylindrical one. For flow visualization, a double headed spark shadowgraph system is employed. For each cylindrical rod used, a series of photographs are taken of the converging shock to determine its shape and stability as it progresses.

Theoretically, the collapsing mechanism of converging cylindrical shocks is found to depend largely on the incoming shock

Mach number, and on the size of the rod used. The results obtained for strong shocks were completely different from that of weak shocks. In the former case, the perturbed shock collapses towards the rod side, whereas a weak shock collapses beyond the geometric centre. Smoothing of the shock front curvature is noted only at the outer triple points and in the case of strong shocks. An equation to determine the rate of growth of perturbation is developed as a function of the rod diameter and its distance from the centre. In the limit where the rod diameter is very small, the perturbation parameter is found to agree with the Butler's small perturbation analysis. Whereas, for large diameters, a good agreement is obtained between theoretical and experimental results.

ACKNOWLEDGEMENTS

The author wishes to express his gratitude and appreciation to his thesis supervisor, Dr. R.A. Neemeh for initiating this project and providing continued guidance and support throughout the investigation.

The author also extends his sincere appreciation to Dr. S. Chandrashekhar for his helpful suggestions and corrections in the improvement of the presentation.

I wish to thank Miss Jayne Claassen for typing the manuscript of this thesis, and my wife Shagufta, for her cooperation throughout this endeavor.

This work was supported by the National Sciences and Engineering Research Council under Grant No. A-4206.

TABLE OF CONTENTS

	<u>PAGE</u>
ABSTRACT	i
ACKNOWLEDGEMENTS	iii
TABLE OF CONTENTS	iv
NOMENCLATURE	vii
CHAPTER 1: INTRODUCTION	1
1.1 Production of Converging Shock Waves	2
1.2 Diffraction of Shock Waves	4
1.3 Stability of Shock Waves	6
1.4 Objective of the Present Work	8
CHAPTER 2: THEORETICAL DEVELOPMENT	10
2.1 Chester-Chisnell-Whitham's Area Mach Relationship	10
2.2 Ray Shock Theory	17
2.3 Reflection and Diffraction of Shock	24
2.4 Application of the Ray Shock Theory to Plane Corners	25
2.4.1 Concave Corners	26
2.4.2 Convex Corners	27
2.5 Application to Present Problem	28
2.6 Wave Diagrams and their Characteristics	34
2.6.1 Construction of Wave Diagrams	35
2.6.2 Practical Suggestions	40

	<u>PAGE</u>
CHAPTER 3: EXPERIMENTAL SET UP AND PROCEDURE	42
3.1 The Axisymmetric Shock Tube	43
3.2 The Test Section	45
3.3 Shadow Photography System	47
3.4 The Time-Delay Spark System	49
3.5 Secondary Units	50
3.6 Experimental Procedure	51
CHAPTER 4: RESULTS AND DISCUSSION	54
4.1 Behaviour of Converging Shocks without External Perturbation	54
4.2 An Experimental Study of Converging Shock-Rod Interaction	56
4.3 Flow Field Measurement	
4.3.1 Mach Number of the Shock in the Annular Part of the Test Section	58
4.3.2 Mach Number of Shock in the Cylindrical Chamber	59
4.4 Theoretical Analysis of Converging Cylindrical Shocks Subjected to External Perturbation	61
4.4.1 The Behaviour of Initially Strong Shocks	61
4.4.2 The Behaviour of Initially Weak Shocks	64
4.5 The Stability of Externally Perturbed Cylindrical Converging Shocks	65
4.6 The Collapsing Mechanism of Cylindrical Shock Waves	71
CHAPTER 5: CONCLUSIONS AND RECOMMENDATIONS	76

REFERENCES

PAGE

81

APPENDIX 'A'

86

FIGURES

89

TABLES

140

NOMENCLATURE

Latin Symbols

A	duct cross-sectional area
C	velocity of characteristics ($\frac{d\beta}{d\alpha}$)
C ⁺	positive characteristics
C ⁻	negative characteristics
CD	contact discontinuity
c	speed of sound
c ₀	speed of sound ahead of the shock
D	diameter of the converging shock
d	diameter of cylindrical rod
f ₁ , f ₂	arbitrary functions
f	body forces per unit mass
K	Chester function (equation 2.32)
M	Mach number
M _i	incident shock Mach number
M ₀	shock Mach number at a radius of 25 mm
MS	Mach stem
MR	Mach reflection
m	characteristic angle
n	5.073 [$\frac{2}{K(\infty)}$]
P	fluid pressure
P ₁	driven chamber pressure
P ₄	driver chamber pressure
R _s	shock radius
R ₀	distance between centre of rod and geometric centre

ΔR	radial distance of perturbed shock from its unperturbed shock front
RR	reflected shock
r	radius of cylindrical rod
s	specific entropy
T	temperature
TP	triple point
t	time
u	x-component of fluid velocity
v	y-component of fluid velocity
x	axial coordinate
y	transverse coordinate

Greek Symbols

α	ray-shock coordinate
β	ray-shock coordinate
γ	ratio of specific heats
δ	flow deflection angle
η	characteristic coordinate
θ	flow direction
θ_w	wedge angle
$\Delta\theta$	change in ray inclination
ϕ	incidence angle of shock
ψ	change in mass through walls per unit length
μ	defined by equation (2.29)
ξ	perturbation parameter

ρ fluid density
 λ Mach stem length
 χ shock-shock locus angle

Subscript

av average
h w.r.t. horizontal
o incident conditions (at 25 mm)
s shock wave
w wall

CHAPTER 1

INTRODUCTION

A great variety of physical and chemical processes can be studied in gases at high temperature. These processes are of interest in the study of their energy effects as well as, high velocity particle-collision which offers the possibility of attaining plasma [1].

The production of such high temperatures in gases by means of symmetrical collapse of converging shock waves has been under investigation for over three decades. Guderley [2] proved theoretically that the strength of the shock approaches infinity, as the radius of the converging shock tends to zero symmetrically. Since then, it has been the interest of many investigators to practically achieve such conditions. Since stable converging shocks collapse symmetrically at the center, it is of prime importance to analyse the stability of converging shocks under various magnitudes of perturbations. The opinions of the various investigators on the stability of converging shocks are contradictory. Lee and Knystautas [3] contend that converging shocks are stable, while Neemeh [4] and Butler [5] claim the opposite. Therefore, a clear and decisive answer to this problem is yet to be found.

This thesis presents a detailed analysis of the stability of converging shocks, perturbed externally by placing cylindrical rods in their path. Whitham's ray-shock theory is used in the present

investigation since it has been employed successfully by many investigators [6,7,8] to study the shock diffraction process and its behaviour in a variable-area duct. Finally, theoretical results are also verified by performing experiments.

The detailed description of the problem is presented later, following a brief review of the previous work done on the production, diffraction and stability of converging shocks.

1.1. Production of Converging Shock Waves

Cylindrical shocks were first studied theoretically by Guderley [2], who analysed their behaviour in a still ideal gas. He found that the shock strength grows infinitely as they approach the axis of the cylinder, and for $\gamma = 1.4$, the shock velocity increases inversely proportional as the 0.396 power of the shock radius. Thus, unbounded increase in shock strength, as the shock approaches to the point of convergence, is predicted by his idealized treatment. In a parallel investigation, a converging detonation wave was studied by Stanyukovich [9], where he derived the asymptotic law for the increase in pressure as $(r)^{-0.47}$ for cylindrical waves.

The simplest method to produce converging shocks was found experimentally by the detonation of gaseous mixture [10]. But the technical difficulties involved in producing safe and reproducible behaviour of shocks in the laboratory render this method impractical. These difficulties were overcome by an apparatus called 'shock tube'.

Perry and Kantrowitz [11,12] produced experimentally a converging cylindrical shock by deforming the plane shock produced in the shock tube, into a cylindrical one. They used 'Tear Drop' type prototype which was placed downstream of the axially symmetric shock tube as shown in Fig. (1.1). However, in their analysis only a 'Tear Drop' shape was considered. This work was extended by Laporte [13] and Chisnell [14], who studied the shock propagation in area contractions for two cases, namely the gradual and abrupt changes. But, Bird [15] showed in his work that not only area reduction but also the profile shape of the area contraction has an important effect on the shock strength near the point of convergence.

Milton [16] studied the effect of an area contraction on the strength of a converging shock and showed that the profile of the area contraction is a very important factor to achieve symmetrical cylindrical shocks. Neemeh [17] extended his work and studied in detail the shock wave propagation in various area contractions. A significant effect on the strength of a shock wave was observed by selecting a suitable area contraction. He designed 'three incremental area contraction' and employed it at the downstream-end of the shock tube to produce highly symmetrical converging cylindrical shocks.

In view of the results obtained by Neemeh using the 'three incremental area contraction', the experiments for the present work are carried out by the same area contraction.

1.2. Diffraction of Shock Wave

During the last forty years, considerable efforts have been directed towards the understanding of the shock diffraction problem.

In the early phase of the investigation, Taub and Bleakney [18] have exhaustively discussed the solutions of regular and Mach reflections for an ideal gas. These solutions however, are only limited to the vicinity of triple points. Bargman [19] found the solution for the entire flow field but his analysis is restricted to weak shocks. Lighthill [20] developed a theory for the motion of a shock wave at an expansion or compression corner. But his theory is valid for small deflections of the shock wave. This limitation led to search for alternate methods of solution to shock diffraction problems. Ludloff and Friedman [21] developed the numerical schemes and obtained equations of motion in a hyperbolic form which could easily be solved by the method of characteristics. These studies however, could not explain the transition from regular to Mach reflection. So Smith [22] performed experiments and concluded that regular reflection undergoes a transition to Mach reflection in a continuous manner and does not start immediately when the theoretical limit of regular reflection is exceeded.

Whitham [23] studied the shock wave motion problems by employing his own ray-shock theory. He found one equation relating the shock Mach number and ray tube area. The second relation between them is taken from Chester - Chisnell - Whitham (CCW) theory [24] for the motion of a shock wave down a tube of varying cross section. The

solution to the resulting hyperbolic equation is conveniently expressed by the method of characteristics. Later on, this theory was extended to three dimensions [25], and diffraction of shock by a cone was examined. The ray-shock theory has been employed successfully by Bryson and Gross [26] to predict the trajectories of triple points for the diffraction of plane shock by cylinder, cone and sphere at shock Mach number of the order of 3.

Skews [6] and Heiling [27] studied the shock diffraction experimentally and found that the ray shock theory agrees well with experiments for only strong shocks. Therefore, Itoh and Itaya [28] and Glass [29] modified the ray shock theory to study the transition from regular to Mach reflection in case of weak shocks. They found that if the wedge angle is kept constant, the shock-shock angle continues to increase as the Mach number approaches unity. However, at high Mach numbers this angle remains constant.

In the present investigation, the diffraction caused by the cylindrical rod takes place in weak and strong shocks. The locus of the triple points predicted by the ray shock theory does not agree well with the experimental values in the case of weak shocks as verified by Skews [6] and Henderson [7]. Therefore, the results plotted by Glass and Shirouzu [29] are used to find locus of triple points in case of weak shock.

1.3. Stability of Shock Waves

Generally, the stability of a system implies that small changes in the input, initial conditions or system parameters do not cause large intolerable changes in the system output [38]. This definition was employed by Kantrowitz [12] to define the stability of a plane cylindrical shock wave as the ability to approach perfect plane or cylindrical shape during its propagation, due to a gradual equalization of curvature between the neighbouring portions. Therefore, the ability of shock waves propagating into a stationary fluid to retain their shapes when subjected to small disturbances is defined as the stability. This is schematically represented for a shock reflected from a wavy wall in Fig. (1.2).

Most of the work done so far is on the stability of plane shocks. It has been shown by Freeman [31] that a perturbation of the plane shock wave, produced by moving a corrugated piston impulsively from rest to a constant speed in the stationary fluid, decays with time. However, this case does not have a close resemblance to actual experimental conditions in shock tube, therefore, Freeman [32] investigated the perturbations caused by non-uniformity of walls or by placing small obstacles on otherwise plane walls. He derived a mathematical expression showing that the perturbations die out in an oscillatory manner. Briscoe and Kovitz [33] performed some experiments and found that plane shock waves reflected normally from perturbed flat walls are stable. Later on, Neemeh [34] experimentally studied the stability of planar incident shocks reflected from a concave wedge-shaped end wall in a shock tube. He concluded that the reflected shock front is stable.

Whitham [23] and Butler [59] studied the behaviour of slightly distorted, but very strong converging cylindrical and spherical shock waves, and found that the amplitude of the disturbances increases as the shock converges. The analysis is approximate and is based on internally developed weak disturbances in very strong shocks. Therefore, these results cannot be employed for externally perturbed weak shock analysis. Perry and Kantrowitz [12] performed experiments to produce symmetrical converging shock waves and showed that for initially weak cylindrical shocks, the wave perturbations are damped out and the symmetry is regained as the wave collapses. Nevertheless for higher Mach number, there is little success in producing symmetrical converging shocks. Knystautas and Lee [3] showed that converging shocks are stable whereas Neemeh et al [8] investigated the stability of converging shocks by the interference of the imploding shock with a small circular aperture in the shock tube. They showed that the relative size of perturbation tends to decrease at a large radius of shocks and increases as the shock collapses. However, there is sufficient experimental evidence [3,12] to conclude that stable implosions can be achieved.

The present work also deals with the stability of converging cylindrical shocks, since this is an important factor which controls the amplification of shocks and the final state of gas. In the present investigation, the shock is perturbed by cylindrical rods of different diameters placed in the path of the converging shocks. The perturbed shock is then examined at different instants during convergence to determine a stability criteria.

1.4. Objective of the Present Work

As can be seen, extensive work has been done on the production of converging cylindrical shock waves. The symmetrical converging shock is a relatively inexpensive way of increasing gas enthalpies. Such high enthalpy gases could be used to produce diamonds from graphite [36]. Further, these can be used to compress a solid to a state which cannot be attained by plane shock compression [37] and to study the response of material under random pressure and high temperature [38]. Therefore, it is worthwhile to study the stability of converging cylindrical shocks before exploring the economical methods of producing them.

It has been observed from the acoustic analysis [39], which is true only for strong shocks with infinitesimal perturbations, and Neemeh's [35] results that converging shocks are unstable. But, the final shape of the shock, distance of collapse from the geometric center and trajectories of triple points are not concluded. Lee's [3] results based on his observations show that converging shocks are stable and the mechanism for stability depends on the sweeping of triple points. But the presence of vortices during explosion phase is not justified. Therefore, it is important not only to study the stability, but also the shape of collapsing shocks for various magnitude of disturbances before drawing any conclusions. Further, it was noticed by Perry and Kantrowitz [12] that the perturbed shock did not collapse at the geometry centre. It is, however, not known so far what happens to the shape of collapsing shock and how does it shift from geometric centre.

The present work therefore, investigates the stability of converging cylindrical shocks and their collapsing mechanism by perturbations of different magnitude. The magnitude and rate of change of perturbation, the exact shape of converging shock, and the trajectories of triple points are investigated from the wave diagrams constructed based on the ray shock theory and the Chester-Chisnell-Whitham's area-Mach number relationship. The final shape of the collapsing shock, its strength, and the distance of the collapsing region from the geometric centre are studied for weak shock as well. The theoretical results obtained from the wave diagrams are then compared with those obtained experimentally to check the validity of the ray-shock theory in the present investigation. The detailed description of the theory and its application to the present problem is presented in the next chapter.

CHAPTER 2

THEORETICAL DEVELOPMENT

In this chapter, Whithams' ray shock theory and its application to the present problem is presented. Using the ray shock theory along with the Chester-Chisnell-Whitham's Area - Mach number relationship; the methodology of constructing the wave diagrams for the converging cylindrical shocks is also given. These wave diagrams are of importance when the analysis of shock propagation is carried out. Such an analysis forms the basis for the investigation of the stability of converging shocks perturbed externally by means of cylindrical rods placed in their path.

2.1. Chester-Chisnell-Whitham's Area-Mach Relationship

The relation between the varying cross-sectional area of the duct and the averaged Mach number of the shock over that local cross-sectional area was first derived by Chester [39]. He used the theory of small perturbation in the flow behind the shock and solved the linearized equation by assuming that the cross-sectional area of the duct remains close to some mean value. Shortly afterwards, the same relationship was obtained by Chisnell [14] through one dimensional steady state analysis. The detailed discussion and comparison of his results with the Guderley's solution [2] for cylindrical and spherical imploding shock waves are given by Payne [40]. Finally, Whitham [24]

So the equations (2.1) to (2.3) can be written as.

$$\frac{\partial \rho'}{\partial t} + u_1 \frac{\partial \rho'}{\partial x} + \rho_1 \frac{\partial u'}{\partial x} + \frac{\rho_1 u_1}{A_1} \frac{\partial A'}{\partial x} = 0 \quad (2.4)$$

$$\frac{\partial u'}{\partial t} + u_1 \frac{\partial u'}{\partial x} + \frac{1}{\rho_1} \frac{\partial p'}{\partial x} = 0 \quad (2.5)$$

$$\left(\frac{\partial}{\partial t} + u_1 \frac{\partial}{\partial x} \right) s' = 0 \quad (2.6)$$

Also, the equation of state can be written as

$$p = k e^{\gamma} e^{s \cdot \frac{\gamma-1}{R}} \quad (2.7)$$

Rewriting the equation (2.7) as

$$\frac{p'}{p_1} = \gamma \frac{\rho'}{\rho_1} + \frac{s'}{c_v} \quad (2.8)$$

And substituting s' from equation (2.8) in (2.6), leads to

$$\left(\frac{\partial}{\partial t} + u_1 \frac{\partial}{\partial x} \right) \frac{p'}{p_1} - \gamma \left(\frac{\partial}{\partial t} + u_1 \frac{\partial}{\partial x} \right) \frac{\rho'}{\rho_1} = 0 \quad (2.9)$$

Combining equations (2.9) and (2.4), the following equation is obtained.

$$\left(\frac{\partial}{\partial t} + u_1 \frac{\partial}{\partial x} \right) p' + c_1^2 \rho_1 \frac{\partial u'}{\partial x} + \frac{c_1^2 \rho_1 u_1}{A_1} \frac{\partial A'}{\partial x} = 0 \quad (2.10)$$

where c is velocity of sound

Performing certain transformations, equations (2.5) and (2.10) lead to

$$\left(\frac{\partial}{\partial t} + (u \pm c) \frac{\partial}{\partial x} \right) p' \pm \rho_1 c_1 \left(\frac{\partial}{\partial t} + (u \pm c) \frac{\partial}{\partial x} \right) u' + \frac{\rho_1 u_1 c_1^2}{A_1} \frac{\partial A'}{\partial x} = 0 \quad (2.11)$$

Equations (2.9) and (2.11) can be written in the total differential form as,

$$\frac{dp'}{dt} + \rho_1 c_1 \frac{du'}{dt} = - \frac{\rho_1 u_1 c_1^2}{A_1} \frac{dA'}{dx} \quad \text{along } \frac{dx}{dt} = u_1 + c_1 \quad (2.12)$$

$$\frac{dp'}{dt} - \rho_1 c_1 \frac{du'}{dt} = - \frac{\rho_1 u_1 c_1^2}{A_1} \frac{dA'}{dx} \quad \text{along } \frac{dx}{dt} = u_1 - c_1 \quad (2.13)$$

$$\frac{dp'}{dt} - \frac{1}{c_1} \frac{dp'}{dt} = 0 \quad \text{along } \frac{dx}{dt} = u_1 \quad (2.14)$$

where

$$c_1^2 = \frac{\gamma p_1}{\rho_1}$$

Integrating equations (2.12) to (2.14), the characteristics form of equations of motion are obtained as

$$p' + \rho_1 c_1 u' = - \frac{\rho_1 u_1 c_1^2}{(u_1 + c_1) A_1} A' + f_1 \quad (2.15)$$

$$p' - \rho_1 c_1 u' = - \frac{\rho_1 u_1 c_1^2}{(u_1 - c_1) A_1} A' + f_2 \quad (2.16)$$

$$p' = \frac{\rho_1}{c_1} \frac{dp'}{dt} + f_3 \quad (2.17)$$

where f_1, f_2, f_3 are arbitrary functions depending which P, Q characteristics and particle path is used. These equations describe the flow field behind a propagating shock. According to Whitham, the positive characteristics will follow a trajectory that is close to that of the shock itself as shown in Fig. (2.1). Therefore, equation (2.15) which is valid along C^+ characteristics can be applied to the shock itself. The disturbances carried by C^+ characteristics are negligible and so on $f_1 = 0$ thus equation (2.15) reduces to

$$\frac{A'}{A} = -[p' + \rho_1 c_1 u'] \frac{(u_1 + c_1)}{\rho_1 u_1 c_1} \quad (2.18)$$

The Rankine Hugoniot equations can be rewritten as

$$p_1 = \frac{p_0}{\gamma + 1} [2\gamma M^2 - (\gamma - 1)] \quad (2.19)$$

$$\rho_1 = \rho_0 \frac{(\gamma + 1)M^2}{2 + (\gamma - 1)M^2} \quad (2.20)$$

$$u_1 = \frac{2c_0}{\gamma + 1} (M - \frac{1}{M}) \quad (2.21)$$

Differentiating equations (2.19) to (2.21), following equations are obtained,

$$p' = \frac{p_0}{(\gamma + 1)} (4\gamma M M') \quad (2.22)$$

$$\rho' = \rho_0 \frac{4(\gamma + 1)M M'}{[2 + (\gamma - 1)M^2]^2} \quad (2.23)$$

$$u' = \frac{2c_0}{\gamma + 1} (1 + \frac{1}{M^2}) M' \quad (2.24)$$

Substituting the values of p' and u' from equations (2.22) and (2.24) in equation (2.18), leads to

$$\begin{aligned} \frac{A'}{A} &= - [2c_0^2 \rho_0 M + \rho_1 c_1 c_0 (\frac{M^2 + 1}{M^2})] \frac{2M'}{\gamma + 1} \cdot \frac{u_1 + c_1}{\rho_1 u_1 c_1} \\ &= - [1 + \frac{1}{M^2} + \frac{2M}{\frac{\rho_1}{\rho_0} \cdot \frac{c_1}{c_0}}] \cdot \frac{2M'}{\gamma + 1} \cdot \frac{(1 + \frac{u_1}{c_1})}{\frac{u_1}{c_0}} \end{aligned} \quad (2.25)$$

The values of $\frac{c_1}{c_0}$, $\frac{\rho_1}{\rho_0}$, $\frac{u_1}{c_1}$, $\frac{u_1}{c_0}$ can be determined from equations (2.19) - (2.21). Thus,

$$\frac{c_1}{c_0} = \left[\frac{[2\gamma M^2 - (\gamma - 1)][2 + (\gamma - 1)M^2]}{(\gamma + 1)^2 M^2} \right]^{\frac{1}{2}}$$

$$= \frac{2\gamma M^2 - (\gamma - 1)}{(\gamma + 1) M} \mu \quad (2.26)$$

$$\frac{\rho_1}{\rho_0} = \frac{(\gamma + 1) M^2}{\mu^2 [2\gamma M^2 - (\gamma - 1)]} \quad (2.27)$$

$$\frac{u_1}{c_0} = \frac{2}{\gamma + 1} \frac{M^2 - 1}{M} \quad (2.28)$$

$$\frac{u_1}{c_1} = \frac{\frac{u_1}{c_0}}{\frac{c_1}{c_0}} = \frac{2(M - 1)}{2\gamma M^2 - (\gamma - 1)} \cdot \frac{1}{\mu} \quad (2.29)$$

where

$$\mu^2 = \left[\frac{2 + (\gamma - 1)M^2}{2\gamma M^2 - (\gamma - 1)} \right]$$

Substituting the values of $\frac{c_1}{c_0}$, $\frac{\rho_1}{\rho_0}$, $\frac{u_1}{c_0}$, $\frac{u_1}{c_1}$ into equation (2.25) gives,

$$\begin{aligned} \frac{A'}{A} &= - \frac{MM'}{M^2 - 1} \left[1 + \frac{1}{M^2} + 2\mu \right] \left[1 + \frac{2(M^2 - 1)}{2\gamma M^2 - (\gamma - 1)} \cdot \frac{1}{\mu} \right] \\ &= - \frac{MM'}{M^2 - 1} \left[1 + \frac{1}{M^2} + 2\mu \right] \left[1 + \frac{2}{\gamma + 1} \frac{2\gamma M^2 - (\gamma - 1) - 2 - M^2(\gamma - 1)}{[2\gamma M^2 - (\gamma - 1)]\mu} \right] \\ &= - \frac{MM'}{M^2 - 1} \left[1 + \frac{1}{M^2} + 2\mu \right] \left[1 + \frac{2}{\gamma + 1} \left(\frac{1}{\mu} - \mu \right) \right] \quad (2.30) \end{aligned}$$

This can be written in simplified form as

$$\frac{A'}{A} = - \frac{2MM'}{(M^2 - 1)} \cdot \frac{1}{K(M)}$$

or

$$\frac{dA}{A} + \frac{2M}{(M^2 - 1)K(M)} \cdot dM = 0 \quad (2.31)$$

where

$$K(M) = 2 \left[\left(1 + \frac{1}{M^2} + 2\mu \right) \left(1 + \frac{2}{\gamma + 1} \frac{1 - \mu^2}{\mu} \right) \right]^{-1} \quad (2.32)$$

which is called 'Chester Function' and the variation of this function is shown in Fig. (2.2). It is clear from the figure that $K(M)$ is a slowly varying function of shock Mach number. Equation (2.31) is called Chester-Chisnell-Whitham relation or simply the 'CCW' relation. This states that for a given finite area change, the change in shock Mach number depends only on M and A . For $\gamma = 1.4$, the value of $K(M)$ varies from 0.5 ($M = 1$) to 0.394 when $M \rightarrow \infty$. Therefore, the Mach number, in case of converging cylindrical and spherical shocks can be approximated by considering $K(M)$ as constant. Since,

$$\frac{dA}{A} = J \frac{dR_s}{R_s} \quad \begin{array}{l} J = 1 \text{ for cylindrical shocks} \\ J = 2 \text{ for spherical shocks} \end{array}$$

where R_s is radius of shock wave.

By integrating equation (2.31) for strong shocks ($M \gg 1$), the following proportionality relations are obtained

$$M \sim R_s^{-0.394} \quad \text{For spherical shocks}$$

$$M \sim R_s^{-0.197} \quad \text{For cylindrical shocks}$$

The results from exact self similar solution for $\gamma = 1.4$ are

$$M \sim R_s^{-0.3943} \quad \text{For spherical shocks}$$

$$M \sim R_s^{-0.1973} \quad \text{For cylindrical shocks}$$

Further comparison, for various values of γ is given by [40]. The equation (2.31) works well for converging shocks because the C^+ characteristic follows the shock very closely. Therefore, applying

the shock conditions to this characteristic involves negligible error. Hence, this relation can be applied to shock wave dynamics problems where only area variation is considered. The theory is valid for weak shocks as well since, in this case, the shock trajectory is very close to the positive characteristic. They are same as Mach number approaches to unity.

This CCW A-M relationship can therefore, be applied to a wide variety of shock wave dynamics problems where the shock Mach number variation with area change is required, as in the case of the ray shock theory presented in the following section.

2.2. Ray Shock Theory

The Ray shock theory due to Whitham [23] describes a new approach to solve the propagation of two or three dimensional shock wave problems, which could be extremely difficult to solve analytically. His method is an extension of the ideas of linear geometrical acoustics. He chose a curvilinear co-ordinate (α, β) system where α represents the instantaneous shock shape and β represents the orthogonal trajectories to the successive position of a curved shock wave, called 'rays' as shown in Fig. (2.3).

The shock front at time t is denoted by $\alpha = c_0 t$, where c_0 is the speed of sound in the uniform gas ahead of the shock. The distance between two successive shock positions α and $\alpha + d\alpha$, is $R_s dt$, where R_s is the speed of the shock and dt is the time taken by the shock from position α to $\alpha + d\alpha$.

$$\dot{R}_s dt = \dot{R}_s \frac{d\alpha}{C_0} = M d\alpha$$

where M is the Mach number of the shock.

Similarly β may be so chosen that the distance between neighbouring rays β and $\beta + d\beta$ is $A(\alpha, \beta)d\beta$ as shown in Fig. (2.4). Where $A(\alpha, \beta)$ is a function proportional to cross sectional area of the ray tube.

The relationship between A and M can be established by considering a curvilinear quadrilateral L, M, N and O with vertices (α, β) ; $(\alpha + \delta\alpha, \beta)$; $(\alpha + \delta\alpha, \beta + \delta\beta)$ and $(\alpha, \beta + \delta\beta)$ respectively:

If $\theta_1 =$ Angle between the ray and fixed direction of x axis at L

$\theta_2 =$ Angle between the successive ray and x axis at O

$\phi_1 =$ Angle between shock and vertical axis at L

$\phi_2 =$ Angle between the successive shock and vertical axis at M

Then $\delta\theta = \theta_1 - \theta_2 =$ change in the ray inclination from L to O .

$$\begin{aligned} &= \frac{MN - LO}{LM} \\ &= \frac{(A + \frac{\partial A}{\partial \alpha} \delta\alpha) \delta\beta - A \delta\beta}{M \delta\alpha} \end{aligned}$$

Thus

$$\frac{\partial \theta}{\partial \beta} = \frac{1}{M} \cdot \frac{\partial A}{\partial \alpha} \quad (2.33)$$

Similarly,

$$-\delta\phi = \frac{(M + \frac{\partial M}{\partial \beta} \delta\beta) \delta\alpha - M \delta\alpha}{A \delta\beta}$$

and so

$$\frac{\partial \phi}{\partial \alpha} = - \frac{1}{A} \frac{\partial M}{\partial \beta}$$

Since rays and shocks are orthogonal, that is $\phi = \theta$

$$\frac{\partial \theta}{\partial \alpha} = - \frac{1}{A} \frac{\partial M}{\partial \beta} \quad (2.34)$$

Differentiating equation (2.33) w.r.t. α and equation (2.34) w.r.t. β and by equating the resulting equations,

$$\frac{\partial}{\partial \alpha} \left(\frac{1}{M} \frac{\partial A}{\partial \alpha} \right) + \frac{\partial}{\partial \beta} \left(\frac{1}{A} \frac{\partial M}{\partial \beta} \right) = 0 \quad (2.35)$$

is obtained.

In order to complete the formulation of the theory, second relationship between A and M is taken from the CCW theory. Therefore the ray shock theory assumed that the propagation of each element of the shock through a ray tube is similar to the motion of a shock through a variable area duct with solid walls. Thus, it treats the rays as solid boundaries and ignores any change in mass, momentum or energy flux across them. Furthermore, the CCW relation is the result of an essentially one-dimensional theory, whereas equation (2.35) is derived on two-dimensional basis. This limitation is alleviated somewhat by the fact that the ray tubes can be made very small.

Equation (2.33) can be written as

$$\frac{\partial \theta}{\partial \beta} = \frac{A'}{M} \cdot \frac{\partial M}{\partial \alpha} \quad (2.36)$$

Multiplying equation (2.34) by ξ and equation (2.36) by η and adding the resulting equations, gives

$$\left(\frac{\partial}{\partial \alpha} + \frac{\eta}{\xi} \frac{\partial}{\partial \beta} \right) \theta + \left(- \frac{\eta}{\xi} \frac{A'}{M} \right) \left[\frac{\partial}{\partial \alpha} + \left(- \frac{\xi}{\eta} \cdot \frac{M}{AA'} \right) \frac{\partial}{\partial \beta} \right] M = 0 \quad (2.37)$$

This can be written as total differentiation if

$$-\frac{\xi}{\eta} \cdot \frac{M}{AA'} = \frac{\eta}{\xi} = \pm C$$

where

$$C = \left[-\frac{M}{AA'} \right]^{\frac{1}{2}}$$

From equations (2.34) and (2.36), it can be shown that

$$\frac{d\beta}{d\alpha} = \pm C \quad (2.38)$$

Thus equation (2.37) can be written as

$$\left(\frac{\partial}{\partial \alpha} \pm C \frac{\partial}{\partial \beta} \right) \theta \pm \frac{1}{AC} \left(\frac{\partial}{\partial \alpha} \pm C \frac{\partial}{\partial \beta} \right) M = 0$$

If

$$D^+ = \frac{\partial}{\partial \alpha} + C \frac{\partial}{\partial \beta}$$

and

$$D^- = \frac{\partial}{\partial \alpha} - C \frac{\partial}{\partial \beta}$$

then

$$D^+ \theta + \frac{1}{AC} D^+ M = 0$$

$$D^- \theta - \frac{1}{AC} D^- M = 0 \quad (2.39)$$

where D^+ and D^- are derivative operator representing differentiation along two families of curves C^+ and C^- . Integration of equations (2.39) leads to.

$$\begin{aligned} \theta + \int \frac{dM}{AC} &= \text{constant} & \text{along } \frac{d\beta}{d\alpha} &= C^+ \\ \theta - \int \frac{dM}{AC} &= \text{constant} & \text{along } \frac{d\beta}{d\alpha} &= C^- \end{aligned} \quad (2.40)$$

where C^+ is characteristic in the direction of increasing β with speed C and C^- in the direction of decreasing β with speed C .

Therefore, we have non-linear waves propagating with velocities $\pm C$ in the $\alpha - \beta$ plane in complete analogy to non linear waves in the x, t plane propagating with velocities $(u \pm c)$ as in gas dynamics and equation (2.40) corresponding to Riemann invariants [41], can be written as

$$\begin{aligned} \theta \pm \omega &= \text{constant along } C^\pm \\ \text{where} \quad \omega &= \int \frac{dM}{AC} \end{aligned} \quad (2.41)$$

When the family of characteristics are straight lines in the α, β plane, it is very convenient to work with wave diagrams. But in most of the cases, it is easier to work in the cartesian coordinates rather than α, β coordinates. Therefore, transformation of coordinates can be done from the geometry given in Fig. (2.5).

$$dx = M d\alpha \cos \theta - A d\beta \sin \theta$$

$$dy = M d\alpha \sin \theta + A d\beta \cos \theta$$

$$\text{Also,} \quad x = X(\alpha, \beta) \quad \text{and} \quad y = Y(\alpha, \beta)$$

$$\text{Therefore} \quad dx = \frac{\partial x}{\partial \alpha} \cdot d\alpha + \frac{\partial x}{\partial \beta} d\beta$$

$$dy = \frac{\partial y}{\partial \alpha} \cdot d\alpha + \frac{\partial y}{\partial \beta} d\beta$$

Comparing the coefficient of $d\alpha$ and $d\beta$.

$$\begin{aligned} \frac{\partial x}{\partial \alpha} &= M \cos \theta, \quad \frac{\partial x}{\partial \beta} = -A \sin \theta \\ \frac{\partial y}{\partial \alpha} &= M \sin \theta, \quad \frac{\partial y}{\partial \beta} = A \cos \theta \end{aligned} \quad (2.42)$$

Also

$$\begin{aligned} \frac{dy}{dx} &= \frac{\sin \theta \pm \frac{AC}{M} \cdot \cos \theta}{\cos \theta \pm \frac{AC}{M} \sin \theta} \\ &= \tan (\theta \pm m) \end{aligned} \quad (2.43)$$

where

$$\tan m = \frac{AC}{M}$$

and

$$C = \frac{d\beta}{d\alpha} = \left[-\frac{M}{AA'} \right]^{\frac{1}{2}} \quad (2.44)$$

'm' is the angle between characteristic and the ray direction. Hence,

$$\theta \pm \omega = \text{constant} \quad \text{along} \quad \frac{dy}{dx} = \tan(\theta \pm m) \quad (2.45)$$

The value of 'w' can be evaluated from the following equation, which is obtained by combining the equations (2.31), (2.41) and (2.44).

$$\omega = \int_1^M \frac{dM}{AC} = \int_1^M \left[\frac{2}{(M^2 - 1)K(M)} \right]^{\frac{1}{2}} dM \quad (2.46)$$

The values of ω are plotted in Fig. (2.6) whereas tabulated values are given in Table 2.1, which can be used conveniently during the construction of wave diagrams, as will be discussed later. However, the value of 'w' can be estimated for weak and strong shocks from the following equations,

$$\begin{aligned} M \rightarrow 1 \quad \omega &= 2^{\frac{3}{2}} [(M - 1)^{\frac{1}{2}} - (M_0 - 1)^{\frac{1}{2}}] \\ M \rightarrow \infty \quad \omega(\infty) &= n^{\frac{1}{2}} \log \left(\frac{M}{M_0} \right) \end{aligned}$$

where

$$n = \frac{2}{K(\infty)} = 5.0743$$

The characteristic angle 'm' can also be determined by using CCW relation and equation (2.43) as

$$\tan m = \left[\frac{(M^2 - 1)K(M)}{2M^2} \right]^{\frac{1}{2}} \quad (2.47)$$

The values of 'm' calculated for weak shocks do not agree with the experimental values [6]. Therefore this difference in values is a

reason for expecting Whitham's theory to be inaccurate for $M_0 < 3$. In order to overcome this discrepancy, Skews has suggested the following equation

$$\tan(m) = \frac{(M^2 - 1)[2 + (\gamma - 1)M^2]}{(\gamma + 1)M^4} \quad (2.48)$$

The variation of m with M as given by equations (2.47) and (2.48) are shown in Fig. (2.7) and numerical values are shown in Table 2.2. Skews demonstrated that considerable error results if equation (2.46) is used for Mach number less than 3. These results indicate that the ray shock theory will not accurately predict the characteristic angle ' m ' at any location on the diffracted shock. This fact is particularly important when wave diagram for weak shock wave is constructed in the present work.

The area of the ray shock tube is calculated by the following expression

$$A = K \cdot e^{\int_1^M \frac{2M}{(M^2 - 1)k(M)} \cdot dM} \quad (2.49)$$

This equation reduces to the following one, in case of strong shocks,

$$\frac{A}{A_0} = \left(\frac{M_0}{M} \right)^n \quad (2.50)$$

where

$$n = \frac{2}{K(\infty)}$$

The variation of A with M from equation (2.49) is given in Fig. (2.8) and tabulated values are given in Table 1.1. This is important to find out the Mach number at various radius of shock when it converges towards the centre. The equations developed so far are

used to find out various parameters of shock wave as they are required to construct the wave diagrams for the present work. It is important to understand the process which occurs when shock wave interact with any disturbance prior to discuss the application of the ray shock theory to present problem.

2.3. Reflection and Djffraction of Shock

When a planar shock is incident on a straight wall it reflects from a point of intersection in such a way that the flow after it regains its direction [27], as shown in Fig. 2.9(a). This type of reflection is called a 'Regular' and is only possible if the flow behind incident shock is supersonic. For a given Mach number of incident shock, there is a maximum angle of incidence ϕ_{\max} for which regular reflection may occur. In other words there is a minimum value of Mach number for a given value of turning angle below which regular reflection is impossible. In such cases, the reflection which takes place is called Mach Reflection as shown in Fig. 2.9(b&d). The range of Mach numbers and wedge angles within which regular reflection occur is given in Fig. (2.10). It is clear from Fig. (2.9) that in the case of Mach reflection the point 'O' detaches from the wedge surface and another shock, called the Mach stem, is issued from the reflection point. This point is called triple point and is some distance away from the wall. The Mach stem, which extends from the triple point to the wall, is usually taken to be straight although experiments [27,28] have shown that this is not necessarily the case, particularly in the region surrounding the triple point. Since part of the gas ahead of

the advancing shock wave system is processed by two shocks (incident and reflected), and part by only one shock (the Mach stem) a slip line forms in the flow field behind the Mach configuration. It is therefore, essential that a contact discontinuity should pass through the triple point. The angle between the surface and the linear trajectory path traced out by triple points is denoted by ' χ '. Hence, two shocks intersect at reflection points on the wedge surface in the regular reflection, while three in the Mach reflection. The two shock theory and the three shock theory are established by Neumann [42] and Bleakney [18] to study the transition from regular to Mach reflection.

The three shock theory may be used to locate the triple point if the stem is assumed to be straight and normal to the wall. This assumption is inherent in the ray shock theory, which uses the average strength of the Mach stem to determine its area and hence its triple point position. Both theories deviate from experimental results. However, the ray shock theory is more convenient to use especially for reflection in converging areas of finite angle change or with curved walls.

2.4. Application of the Ray Shock Theory to Plane Corners

The shock diffraction problems can be easily solved in the case of regular reflection, as discussed in the previous section. However, if the normal shock encounters a change in curvature such that Mach reflection occurs, then the triple point angle, in addition to other parameters, is required to analyse the problem. These parameters can be obtained by the application of the ray shock theory.

2.4.1. Concave Corners

A wedge of finite angle which causes the Mach reflection of incident shock as shown in Fig. (2.11), represents a concave corner.

Let α and $\alpha + \Delta\alpha$ be two successive positions of the shock wave of Mach number M_0 and R, S be the corresponding triple points. The ratio of ray tube area at successive positions of the shock can be given as:

$$\frac{A}{A_0} = \frac{\sin(\chi - \theta)}{\sin \chi} \quad (2.51)$$

The velocity of triple point 'C' in α, β plane can be obtained as

$$(RS)^2 = (M \Delta \alpha)^2 + (A \Delta \beta)^2 = (M_0 \Delta \alpha)^2 + (A_0 \Delta \beta)^2$$

or

$$(C)^2 = \left(\frac{\Delta \beta}{\Delta \alpha} \right)^2 = \frac{M_0^2 - M^2}{A_0^2 - A^2} \quad (2.52)$$

where M_0 and M represent the incident shock and Mach stem respectively.

From Figure (2.11)

$$\tan(\chi - \theta) = \frac{A \Delta \beta}{M \Delta \alpha} = \frac{AC}{M}$$

$$= \frac{A}{M} \left[\frac{M^2 - M_0^2}{A_0^2 - A^2} \right]^{\frac{1}{2}} \quad (2.53)$$

$$\tan(\chi) = \frac{A_0}{A} \cdot \frac{M}{M_0} \tan(\chi - \theta) \quad (2.54)$$

The corresponding jump in θ can be obtained by noting that

$$\cot(\theta) = \tan(TRS + SR\theta)$$

$$\cot(\theta) = \frac{\frac{AC}{M} + \frac{M_0}{A_0} \frac{1}{C}}{1 - \frac{A}{A_0} \cdot \frac{M_0}{M}}$$

substituting value of C from equation (2.52) and rearranging we get

$$\tan(\theta) = \frac{[(M^2 - M_0^2)(A_0^2 - A^2)]^{\frac{1}{2}}}{AM + A_0 M_0} \quad (2.55)$$

since Mach stem and incident shock remain contiguous during movement of triple point locus therefore, velocity of both sections must be identical and this yields the following equation

$$\frac{M}{M_0} = \frac{\cos(\chi - \theta)}{\cos(\chi)} \quad (2.56)$$

Now the solution of Mach number of the wall, shock-shock angle and Area can be obtained by solving the equations (2.31), (2.51), (2.55) and (2.56).

2.4.2. Convex Corners

The situation of shock diffraction around a plane convex corner is shown in Fig. (2.12), where the wall jumps from $\theta = 0$ to θ_w and remains at this value thereafter. If M_0 and M_w are the Mach number at plane wall ($\theta = 0$) and at convex wall ($\theta = \theta_w$) respectively, then by using equation (2.41) at two successive positions of shock, the following equation can be written

$$\theta_w - w(M_w) = -w(M_0)$$

Since at $\theta = 0$, $M = M_0$ and at $\theta = \theta_w$, $M = M_w$

M_w can be determined from the equation (2.41). Since θ and M are known in α, β plane, the shock position (x, y) can be determined by integrating along the shock or along a characteristic.

α remains constant along the shock and equation (2.42) gives

$$\int_{x_0}^x dx = - \int_{\beta_0}^{\beta} A \sin(\theta) d\beta$$

$$\int_{y_0}^y dy = \int_{\beta_0}^{\beta} A \cos(\theta) d\beta$$

x_0, y_0, β_0 are evaluated at the boundary along which shock propagates.

$$x_0 = \alpha M_w \cos \theta_w, \quad y_0 = \alpha M_w \sin \theta_w$$

Therefore

$$x = \alpha M_w \cos \theta_w - \int_{\beta_0}^{\beta} A \sin \theta d\beta$$

$$y = \alpha M_w \sin \theta_w + \int_{\beta_0}^{\beta} A \cos \theta d\beta$$

(2.57)

But in most of the cases the shock position is determined by integrating along the characteristics as follows,

$$x = x_w + \int_{\beta_w}^{\beta} A \cdot \frac{\cos(\theta + m)}{\sin m} d\beta$$

$$y = y_w + \int_{\beta_w}^{\beta} A \cdot \frac{\sin(\theta + m)}{\sin m} d\beta$$

(2.58)

It is convenient to use above integration because M, θ and m are constant along one family of characteristic thus integration becomes simple. x_w and y_w refer to the initial coordinates of the characteristics.

2.5. Application to Present Problem

The equations presented in the preceding section are used to determine the shape of a shock wave and various parameters necessary to

analyse the propagation of shock waves as they encounter a curved wall. Since the analysis of cylindrical imploding shocks is the matter of interest in this investigation, a brief description of their production is given. This follows with the analysis of the stability and collapsing mechanism.

The imploding shocks are produced in a shock tube by means of special device known as 'Three incremental area contraction'. This device is selected in preference to the other devices because of the following reasons [17],

- i) It provides uniform shocks in the exit passage.
- ii) It gives satisfactory shock amplification with a minimum attenuation in the pressure.
- iii) It provides smaller stabilization distance in the exit passage.
- iv) It provides highest Mach number.

The shape of a shock front in the three incremental area contraction is determined by employing the ray shock theory. The initially plane shock propagates down a three incremental area contraction and a Mach reflection occurs when it encounters the first corner ($\Delta\theta = 33.5$) as shown in Fig. (2.13). This results in the formation of triple point which moves with the shock and causes a discontinuity. This discontinuity is prevented for moving along the shock front by selecting the second corner in such a way that triple point resulting from first reflection is eliminated before second

starts. The incident shock is therefore, completely replaced by the Mach stem before entering into second contraction. This Mach stem is amplified and is perpendicular to the wall according to the ray shock theory. When this is reflected by a second deflection ($\Delta\theta = 37.5^\circ$), it causes again a Mach reflection of incident Mach stem and results in further amplification. The second discontinuity resulting from the formation of second triple points, is again eliminated before it hits the third corner. The second Mach stem behaves as a stronger incident shock for the third contraction. After travelling over the third increment ($\Delta\theta = 19$), the shock is completely replaced by the amplified Mach stem in a passage which is perpendicular to the shock tube axis, thus producing a strong cylindrical shock.

The Mach number of the final Mach stem can be determined by the ray shock theory as shown in Fig. (2.13). The initial Mach number M_1 , the wall increment ' $\Delta\theta_1$ ', are known. Therefore, the shock-shock angle ' χ_1 ' and Mach number ' M_1 ' can be calculated from the equations (2.31), (2.51), (2.56). Similarly knowing the second wall increment ' $\Delta\theta_2$ ' and Mach number ' M_1 '. The second shock-shock angle ' χ_2 ' and Mach number ' M_2 ' can be calculated from the same equations. Repeating this procedure for third increment ' $\Delta\theta_3$ ', the final stem Mach number can be determined. The last increment is smaller than the others to ensure that the discontinuities so formed on the shock front are weakest near the exit passage. The second Mach stem is now completely replaced by the cylindrical shock.

Once the cylindrical imploding shock is achieved, the stability of such shock can be determined by the perturbation of the shock wave before it converges. These perturbations are produced by placing cylindrical rods of various diameters, one at a time, in the path of the converging shock. The rate of change of perturbation with respect to rate of converging of cylindrical shocks determines the stability. This can be obtained from the wave diagram constructed for the particular case. This wave diagram not only provides the information to study the stability behaviour but also information about the exact shape of the shock during its convergence and the trajectory of the locus of triple points. Since the final state of gas depends upon the amplification of shock and its point of convergence, it is important to study the final shape of the collapsing shock as well. But, before constructing the wave diagram it is necessary to understand the phenomena of interaction of shock wave with the externally placed cylindrical rod.

When a shock wave strikes the solid boundary of a cylindrical rod, it reflects in one of the two configurations regular 'RR', or Mach reflection 'MR' as discussed in section (2.3). The step by step process of interaction of the shock with the rod and the type of reflection in the present problem is shown in Fig. (2.14) where the successive stages of shock wave interaction with cylindrical rod is illustrated schematically. In Figure 2.14(a) the cylindrical shock is approaching the rod and when it strikes with it, a regular reflection takes place due to a large wedge angle. This causes a reflected shock 'RR' as shown in Fig. 2.14(b). As the shock wave propagates along the surface

the rod, the angle of incidence of shock wave varies. Therefore, the transition from regular reflection to Mach reflection takes place as discussed in section (2.3). Fig. 2.14(c) shows the incident shock and reflected shock joined to the rod surface through a Mach stem 'MS'. A contact discontinuity 'CD' which divides two flows of different density but having the same pressure is also shown by dotted lines. Initially, the feet of the Mach stems are separated from each other as shown in Fig. 2.14(c). As the incident shock moves inward they come close together symmetrically at the rear stagnation point of the rod, as shown in Fig. 2.14(d). As these Mach stems 'MS' collide, another Mach type reflection takes place with second reflected shocks (RS_2), Mach stem (MS_2) and contact discontinuity (CD_2). The process is shown in Figs. 2.14(e) and (f).

The point, where regular reflection is converted into Mach reflection, is not exactly known since the transition takes place over a certain region [27,28]. The location of such a point on the surface of cylindrical rod is required to start the construction of wave diagram. Such a point, however, can be determined approximately by ray shock theory. If the length of Mach stem from the surface of cylindrical rod is denoted by λ and the radius of cylinder by 'r' then the undisturbed wave contained in a stream tube of area $A_0 = (r + \lambda) \sin \phi$ passes through the area $A_1 = \lambda$ as shown in Fig. (2.15).

$$\frac{A}{A_0} = \frac{\lambda}{(r + \lambda) \sin \phi} \quad (2.59)$$

since the incident shock and Mach stem are parts of the same surface α

$$\alpha = c_0 t = c_0 \frac{x}{R_s} = \frac{x}{M_0} = \frac{r + \lambda \cos \phi}{M_0} \quad (2.60)$$

According to Whitham's theory

$$M_0 = \frac{1}{\sqrt{\alpha}}$$

since Mach stem is assumed normal to the cylindrical surface,

$$\frac{1}{M} = \frac{1}{r} \frac{\partial \alpha}{\partial \phi}$$

substituting the value of $\frac{\partial \alpha}{\partial \phi}$ from equation (2.60), the following equation is obtained

$$\frac{\partial \lambda}{\partial \phi} = (r + \lambda) \tan \phi - \frac{M_0 r}{M} \frac{1}{\cos \phi} \quad (2.61)$$

For strong shocks $M \gg 1$, equations (2.50) and (2.59) yield

$$\frac{\lambda}{(r + \lambda) \sin \phi} = \left(\frac{M_0}{M} \right)^n$$

where $n = 5.074$ for $\gamma = 1.4$.

So, equation (2.61) reduces to

$$\frac{\partial \lambda}{\partial \phi} = (r + \lambda) \tan \phi - \frac{r}{\cos \phi} \cdot \left[\frac{\lambda}{(r + \lambda) \sin \phi} \right]^{\frac{1}{n}} \quad (2.62)$$

since regular reflection occurs for small values of ϕ , therefore for small λ , it can be said that $\frac{\partial \lambda}{\partial \phi} \ll 1$ and equation (2.62) reduces to

$$\lambda = r(\sin \phi)^{n+1} \quad (2.63)$$

It is obvious from above equation that length of Mach stem is negligible for small values of ϕ . The limiting value of λ can be

taken as 25% of the radius of cylindrical rod which gives the value of incidence angle ϕ about 49° . However, experimental results [26] indicate that Mach reflection starts when the angle of incidence of shock wave is between 45° to 50° . Therefore the initial value of ϕ , when Mach reflection starts at the surface of rod, is taken 48° to 50° start with the construction of wave diagrams. The values of Mach number and shock-shock angle for flow inclination are computed from the equations (2.31), (2.53), (2.55) and plotted in Figures (2.16) and (2.17).

The experimental results show that the ray shock theory predicts the shock shock angle for strong shock and does not agree well with the experimental results in case of weak shocks [42]. This disagreement makes the ray shock theory incapable of predicting the characteristic angle 'm' and locus of triple points correctly. Thus, in order to construct the wave diagram for a weak shock, critical angle of incidence [6], shock shock angle χ [29] and characteristic angle 'm' are used from the Figures (2.19) and (2.18) and (2.7) respectively. Whereas, the ray shock theory is used alone for the construction, of wave diagrams of strong cylindrical shocks as discussed in the following section.

2.6. Wave Diagrams and Their Characteristics

Wave diagram is a graphical representation of the propagation of waves in a two coordinate system. A great variety of nonsteady flow problems can be solved by means of wave diagrams which are constructed

by the method of characteristics, a mathematical term that is taken from the theory of partial differential equations. Physically, characteristics are two families of lines along which disturbances propagate. The construction of such diagram is important in the present work because it is not only a convenient way to analyse the propagation of converging shocks but also provides the information about stability, collapsing mechanism of converging shocks and Mach number at different locations as well. Therefore, the wave diagrams are constructed to have full information about the final shape of the shock, distance of its collapsing from the geometric centre and final state of the gas.

2.6.1. Construction of Wave Diagrams

The converging cylindrical shocks are perturbed by a cylindrical rod to study its stability and collapsing mechanism. Therefore, regular reflection starts initially when imploding shock interacts with the rod and Mach reflection takes place when incident shock angle reaches its critical value, as discussed in section 2.3. The trajectory of triple point is called shock-shock and its role in the wave diagram is exactly analogous to that of a shock wave in more familiar case of unsteady-one dimensional gas flow. In other words it can be said that the shock-shock represents the discontinuity not only to physical flow field but also to the characteristics. The procedure to construct the complete wave diagram involve the following interactions.

1. Crossing of C^+ and C^- characteristics.
2. The characteristics and the plane of symmetry.
3. The characteristics and the shock-shock.

The procedure to first and second kind of interactions are easy and shown in Fig. (2.20). Generally, the initial conditions of gas at 1 and 2 are known as shown in Fig. 2.20(a) and the point of their intersection is located. The Q-wave through point 1 and P-wave through point 2 are known which intersect at a new point 3. The characteristics are denoted by dotted lines but for the purpose of a step-by-step procedure, these can be approximated by a sequence of short straight sections. The procedure to locate point 3 is as follows

$$\begin{aligned} C^+ &= \theta + \omega = \text{constant} \\ C^- &= \theta - \omega = \text{Constant} \\ \text{or} \quad \theta_3 &= \frac{1}{2}(C_2^+ + C_1^-) \\ \omega_3 &= \frac{1}{2}(C_2^+ - C_1^-) \end{aligned}$$

Since θ_3 and ω_3 are known, the Mach number and characteristic angle at intersecting point '3' can be obtained from equations (2.46) and (2.47). The slope of the characteristics is taken as an average of the values at each point. For instance, the correct slope of the Q-wave through points 1 and 3 are given by $(\theta_1 + m_1)$ and $(\theta_3 + m_3)$ respectively, but the slope of the corresponding straight line may be approximated by the arithmetic mean as given below

$$(\theta + m)_{1-3} = [(\theta + m)_1 + (\theta + m)_3]/2$$

The solution of second type of interaction is also simple because θ is known in this case. Since

$$C^+ + C^- = 2\theta$$

At the plane of symmetry or point of reflection $\theta = 0$, therefore

$$C^- = -C^+$$

From Fig. 2.20(b)

$$C_2^+ = - C_2^- = - C_1$$

Therefore point 3 can easily be located by interacting Q-wave through point 4 and P wave through point 2, as discussed above.

The procedure of constructing the wave diagram becomes complicated when the shock shock forms because the characteristic invariants Ps and Q changes discontinuously across the shock-shock. Thus the characteristic slope downstream of the shock-shock is unknown since θ and w are not known there and the value of Mach number jumps across it. In order to find out quantities downstream of shock-shock an iteration technique is used which is explained below.

The sketch illustrating the interaction of the imploding shock with cylindrical rod is shown in Fig. (2.21) wherein initial conditions till point 8 are known and points 9/10, 11/12 are to be located on the shock-shock. Initially a point x_9, y_9 is selected at any radius R_9 from the geometric centre. Then the ray angle $\theta_9 = \tan^{-1} \frac{y_9}{x_9}$ and the area ratio $\frac{A_9}{A_0}$ are determined since area is proportional to radius and initial radius R_0 is known. The Mach number at point 9 is calculated from the equation (2.31). Once Mach number and ray angle at point 9 are known, the Mach number, shock-shock angle and characteristic angle at point 10 can be calculated from the following equations

$$\frac{A_{10}}{A_9} = \frac{\sin(x_{10} - \Delta\theta)}{\sin x_{10}} \quad (2.64)$$

$$\frac{M_{10}}{M_9} = \frac{\cos(x_{10} - \Delta\theta)}{\cos x_{10}} \quad (2.65)$$

$$\frac{A_{10}}{A_9} = \frac{f(M_{10})}{f(M_9)} \quad (2.66)$$

$$\Delta\theta = \theta_9 - \theta_{10} \quad (2.67)$$

Since C^+ characteristic line passes through points 3 and 10 therefore

$$\begin{aligned} \theta_{10} + w_{10} &= \theta_3 + w_3 \\ \text{or} \quad \theta_{10} - \theta_3 &= \int_3^{10} \frac{dM}{AC} \end{aligned} \quad (2.68)$$

The above five equations are solved for the five unknowns at point 10 that is M_{10} , A_{10} , $\Delta\theta$, θ_{10} x_{10} . The characteristic angle m_{10} can be calculated from equation (2.47). Since the shock-shock angle at 2 and 10 and the slope of the characteristic through 3 and 10 are known therefore, the equations of straight line can be written as follows

$$y_9 - y_2 = (x_2 - x_9) \tan(x_h)_{av} \quad (2.69)$$

$$y_9 - y_3 = (x_3 - x_9) \tan(\theta + m)_{av} \quad (2.70)$$

where $x_h)_{av}$ is the average shock shock angle at point 10 and 2 with respect to fixed horizontal axis and $(\theta + m)_{av}$ is the average of slope of the characteristic lines through points 3 and 10. Therefore, from the equations (2.69) and (2.70), the location of point 9/10 can be determined. If these calculated values of x_9 , y_9 are the same as selected initially then the values calculated downstream of shock-shock are correct otherwise point 9 is reselected. However, equations (2.64) to (2.70) can also be solved simultaneously to find out 7 unknowns.

The inner shock-shock is also located by the procedure discussed before except the initial point 11 is determined by the interaction of two C^+ characteristics. Since C^+ characteristic passes through points 5 and 11 therefore

$$(\theta + w)_{11} = (\theta + w)_5$$

Similarly C^- characteristic passes through points 4 and 11. Therefore

$$(\theta - \omega)_{11} = (\theta - \omega)_4$$

From the above equations we can find θ_{11} and ω_{11} and then from equations (2.41) and (2.44) Mach number and characteristic angle at point 11 can be calculated. Therefore, in order to locate point 11, x_{11} and y_{11} are determined from the following two equations

$$y_9 - y_{11} = \tan(\theta - m)_{av} \cdot (x_2 - x_{11})$$

$$y_3 - y_{11} = \tan(\theta + m)_{av} \cdot (x_3 - x_{11})$$

once all quantities at upstream of shock shock are obtained the quantities downstream of the shock-shock are determined from the equations (2.64) to (2.68).

The downstream of the shock-shock is the Mach stem, which is assumed to be locally straight, will have a different orientation on the characteristics. Thus the effect of the characteristic intersection with the shock-shock is to bring about a curvature of Mach stem. Since, the characteristics mesh is finite, the curved Mach stem is represented by a series of straight-line segments connected together.

It should be pointed out that the ray shock theory does not predict accurately the shock-shock angle and the characteristic angle in case of weak incident shock waves. Therefore, the values of ' χ ' and ' m ' are not calculated from the ray shock theory. The results of Shirouzu and Glass [29] and equation (2.48) are used to determine the shock-shock angle and the characteristic angle.

2.6.2. Practical Suggestions

As the first step in the preparation of a wave diagram, the given data should be expressed in non-dimensional form. The number of characteristics that are entered in a wave diagram are arbitrary. The more lines drawn, the more accurate the diagram becomes in principle. In practice, however, the inaccuracy that may occur can be minimized by drawing the characteristic lines and shock-shock trajectory at average angle between the two points.

It is very convenient to use the graphs instead of solving equations simultaneously for numerical computation of the quantities downstream the shock-shock. For such a purpose, graphs to find out ratio of stem to incident Mach number and the shock shock angle versus change in deflection are plotted from the ray shock theory and are given in Figs. (2.16) and (2.17) respectively. Milton's experimental results, considering the curvature of Mach stem are also given on the same graphs which indicate that the ray shock theory slightly deviates (2 - 3%) from the experimental results. Therefore, the Milton's results [43] could be used for strong shocks. In such cases, iteration procedure starts by assuming the value of $\Delta\theta$ and then from the Figs. (2.16) and (2.17), the Mach number downstream the shock-shock and shock-shock angle can be found. Once 'M' and ' χ ' are known, the w , m and θ downstream the shock-shock can be found out from the graphs or Tables 2.1 and 2.2. Since C^+ characteristic passes through points 3 and 10 as shown in Fig. (2.21) therefore, $(\theta + w)_{10}$ calculated must be the same as $(\theta + w)_3$ whose value is interpolated by assuming linear relation

between the neighbouring characteristics. The average calculated slope between the points 3 and 10 must be such that the C^+ characteristic passes through both points. Similarly, the trajectory of the shock-shock drawn at average angle from point 2 must pass through the calculated point 10. If not, new values of $\Delta\theta$ should be assumed.

In order to get accurate results it is a good practice to construct the wave diagram initially on enlarged scale and then can be reduced to convenient scale. But it should again be enlarged before reaching the centre. For the sake of simplicity and convenience, it is possible to carry out all the computing steps without writing down anything except the results for each point of the wave diagram. The values of the P and Q waves, shock-shock angle, slope and other required quantities may be noted for each point in the wave diagram. In general, it is better to number the points and obtain all the numerical values, including intermediate steps, in tabular form. Further, the interpretation of wave diagrams are facilitated by drawing the lines of different meanings in a distinct manner.

The accuracy of wave diagram should simultaneously be carried out by checking the procedure and accuracy of iterations. The slope of the characteristics changes slightly from step to step. Any sudden change of direction should, therefore, be suspected as a possible error unless it is associated with the crossing of a discontinuity. If a check does not reveal any error, the number of waves drawn is too small for this particular region of the wave diagram. Therefore, additional waves by interpolation may be used at mean slope.

CHAPTER 3

EXPERIMENTAL SET UP AND PROCEDURE

This chapter presents a description of the experimental set up and the procedure of recording the results. All experiments are conducted in an air-to-air shock tube with the annular end of the test section bent radially inward so as to have a cylindrical implosion chamber. A three incremental area contraction is used to achieve ninety degree bend of annular plane shock wave. The shock waves in cylindrical implosion chamber are perturbed by rubber rods placed one at a time and photographs are taken at various stages during their way of convergence to study their behaviour.

The experimental set up for producing converging cylindrical shock waves consists of the following main components

- a) The Axisymmetric Shock Tube
- b) The Test Section
- c) The spark Shadowgraph System
- d) The Time Delay System
- e) Secondary Units

The schematic diagram of experimental set up is shown in Figure (3.1) and the main units are described in the following sections.

3.1. The Axisymmetric Shock Tube

The shock tube is constructed from seamless structural steel tubing with 0.7 cm wall thickness. The inner diameter of the cylindrical tube is 15.4 cm and the total length is 4.57 meters. The shock tube consists of a driver section 76.2 cm long and a basic driven section 3.81 meter long. The driven section is further divided into two parts, one 2.74 meter long followed by other 1.07 meter test section as shown in Fig. (3.1). These sections of shock tube are assembled by standard flanges of same dimensions bolted by eight M18 bolts. These flanges are made of forged steel and are welded at the end of seamless pipe before final machining so that the deformation caused by the stresses developed during the welding process may be eliminated in the final machining process. The flanges are centered with the seamless tubes and the end of the sections are faced to the final dimensions in the same setting. The O-ring groove was cut in the raised face of the flanges connecting the driver and driven sections. The shock tube is not internally machined fully because boring machine or deep hole boring machine operations were expensive. Therefore, only 15 cm from each end of each section are honed to minimize the asymmetry. This procedure is found to give satisfactory results with a considerable reduction in the machining cost. The shock tube is supported by four adjustable height rollers, two in driver section and two in driven section. These rollers are mounted on a steel column whose height is adjustable and this unit is welded to a flat steel plate.

Compressed air is used throughout the experiments since it is the only economical gas available to produce a moderate Mach number. The pressure in the driver section is increased relative to the pressure in the driven section. Therefore, the driven section is connected to vacuum system and the driver section is connected to a compressed air storage tank. This compressed air is supplied by reciprocating compressor. These connections are made by 1 cm copper tubing through the control panel. Vacuum is provided by an Edwards' vacuum pump and is connected to driven section by a 7.5 cm steel pipe followed by 1 cm copper tubing. The vacuum pressure in the driven section is measured by an MFG testing gauge (0 - 760 mm Hg) and the pressure in the driver section is measured by other gauge range 0 - 40 bar. These pressure gauges are installed on the control panel. Leakage of air is kept to a minimum possible value by reducing the number of instrumentation access holes in the driven section. Neoprene O-ring seals are used on both the flanges connecting the driver to the driven section. This assures a good grip on both sides of the diaphragm and reduces any leakage. Gaskets and high vacuum grease are used in other connecting flanges. The pressure ratio between the driver and driven sections is maintained in such a way that the Mach number of incident plane shock is 1.79. The same shock is amplified after passing through the series of three cylindrical inclined steps in the test section. These steps, which are finite increments of conical bends, allow Mach reflection and this produces a Mach stem which is redirected in its propagation and becomes the incident shock for each of the succeeding steps. Finally the Mach stem is perpendicular to the incident plane shock and a Mach number of 3 is achieved.

3.2. The Test Section

The test section is located downstream of the shock tube and is supported by an adjustable height column with U-clamps. A schematic diagram of the test section is given in Fig. (3.2). Two aluminum pipes of outer diameter 10 cm are placed concentric with the driven section of the shock tube. The length of the aluminum pipe inside the driven section is 76 cm and that inside the test section is 107 cm. The upstream end of the aluminum pipe is chamfered to 5° in order to minimize the flow disturbances at the inlet condition. The two aluminum pipes are supported at the middle by an aluminum flange of thickness 4 cm. The construction of this flange is shown in Fig. (3.3), where part A indicates the outer part of the flange with an internal bore equal to the inner diameter of the seamless pipe. The part B consists of a ring (outer diameter 10 cm and inner diameter 7.6 cm) with four webs, 1.3 cm thick and 4 cm wide. These webs are made to fit the inside surface of part A and machined separately to provide good, sharp and precise corners. On both sides of the web, wedges of 10 degrees included angle are placed to minimize the effect of the webs on the shock front shape. These wedges are made to fit accurately the inside surface of shock tube as shown in Fig. (3.2). The two aluminum pipes and the aluminum flange are assembled as shown in Fig. (3.4). The downstream end of the aluminum pipe is fitted with a 6.5 cm diameter and 0.6 cm thick plane mirror. The significance of this mirror will be explained at a later stage. The complete assembly is placed inside the shock tube as shown in Fig. (3.2).

The 'three incremental area' is placed at the extreme end of the shock tube by means of another aluminum flange made from 2.0 cm thick plate. The pitch circle diameter and outer diameter of this flange is made exactly according to the flanges attached with the shock tube. The inner bore of this flange is made according to the diameter of mirror, fitted at the end of aluminum pipe that is 6.5 cm and a rest of thickness 1 cm with diameter 12 cm is made in the middle of the flange to accommodate the fine quality commercial glass of thickness 0.95 cm. This glass is placed in between the conical contraction and the aluminum flange and sealed by a rubber gasket of 0.5 mm thickness. The assembly of the end flange and the area contraction is shown in Fig. (3.5). The glass and plane mirror are so placed that a photograph of the cylindrical shock with a maximum view of 6.5 cm diameter is obtained. The gap between the glass window and the mirror was adjusted by placing thin paper gaskets between the steel flange of test section and end aluminum flange.

The initially plane shock strikes the upstream end of the aluminum pipe (OD 10 cm). Part of this shock travels in an annulus area and the other part travels inside the aluminum pipe. The shock travelling in the annulus area then strikes the upstream wedges and as a result of this interaction, the shock is slightly distorted. When the shock moves along the webs and wedges placed at the downstream section, it regains its planar shape in a short distance of travel. This planar shock moving inside the test section then encounters the three incremental area contraction placed at the extreme downstream end of the shock tube. The shock converts into the Mach stem until it becomes

cylindrical and perpendicular to the initial plane shock. This cylindrical shock converges as it moves in the gap between the end mirror placed in the aluminum pipe and the glass placed in the end aluminum flange. The converging cylindrical shock is then perturbed by the cylindrical rod located in its path. The cylindrical rod, made of rubber, is glued on the inside of the glass at 2.5 cm from the geometric center of the apparatus. The interaction of the converging shock with the cylindrical rod causes the perturbation on the shock front. In order to study the stability and shape of the collapsing shock, a photographic history is required. A description of the photographic apparatus used is presented in the following section.

3.3. Shadow Photography System

All optical methods are based on the fact that the speed of light depends upon the refractive index of the medium through which it passes. The value of the refractive index in turn varies with the density. In a shock wave the density increases rapidly to a peak and approaches a constant value. Therefore, the selection of an optimal method depends upon the rate of the change in density. In phenomena where the refractive index varies relatively slowly, the schlieren method is used. On the other hand if the refractive index changes very rapidly, the shadowgraph method is used. Generally, as a rough approximation the schlieren method measures the first derivative whereas shadow method measures the second derivative of the refractive index [44].

The converging cylindrical shock gets stronger as it approaches the center. This results in a very large change in the density. Therefore a shadowgraph method is selected for the present work. This method is not only simpler than the schlieren method but also brings out clearly the rapid changes in the refractive index. Also, the shock-front position may be estimated to better than 0.1 mm.

A schematic arrangement of the shadowgraph photography system is shown in Fig. (3.6). It consists of a 5 KV spark source supplied by a power amplifier. A continuous light source is used for the alignment and adjustment of the system. This 100 watts constructed arc lamp is connected to a power supply unit and is cooled by a small fan (12 volt). The spark light source supplies a light pulse of 5 to 10 microseconds for instantaneous photography. This spark is triggered by a transducer placed between two condensers of focal length 17.5 cm. These serve to focus the light on a point. The size and shape of the light source is controlled by the adjustable knife edge. The knife-edge component for light interception consists of razor blades held in position by four screws and framed on a stand with sliding adjustment. This effective source has to be at the focal point, that is 123.19 cm, of the spherical mirror. This spherical mirror is adjusted such that parallel beams of light pass through the test section. The light from the test section is reflected by another plane mirror which in turn reflects the light rays onto the photographic plate.

The amplification factor is the ratio of the size of the image on photographic plate to that of the object in the test section.

It depends upon the distances of the image and the object from the mirror and its focal length. The amplification factor can be calculated from the standard formula but a simple method to obtain this factor is adopted here. A vernier with a specified opening is located at the test section. The amplification factor is then simply the ratio of the image opening on the photography plate to the actual opening of the vernier. All sets of photographs are taken by a polaroid camera (MP-3) on the 3000 ASA polaroid film. The room was completely dark before firing the shock tube since a shutter-less camera is used to take photographs of converging cylindrical shocks. The camera is placed on a stand whose height is adjustable. It was very difficult to photograph the converging cylindrical shock right at the center of collapse since the time delay unit used in the system has accuracy of ± 5 microseconds. However, after many trials, the shock collapsing at center is photographed and with reference to this time ($t = 0$) other photographs of converging shock waves are taken by changing the delay setting. This is the method of obtaining one photograph for each firing of the shock tube.

3.4. The Time-Delay Spark System

The optical method, spark shadowgraph requires a high intensity, short duration light source because photographs in sequence are necessary to study the behaviour of converging cylindrical shock waves. Thus, some provision for high frequency multiple flashes is desirable. Alternately, if the events have a high degree of repeatability, the phenomenon can be reproduced and photographed for its

successive state relative to the preceeding one to yield a time history. This process is made possible by employing the Time-Delay spark unit.

The primary components of this system are the trigger unit, the spark lamp and time delay generator. These are coupled with each other by various secondary units. The trigger unit consists of a piezoelectric pressure transducer, a pulse amplifier and a pulse generator as shown in Fig. (3.7). The pulse generator sends a signal to the trigger of an oscilloscope which is used for timing purpose and another signal of sufficient amplitude to the delay generator. In addition, the use of a manual firing switch on the pulse generator allows testing the rest of the system without the necessity of firing the shock tube, this feature is particularly advantageous for checking the alignment of the optical system.

The delayed generator output is amplified and is used to trigger another pulse generator which generates high voltage to trigger the spark unit. The spark unit produces a light for about 5 micro-seconds for the shadowgraph optical system. The spark is controlled by the hydrogen thyration tube. A positive pulse causes a thyration to induce a spark across a high voltage gap. Further detail of this unit is discussed by Wu et al [45].

3.5. Secondary Units

Several secondary units are necessary to support the primary facilities. A vacuum pump (type DU05, ultimate pressure of 0.01 mm Hg.)

is used to produce vacuum in the driven chamber of the shock tube. This vacuum pump is connected to the control panel by 1.90 cm inner diameter copper tubing and by flexible tubing to driven section. The vacuum pressure in the driven section is measured by an MFG testing gauge range 0 - 760 mm Hg vacuum. Another gauge pressure is used to measure the pressure in driver section. Mylar plastic sheets of various thickness are used as diaphragm and a thickness of 0.5 mm sheet has been selected experimentally according to the shock Mach number required.

3.6. Experimental Procedure

The shock tube is checked carefully and all unnecessary holes are closed to avoid leakage. The connections of the driver and driven chamber to the control panel are made and then the height of shock tube is adjusted by water level. The test section is cleaned and adjusted separately and placed inside the shock tube axisymmetrically, as shown in Figs. (3.2 to 3.5). The distance of the inner aluminum tube from the inner surface of shock tube is kept equal from all sides. The end flange equipped with the area contraction and glass is bolted with the extreme downstream flange of the shock tube as shown in Figs. (3.1) and (3.5). The shadowgraph system is set with the help of continuous source of light and the camera is adjusted by producing spark manually in complete darkness.

The light beam for the shadowgraph is obtained from an electric spark source which could be triggered by the signal from a time-delay unit. The output of the pressure transducer installed in

the shock tube is used to trigger the delay unit. The instantaneous photograph at a desired instance is obtained, using such a system, by adjusting the delay time.

The Mylar sheet of 0.5 mm thickness is used to separate the driver and driven chambers. The driven chamber is evacuated by the vacuum pump to 590 mm Hg. and the driver section is filled with compressed air supplied from a storage tank. The pressure just before the rupture of the diaphragm is recorded from the pressure gauges mounted on the control panel. The Mach number of the shock produced by bursting the diaphragm can be calculated from the following equation [41]

$$M_s - \frac{1}{M_s} = \left(\frac{a_4}{a_1} \right) \left(\frac{\gamma_1 + 1}{\gamma_4 - 1} \right) \left[1 - \left\{ \frac{2\gamma_1 M_s^2 + (\gamma_1 - 1)}{\gamma_1 + 1} \cdot \left(\frac{p_1}{p_4} \right) \right\}^{\frac{\gamma_4 - 1}{2\gamma_4}} \right] \quad (3.1)$$

where $\gamma_1 = \gamma_4 = 1.4$ for air.

$$a_4 = a_1$$

Since the strength of the shock does not remain the same as it travels downstream. Therefore, the Mach number of the shock at downstream end is determined experimentally. For this purpose, three transducers can be mounted at the end of the shock tube. The first pressure transducer is used to trigger the oscilloscope (Tektronix). The other two gauges are connected to the input terminals of the oscilloscope. Knowing the distance between two transducers and the oscilloscope time scale, shock velocities can be computed. The Mach number is simply calculated by dividing the shock velocity with the velocity of sound at room temperature. The pressure across the shock wave can also be calculated by

using the same set of pressure transducers. Then by knowing the transducer constant $\frac{\Delta V}{\Delta P}$ (42.5 mv/Psi), the oscilloscope voltage scale, the pressure behind the shock can be easily computed from the oscilloscope pressure traces. A Mach number of 1.79 is obtained with the driver pressure 70 psig and a driven pressure of 590 mm Hg (vacuum). The Mach number '3' of cylindrical shock at radius 25 mm from geometric center is obtained by using transducers.

The experiments are performed by keeping the same vacuum pressure in driven section and the same thickness of mylar sheet. Initially, a sequence of shadowgraphs are obtained without generating external perturbations. The experiments are repeated by placing a cylindrical rod of diameter 5 mm and then 1.75 mm at 25 mm from geometric center. A detailed discussion on these experimentally obtained photographs is given in the following chapter.

CHAPTER 4

RESULTS AND DISCUSSION

This chapter discusses the results of the experiments and effects of external perturbations of various magnitudes on the general behaviour of converging cylindrical shock waves. The interaction of converging shocks with cylindrical rods and their influence on the stability and collapsing mechanism are discussed in detail. A methodology to solve such problems theoretically through wave diagrams is analysed and the theoretically obtained values of perturbation, the inner and outer trajectories of the shock-shock and the shape of the shocks are compared with the corresponding experimental results. A mathematical model to predict the rate of growth of perturbation at any instance is presented for various sizes of cylindrical rods. Finally, the mechanism of externally perturbed collapsing shocks is presented.

4.1. Behaviour of Converging Shocks Without External Perturbation

A sequence of spark shadowgraphs illustrating the converging cylindrical shock waves is presented in Fig. (4.1). These converging cylindrical shocks are produced by passing the plane shocks of Mach number 1.79 over the three incremental area contraction, placed at the downstream end of the shock tube with a gap width of 2.5 mm. Shadowgraph (a) is the case of no flow whereas shadowgraphs (b) to (e) show the converging process. It can be seen from the photographs that

the shock front is cylindrical at large radii, but accurate measurements show that a small asymmetry exists at small radii. This small asymmetry is probably due to a small eccentricity of inner aluminum tube and surface roughness of the inner side of the shock tube. The surface finish can be improved by internal grinding or boring processes. These processes are, however, expensive and complicated, therefore not carried out in the present work. The asymmetry of the shock front at small radii causes its break down, and a Mach type reflection takes place before the shock reaches the collapsing point. This behaviour is expected because the shock is relatively strong and the collapsing is not very sharp as is obvious from the shadowgraph (e) of Fig. (4.1). A few concentric circles are seen behind the collapsing shock, these result from the multiple reflections of relatively weak reflected waves, in the three area contraction.

The expanding shocks are formed immediately after collapse of converging shocks as indicated in shadowgraphs (f, g). These clearly show the presence of concentric waves trailing behind the expanding shock. These waves result from the interaction between the expanding shock and the weak concentric waves which are initially trailing behind the converging shock. A pair of vortices are also observed during the expanding phase of the shock. As the expanding shock propagates outward, the vortices grow bigger as seen in shadowgraph (g) of Fig. (4.1). The mechanism of formation of these vortices and the effect of the external perturbation on the converging cylindrical shock is discussed in the following section.

4.2. An Experimental Study of Converging Shock-Rod Interaction

The behaviour of converging cylindrical shocks perturbed externally is studied by placing a cylindrical rod in its path of convergence. The shock interacts with the cylindrical rod and changes its configuration. Two sets of experiments are performed, one by placing a rod of diameter 5 mm and another by a rod of 1.75 mm. The spark shadowgraph of this process of interaction of cylindrical converging shocks with the cylindrical rod are taken to study the actual phenomenon taking place. These cases are shown in Figs. (4.2) and (4.3). The schematic diagram of the shock-rod interaction is given in Fig. (2.14).

The converging cylindrical shock wave impinging on a cylindrical wall yields a regular reflection and then Mach reflection. The Mach stem, MS , and the corresponding slip streams (contact discontinuities), CDI appear before the Mach stem meets at the rear end of the rod as shown in Fig. 2.14(c). The interaction of Mach stems as they collide behind the cylinder may be considered as a reflection off a solid surface instead of the symmetry axis. Here again the reflection is at first regular and then Mach type reflection appears. This is shown in Fig. 2.14(d) and in the experimental shadowgraph Fig. 4.3(b). Two secondary reflected shocks, RS_2 , and their accompanied slipstreams, CD_2 , are formed. This process is depicted by the shadowgraphs given in Fig. (4.2) and (4.3). The first triple point, intersection of reflected shock, contact discontinuity and Mach stem is called the outer triple point which travels on the shock as cylindrical shock converges. The trajectories of these triple points can be calculated from the series of

shadowgraphs. The inner triple points are formed after the second Mach reflection, as can be seen from the shadowgraph 'b' of Fig. (4.2). The trajectories of inner triple points sweep around the shock and try to come closer to the outer trajectories of the triple points. The slip streams formed by Mach reflection trail behind the converging shock front and tend to travel toward each other until they meet. This phenomenon is clear from the shadowgraphs given in Fig. (4.2).

It is clear from the photographs that the shock front shape is affected by the change in the magnitude of perturbations. The distortion of the shock front increases with the increase in the rod diameter as clear from these figures. As a result of the disturbances introduced in the flow, the shock is seen to lag behind in the direction corresponding to the location of the cylindrical rod. Photographs show the breakdown in the shock front curvature at comparatively higher radii. The shadowgraph (h) of Fig. (4.2) gives the expanding shock during the explosion phase. The expanding shock is seen to interact with the reflected waves resulting from the Mach reflection taking place during shock convergence. This interaction forms another discontinuity extending towards the convergence center. These discontinuities intersect and form the pair of vortices. The formation of these vortices are clear from the shadowgraphs taken during the explosion phase. These shadowgraphs will be discussed in detail to investigate the stability and collapsing mechanism of the converging shocks in the subsequent sections. Since the Mach number of the cylindrical shock is an important factor to analyse the present

problem, it is determined experimentally as explained in the following section.

4.3. Flow Field Measurement

The Mach number of a shock generated in a shock tube can be determined by obtaining the pressure ratio between the driver and driven sections at which the diaphragm bursts. Since the Mach number of a shock wave may change during its propagation in the shock tube therefore, the local Mach number is determined in the present investigation. The pressure transducers are mounted in the annular and cylindrical section of the shock tube to find out the velocity of the shock and the pressure across it as explained in the following subsections.

4.3.1. Mach Number of the Shock in the Annular Part of Test Section

The Mach number of the shock wave in the annular section of shock tube is determined by placing two transducers upstream of the area contraction. The first transducer triggers the oscilloscope and the second records the voltage jump. This jump shows the arrival of the shock wave at the second transducer. The pressure trace obtained from the single transducer, placed at 30.48 cm from the end flange of the shock tube is shown in Fig. 4.4(a). The ordinate in this figure represents the voltage increment (0.5 v/cm). The pressure across the shock wave can be calculated from the transducer gain (42.5 mv/psia). Since the pressure ahead of the shock is known (590 mm Hg), the pressure ratio across the shock can be obtained. The local value of

the shock Mach number is then determined either by using the normal shock table or by employing the following basic equation of normal shock waves expressed in terms of shock Mach number and the static pressure ratio [46]

$$M_1 = \left[1 + \frac{\gamma + 1}{2\gamma} \frac{\Delta p_1}{p_i} \right]^{1/2} \quad (4.1)$$

where

Δp_1 is the pressure difference across the shock in the annular section

p_i is the absolute value of the (vacuum) pressure ahead of the shock.

It can be seen from the pressure trace that the pressure behind the shock front is steady. This shows that no expansion waves are trailing behind the shock front. The Mach number calculated in an annular section is found to be 1.79. Since the Mach number is a function of the square root of the pressure difference, the results obtained by this method are fairly accurate. Since the shock strength varies when it passes through the variable area duct, the value of the Mach number in the cylindrical chamber also changes as it propagates towards the centre. Therefore, it is necessary to find out the local value of Mach number in the cylindrical chamber when the shock wave hits the cylindrical rod.

4.3.2. Mach Number of Shock in the Cylindrical Chamber

The local shock Mach number in the cylindrical implosion chamber is determined by placing a pressure transducer at radius of

25 mm from the geometric center. This transducer is connected to an oscilloscope from which a pressure trace is obtained. A typical pressure trace for incident shock Mach number of 1.79 and cylindrical chamber gap of 2.5 mm, is given in Fig. 4.4(b). The pressure difference across the converging shock at the radius of 25 mm is thus obtained by measuring the ordinate of the pressure trace and dividing it by the gain of transducer (32.5 mv/psia). The normal shock equation (4.1) is used to calculate the Mach number. However, if the Mach number and pressure across the annular plane shock is known then the Mach number in the cylindrical chamber can be obtained by using the following equation

$$M_2 = [1 + \frac{\Delta p_2}{\Delta p_1} (M_1^2 - 1)]^{\frac{1}{2}} \quad (4.2)$$

where Δp_2 is the pressure difference across cylindrical shock M_1 , Δp_1 are the quantities determined in section 4.3.1.

The Mach number of the cylindrical converging shock can also be calculated conveniently from the following equation,

$$M_2 = [1 + (M_1^2 - 1) \frac{\Delta v_2}{\Delta v_1}]^{\frac{1}{2}} \quad (4.3)$$

where Δv_1 and Δv_2 are the voltage rise in the cylindrical and annular sections respectively, determined directly from the Fig. (4.4). The Mach number of the cylindrical shock at 25 mm from geometric center is found to be 3. Once the Mach number is determined, the cylindrical rods are placed to study the behaviour of cylindrical converging shocks under external perturbations.

4.4. Theoretical Analysis of the Converging Cylindrical Shocks Subjected to External Perturbation

The theoretical analysis of cylindrical shocks is based on the Whitham's Ray-shock theory and the well known Chester-Chisnell-Whitham's A-M relation. Wave diagrams are constructed to analyse the behaviour of initially strong cylindrical shocks and weak shock. The external perturbations are generated by placing a cylindrical rods of various diameters at 25 mm from the geometric center. The interaction of a cylindrical rod and converging shock wave, and the procedure of constructing the wave diagram is given in Chapter 2. However, before studying the stability of converging shocks, the influence of external perturbations on initially strong and weak shocks is discussed in the following sections.

4.4.1. The Behaviour of Initially Strong Shocks

The initial upper half of the wave diagram for shock Mach number of 3 at radius 25 mm, perturbed by a cylindrical rod of diameter 5 mm is given in Fig. (4.5). Interaction of the shock and the characteristic waves are marked by numbers and the corresponding values of flow parameters at each point are given in the Table (4.1). This wave diagram is completed by means of a step-by-step procedure and is given in Fig. (4.6). Under the same initial conditions, the size of externally produced perturbations were reduced by decreasing the diameter of the cylindrical rod to 1.75 mm, 0.8 mm and 0.25 mm. These rods are placed, one at a time and the wave diagrams are constructed for each case and are given in Fig. (4.7), (4.8) and (4.9), respectively.

From these diagrams, it is clear that Mach reflection starts when the incident angle of the converging shock becomes 48° and the triple point travels on the shock. The trajectories of triple points are shown in dotted lines in the wave diagrams. The path of these triple points moves away in case of bigger cylindrical rod, in other words, the region affected by the disturbances increases with the diameter of the rod. These trajectories are shown in Fig. (4.10). The outer trajectories of the triple points from the wave diagram given in Fig. (4.7) are also plotted separately on the same figure and their paths are compared with the Whitham's area rule. It is observed that the tendency of these trajectories with the decrease in magnitude of external perturbation is toward the path obtained by Whitham's area rule. Surprisingly, the smoothening of the shock front curvature was observed in all cases of strong shocks and at the outer triple points only. The distance where the outer shock-shock dies out depends upon the diameter of the cylindrical rod, this indicates that the disturbances weaken on the outer part of the cylindrical shock. The experimental values of outer triple points are obtained from the shadowgraphs given in Figs. (4.2) and (4.3) and are shown on the corresponding theoretically obtained curves in Fig. (4.10). A good agreement between the theoretically and experimentally obtained outer trajectories of triple points is clear from the figure.

When the Mach stems that ride on the surface of the rod collide with each other behind the rod, their interaction may be considered as a reflection of a solid surface instead of the axis of symmetry. Here again Mach reflection takes place at a distance of

0.6 ~ 0.7 times the diameter of rod as observed from the wave diagram (4.6) to (4.9). The trajectories of inner triple points are also shown in dotted lines on the wave diagrams. The angle of the path of triple points from the horizontal depends upon the magnitude of perturbations. The shock-shock angle increases with the decrease in size of the rod. This behaviour of the trajectories of inner triple points is shown in Fig. (4.11) for the perturbations produced by rods of various diameters. Thus, the shock amplification is larger in the case of weak disturbances since the amplification of the Mach stem is proportional to the shock-shock angle. The shock front perturbed by smaller rod diameters travels faster than those perturbed by bigger rod diameters, as demonstrated in Fig. (4.11). The increasing spread between the trajectories of inner triple points also indicates the attenuation of the disturbances.

The change in the flow deflection angle across the inner Mach stem decreases with decreasing radius of the shock for all cases shown in Figs. (4.6) to (4.9). At a certain radius it starts to increase again, the points of inflection depending upon the size of the perturbations as shown in Fig. (4.12). It is evident from this figure that in case of weak disturbances ($d = 0.25$ mm) the flow deflection angle reduces to a minimum value at higher shock radius and it stays almost constant till the shock reaches close to the centre. But with the increase of cylindrical rod diameter, the minimum flow deflection angle increases and the point of inflection occurs at comparatively large shock radius. In case of a cylindrical rod of diameter 5 mm, the value of flow deflection angle stays higher and starts increasing at

comparatively high shock radii as shown in Fig. (4.12). This shows that the shock front breaks down earlier or in other words at bigger shock radius for higher values of magnitude of perturbation.

The trajectories of inner triple points are also obtained from the shadowgraph, given in Figs. (4.2) and (4.3). The experimentally obtained values of these trajectories are close enough to the theoretically obtained trajectories as obvious from Fig. (4.11). The above mentioned behaviour is for initially strong cylindrical shocks ($M=3$); the behaviour of initially weak cylindrical shock is discussed in the following section.

4.4.2. The Behaviour of Initially Weak Shock

A cylindrical shock of Mach number 1.5 at radius 25 mm from geometric centre is taken as initially weak shock. The external perturbations are generated on the shock front by placing a small rod of diameter 0.25 mm at a distance of 25 mm from geometric centre. The behaviour of such externally perturbed shock is analysed through the wave diagram, constructed by using the same technique as described in Chapter 2. Two pairs of Mach reflections are generated during the interaction with the cylindrical rod, as explained in case of strong shocks. The outer trajectories of the triple points in this case do not die out until the shock front reaches close to the centre, as obvious from the wave diagram given in Fig (4.13). The inner trajectories of triple points widen because of weak disturbances and meet with the outer trajectories of triple points close to the geometric centre as clear from the Fig. (4.14).

The inner trajectories of triple points sweep along the disturbed part of the shock front causing bigger shock-shock angle as compared to the corresponding strong shock case. Therefore the disturbed part of the shock front travels faster than the undisturbed part. The change in flow deflection in this case is also higher as compared to the corresponding strong shock case, indicating that break down of the shock front takes place even at higher radius of cylindrical shock. This analysis indicates that weak shocks are more sensitive to external disturbances as compared to the strong shocks for the same magnitude of perturbation. Thus the final values of temperature and Mach number will be less in the case of weak cylindrical shocks as compared to the strong shocks subjected to same magnitude of perturbation. The other factors affecting on the final state of the gas are discussed in the following sections.

4.5. The Stability of Externally Perturbed Cylindrical Converging Shocks

The stability of converging shocks is one of the main factors which controls the final state of the gas. Therefore the stability of converging cylindrical shocks is analyzed theoretically and experimentally in detail. In general, a converging shock wave is said to be stable if it appears to be perfectly cylindrical in shape, thus damping out disturbances as it propagates. These disturbances are produced in the present investigation, by placing a rod of different diameters at a radius of 25 mm from geometric center. A diffraction of cylindrical converging shocks by cylindrical rods is analysed in Chapter 2 wherein

a pair of Mach stems and contact discontinuities are observed. As the cylindrical shock converges, the reflected shocks sweep along the shock front. If the tangential speed of the triple points is high as compared to the radial speed, the perturbed shock front should regain its symmetry as it converges. However, if the tangential speed is smaller than the radial speed, the converging shock will never regain its symmetry. The rate of change of disturbances on the shock front with respect to shock radius also check the stability of cylindrical shock. Therefore, the factors affecting the stability of cylindrical shocks are studied theoretically and experimentally in the present work.

A set of experiments are performed to analyse the stability criteria for strong cylindrical shocks perturbed by cylindrical rods. These photographs depicting the shapes of perturbed shocks are given in Figs. (4.2) and (4.3). It is clear from these photographs that the two triple points which appear on either side of the plane of symmetry are caused by the diffraction of the cylindrical shock with the front side of the rod and from the interaction of the two Mach shocks as explained earlier. Fig. (4.2). shows a sequence of spark shadowgraphs illustrating the interaction of the cylindrical converging shock with a rod of 5 mm diameter and a shock Mach number of 3 at a radius of 25 mm from the centre. In these photographs, it is clear that the cylindrical shock front does not regain its symmetry as it converges towards the geometric centre. The disturbed part of the shock front is delayed as compared to the rest of the shock. The undisturbed part of the shock front strengthens as it converges towards the centre, so the delayed

part is not able to catch up with the rest of the shock and is therefore, lagging further behind. As a result, a breakdown in the shock front curvature is observed in the shadowgraphs (b) to (f) in Fig. (4.2). From these shadowgraphs it is clear that externally perturbed shock wave by a rod of diameter 5 mm does not regain its symmetry as it propagates. Also, the triple points do not travel with a speed faster than the radial speed of the converging shock. Therefore, the cylindrical shock perturbed by a rod of diameter 5 mm does not appear to be stable. But, before analysing this case in detail it is worthy to perform another set of experiments to analyse this phenomenon with small magnitude of external perturbations.

Another sequence of spark shadowgraphs is presented in Fig.(4.3) for the same initial conditions as before, but with a cylindrical rod of diameter 1.75 mm. Since, the smaller cylindrical rod relative to the undisturbed shock diameter gives comparatively faster speed of travel of the inner triple points along the converging shock front. In these shadowgraphs, the inner triple points sweeps along the converging shock front at faster speed than that observed in the previous case as clear from the Fig. (4.11). However, asymmetry of the shock front is clear at a comparatively smaller radius. The formation of vortices in both series of shadowgraph is observed during the expansion phase. The expanding shock front interact with the reflected waves and leads to the formation of vortices, trailing behind the expanding shock. It is apparent from the photographs that vortex formation occurs only during the expansion phase of the shock motion. The appearance of these vortices indicates the breakdown of the shock

front during the converging phase of the cylindrical shocks. This breakdown of the shock front leads to the instability of the converging shocks.

The stability of cylindrical converging shocks is also investigated theoretically from the wave diagrams, constructed for the various cases. The wave diagram, shown in Fig. (4.6) corresponds to the case shown by the series of shadowgraphs in Fig. (4.2). The successive positions of the shock wave are shown by thick lines and the values of displacement of perturbed part of shock front from its mean position are determined to check the stability. The perturbation factor ' ξ ' is defined as,

$$\xi = \frac{\Delta R}{R_s}$$

where ΔR is the distance by which the perturbed part of shock front is displaced from its undisturbed position and R_s is the instantaneous radius of the cylindrical shock wave.

The values of the perturbation factor are determined from the wave diagrams and are plotted in Fig. (4.15). It is clear from this figure that the amplitude of the disturbance does not reduce to zero. The perturbation parameter does not increase significantly for bigger radii of shock front but this parameter shoots up for small radii of shock front. These theoretically obtained values of the perturbation factor are compared with the experimentally obtained values of the same parameter. The experimental values of the perturbation factor are determined from the shadowgraphs by using the following equation

$$\xi = \frac{\Delta R}{R_s} = \left[\frac{2(D_{\max} - D_{\min})}{(D_{\max} + D_{\min})} \right] \quad (4.4)$$

where

D_{\max} is the maximum diameter of the shock front

D_{\min} is the minimum diameter of the shock front.

The experimentally obtained values of perturbation parameter are found to be in good agreement with the theoretically obtained values. The values of the perturbation factor are determined similarly for the cylindrical shocks perturbed by cylindrical rods of diameters 1.75 mm, 0.8 mm and 0.25 mm. The successive positions of shock are drawn on the wave diagrams as shown in Figs. (4.7) to (4.9) and the values of the perturbation parameter are plotted in the Fig. (4.15). The experimental values of perturbation factor from the series of shadowgraphs given in Fig. (4.3), are also shown on the corresponding theoretical curve in Fig. (4.15). It is clear from this figure that the magnitude of the perturbation depends upon the size of cylindrical rod placed in the path of cylindrical shock, and the perturbation grows faster in the case of bigger cylindrical rod. It is observed that the rate of growth of perturbation also increases with the increase of the magnitude of perturbation. The perturbation factor shoots up close to the center in case of weak ($d = .25$ mm) disturbance, indicating that the shock remains comparatively stable for a longer time.

The values of the perturbation parameter are also plotted on the log log scale as shown in Fig. (4.16) and the following general mathematical expression is obtained

$$\xi = [F \left(\frac{d}{R_0} \right)] \left(\frac{R_s}{R_0} \right)^{-G \left(\frac{d}{R_0} \right)} \quad (4.5)$$

where

d is the diameter of the cylindrical rod

R_0 is the radius at which the cylindrical rod is placed

$$F \left(\frac{d}{R_0} \right) = 0.182 \left(\frac{d}{R_0} \right) - 24.59 \left(\frac{d}{R_0} \right)^2 + 349.19 \left(\frac{d}{R_0} \right)^3 - 118.6 \left(\frac{d}{R_0} \right)^4$$

$$G \left(\frac{d}{R_0} \right) = 0.67 + 3.22 \left(\frac{d}{R_0} \right) - 38.7 \left(\frac{d}{R_0} \right)^2 + 121.4 \left(\frac{d}{R_0} \right)^3$$

$F \left(\frac{d}{R_0} \right)$ gives the magnitude of the perturbed cylindrical shock as a function of the cylindrical rod and distance at which it is placed from the geometric center. The factor $G \left(\frac{d}{R_0} \right)$ gives the rate of growth of perturbation. This mathematical expression can be used to find the displacement of the shock front at any time perturbed by any size of the rod diameter. In case of very weak disturbances, relatively small terms can be neglected since

$$\left(\frac{d}{R_0} \right)^2 \ll \left(\frac{d}{R_0} \right) \ll 1$$

Therefore, in the limit where the rod diameter is very small as compared to its distance from geometric centre, the perturbation grows as follows,

$$\xi \propto \left(\frac{R_s}{R_0} \right)^{-0.67}$$

This result agrees fairly well with Butler's theoretical analysis for small perturbations, wherein he proved that the perturbation grows as $\left(\frac{R_s}{R_0} \right)^{-0.64}$. The theoretical and experimental results are given in

Fig. (4.16) and these results are compared with the Butler's small

perturbation analysis. The theoretical results agree well with the experimentally obtained results and with Butler's results as clear from the figure. Therefore, the degree of stability can be given by the magnitude and rate of growth of perturbations. Equation (4.5) is useful in finding the magnitude of disturbances at any instance, and the rate by which these disturbances grow for various magnitude of perturbations. These results indicate that in practical sense, all converging shocks are unstable. The theoretical conditions of infinite pressure and temperature at the convergence center will then be limited to finite values. However, these values can be increased by reducing the size of perturbation in the shock tube and by improving the shape of collapsing shock close to the center. The rate of increase in perturbation does not give the exact shape of the shock, therefore it is equally important to analyse the shape of collapsing shock and its distance from the geometric centre for various magnitude of perturbations.

4.6. The Collapsing Mechanism of Cylindrical Shock Waves

The collapsing mechanism of a converging cylindrical shock wave deals with the influence of perturbations of different magnitude on the shapes of collapsing shocks and on the shift of the center of collapse from the geometric center. In present work, this phenomenon is studied by creating disturbances of various magnitudes on strong and weak cylindrical shock fronts.

The theoretical shapes of the shock front are obtained by using the Whitham's ray shock theory. The wave diagrams for different magnitudes of external perturbations are constructed as explained before and are given in Figs. (4.6) to (4.9) for initially strong cylindrical shock waves. The shapes of the shock waves are drawn on the wave diagrams, which illustrate that the perturbed part of the shock front changes its shape gradually. Whereas the undisturbed part of the shock front is unaware about the disturbances therefore converges symmetrically. The disturbed part of the shock front contributes to the asymmetry of collapse by lagging behind the undisturbed shock front. The rate of amplification of the disturbed part will of course, be less than that of the undisturbed part of shock front. This makes the delayed part to lag even further behind. The shapes of the perturbed shock front are also drawn separately for the cases where cylindrical shocks are perturbed by cylindrical rods of diameters 5 mm and 1.75 mm as shown by the solid lines in Fig. (4.17).

The shapes of the experimentally perturbed shock front are obtained from the shadowgraphs shown in the Figs. (4.2) and (4.3). These shadowgraphs are magnified to get accurate results. The shape of the perturbed shock from each of the shadowgraphs is plotted by dotted lines in the Fig. (4.17). The corresponding theoretical shapes of the perturbed cylindrical shock wave are obtained from the wave diagram and compared with the experimentally obtained shapes. A good agreement is noted which proves the validity of the theory used in present work to analyse the behaviour of converging shocks. Because of the difficulty in experimentally obtaining the shapes of the shock very close

to the center of collapse, theoretical shapes are obtained in that region. The analysis of the converging shock close to the geometric center is therefore, based only on the theoretical results. These results close to the center are taken as true since the theory is proved to be valid over a wide range.

The wave diagrams are further enlarged near the center and the shapes of the collapsing shock are obtained for the strong and weak cylindrical shocks. These diagrams are shown in Figs. (4.18) to (4.21) for initially strong shocks with cylindrical rods 5 mm, 1.75 mm, 0.8 mm and 0.25 mm respectively. It is clear from these figures that the undisturbed portion of shock front reaches the geometric centre before the disturbed part because of higher rate of amplification. The magnitude by which disturbed part of shock front lags behind varies in each case and it increases with the increase of rod diameter. This difference will cause the collapsing of shock before it reaches the geometric center. It is worthwhile to note from these figures that the final state of collapse of the shock is not a single point but rather a region whose size depends upon the magnitude of the perturbations. It is noted from the Fig. (4.18) that the shock collapses in an oval shape whose maximum length shifted from the geometric center is 1 mm. The shape of collapsing region changes from oval to almost square by decreasing the diameter of cylindrical rod as shown in the Figs. (4.19) to (4.21). The maximum length by which the collapsing region is shifted from geometric center decreases accordingly and it is found to be 0.27 mm, 0.055 mm and 0.02 mm for rod diameters 1.75 mm, 0.8 mm and 0.25 mm respectively. It is observed from the above figures

that the initially strong cylindrical shock collapses towards the cylindrical rod whose distance from the geometric center depends upon the diameter of rod. This result agrees with the Perry and Kantrowitz's experimental results [12] but contradicts the findings of Lee and Knystantas [3].

In the case of weak cylindrical shock an entirely different behaviour is observed. The amplification of the shock strength of disturbed section is observed to be higher than the undisturbed section of the shock front. Mach reflection in this case amplifies the disturbed shock front at a higher rate because of higher values of shock-shock angle and of relatively weak amplification of weak shocks. Therefore, the disturbed part of the cylindrical shock front accelerates and reaches the geometric center before the remaining part does, thus making the shock to collapse on the opposite side of perturbations as shown in the Fig. (4.22). The shock in this case collapses in an elliptical fashion and the maximum length of its shifting from the geometric center is found to be 0.76 mm, which is much higher than the corresponding case of strong shocks. This indicates that the final values of temperature and Mach number are not infinite in any case. However, the strong cylindrical shock may result in high temperature but the weak one will not, because of the large shift of the collapsing shock from geometric center for the same magnitude of disturbances, as is obvious from the Figs. (4.21) and (4.22). The final state of collapse of the cylindrical converging shock is not a single point but a region depending upon the size of the perturbations. Since small

eccentricities are always present in any shock tube facility, it is evident that a perfectly symmetrical converging shock which collapses to a single point can never be achieved practically.

CHAPTER 5

CONCLUSIONS AND RECOMMENDATIONS

The stability of converging cylindrical shocks was studied both theoretically and experimentally. External perturbations were produced by means of cylindrical rods, placed in the path of converging shocks. Based on the various results obtained, the following conclusions are drawn.

1. Highly symmetrical converging cylindrical shocks, produced experimentally, were found to retain their symmetry down to small radii, at which an eventual breakdown in shock front curvature occurred.
2. During the shock expansion phase, vortices were observed due to the breakdown in the shock front curvature. These vortices are the result of the interaction between the contact discontinuities and the expanding shock.
3. The perturbed shock does not collapse to a single point, because the unaffected portion of the front seeks its true centre of collapse whereas the perturbed part does not, either by lagging or acceleration. Further, the distance by which the collapsing region is shifted from

the centre is found to depend upon the initial Mach number of the shock and the magnitude of external perturbation.

4. For initially strong cylindrical shocks, perturbed by a cylindrical rod, the final state of collapse is shifted towards the rod side because the perturbed part lags behind the undisturbed part of the shock front. Whereas, for an initially weak cylindrical shock, the collapsing takes place beyond the geometric centre because, the rate of amplification of the perturbed part is more than that of the unperturbed part.
5. A smoothening mechanism of the shock front was noted at the outer triple points for initially strong shocks only. Whereas, such a mechanism was not observed at the inner triple points. The angle between the incident and Mach shocks was found to increase monotonically until Mach reflection was no more possible.
6. In all cases considered, the perturbations grow as the shock progresses towards the geometric centre, indicating that the symmetry of the shock front cannot be regained before it collapses and that converging cylindrical shocks are unstable.

7. A mathematical expression was obtained to predict the magnitude and rate of growth of perturbations of initially strong cylindrical shocks. In the limit where the rod diameter is very small, this expression reduces to that of Butler's small perturbation analysis.
8. High temperature resulting from converging shocks does not necessarily imply that such shocks are stable, since collapse of the unperturbed part of the shock may cause high temperature as well.

The theoretically obtained shapes of the shock front, the trajectories of triple points and the perturbation parameter were compared with those obtained experimentally. A good agreement is observed between them, which establishes the validity of the present theory in analysing the stability of converging shock waves.

Recommendations for Future Work

The present investigation has successfully achieved the objectives within the scope of the work. However, the following recommendations are suggested for future development on the problem considered in this thesis:

1. It is observed that the collapse of initially strong cylindrical shocks and that of weak shocks occur on opposite sides of the geometric centre. This indicates

that there is a particular value of the Mach number which will cause the collapse of shock waves exactly at the geometric centre. Such shock waves, of course, will result in very high values of energy at the centre.

2. The shapes of the shocks close to the geometric centre and the shift of their collapsing regions are obtained only theoretically. In order to verify them experimentally, clear photographs of the collapsing shocks near the geometric centre should be obtained by using the following
 - i - An optical glass of small thickness in the window of the end plate
 - ii - A concave mirror with large focal length
 - iii - A time delay unit with accuracy better than $\pm 1 \mu\text{sec}$
 - iv - A shock tube with minimum roundness error and better inner surface finish.
3. The behaviour of a converging cylindrical shock can be analysed by producing disturbances around the shock front. These disturbances could be produced by placing four or eight cylindrical rods symmetrically in the path of the shock wave.

4. Computer aided analysis can be carried out to find the optimum value of Mach number and the magnitude of disturbances required in order to achieve maximum possible symmetry in the collision of the converging cylindrical shocks. The algorithm given in appendix 'A' may be used to generate wave diagrams on a computer graphics terminal, for various Mach numbers of shock waves perturbed by various magnitude of disturbances. Thus, the behaviour of cylindrical shocks may be simulated, before performing the experiments.

REFERENCES

1. Lau, J.H., Kekez, M.M., Laugheed, G.D. and Savic, P., "Spherically Converging Shock Waves in Dense Plasma Research", Proceedings of the 10th International Symposium on Shock Tube and Waves, 1979, p. 396.
2. Guderley, G., "Powerful spherical and cylindrical compression shocks in the neighbourhood of the centre of the sphere and of the cylindrical axis", Luftfahrtforschung, Vol. 19, 1942, p. 302.
3. Knystautas, R., and Lee, J.H., "Experiments on the Stability of Converging Cylindrical Detonation", Combustion and Flame Journal, Vol. 16, 1971, p. 61.
4. Neemeh, R.A. et al, "Experiments on the Stability of Converging Cylindrical Shock Waves", AIAA Journal, Vol. 19, March 1981, p. 257.
5. Butler, D.S., "The Stability of Converging Spherical and Cylindrical Shock Waves", Armament Research and Development Establishment, Report No. (B) 18/56, 1956.
6. Skews, B.W., "The Shape of a Diffracting Shock Wave", Journal of Fluid Mechanics, 29, 1967, p. 297.
7. Henderson, L.F. and Lozzi, A., "Experiments of Reflections of Plane Shock Waves at Cylindrical Surfaces", Journal of Fluid Mechanics, 68, 139, 1975, p. 363.
8. Wu, J.H.T., Yu, T.S., Neemeh, R.A., and Ostrowski, P.P., "Stability of Cylindrical Converging Shock perturbed by a Bleed Aperture", Proceedings of the 12th International Symposium on Shock Tubes and Waves, Jerusalem, 1979, p. 324.

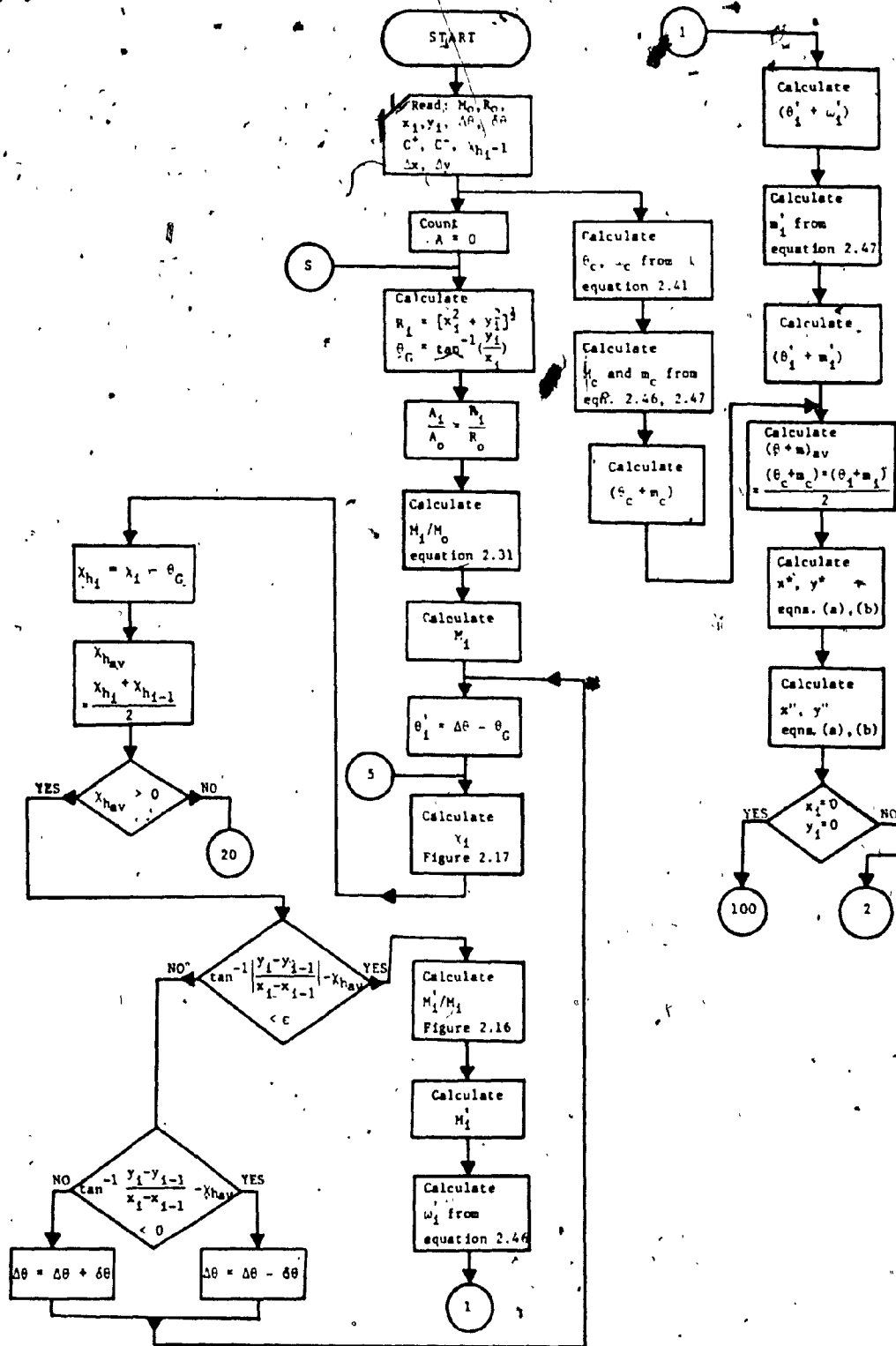
9. Stanyukovich, K.P., "Unsteady Motion of Continuous Media", Gostekhizdat, Englo. Transl., Pergamon Press, New York, 1960.
10. Payman, W., "The detonation Wave in Gaseous Mixture and the Pre-detonation Period", Proc. Royal Society, London, 120A, 1928, p. 90.
11. Perry, R.W., "The Production and Stability of Converging Shock Waves", Ph.D. Thesis, Cornell University, 1951.
12. Perry, R.W., and Kantrowitz, A., "The Production and Stability of Converging Shock Waves", Journal of Applied Physics, Vol. 22, No. 7, July 1951, p. 878.
13. Laporte, O., "On the Interaction of Shock with a Constriction". Rept. LA 1740, 1954, LOS ALAMOS Scientific Lab.
14. Chisnell, R.F., "The Motion of a Shock Wave in a Channel with Application to Cylindrical and Spherical Shock Waves", Journal of Fluid Mechanics, Vol. 2, 1957, pp. 286-289.
15. Bird, G.A., "The Effect of Wall Shape on the Degree of Reinforcement of a Shock Wave Moving into a Converging Channel", Journal of Fluid Mechanics, Vol. 5, 1959, pp. 60-66.
16. Milton, B.E. and Archer, R.D., "Generation of implosions by Area Change in a Shock Tube", AIAA Journal, Vol. 7, No. 4, 1969.
17. Neemen, R.A., "Experimental Studies of Converging Cylindrical Shock Waves Produced by Area Contractions", Ph.D. Thesis, McGill University, 1976.
18. Bleakney, W. and Taub, A.H., "Interaction of Shock Waves", Rev. Mod. Phys., Vol. 21, 1949, p. 584.
19. Bargmann, V., "On Nearly Glancing Reflection of Shocks", Applied Math. Panel Report No. 108, National Research Committee, 1945.

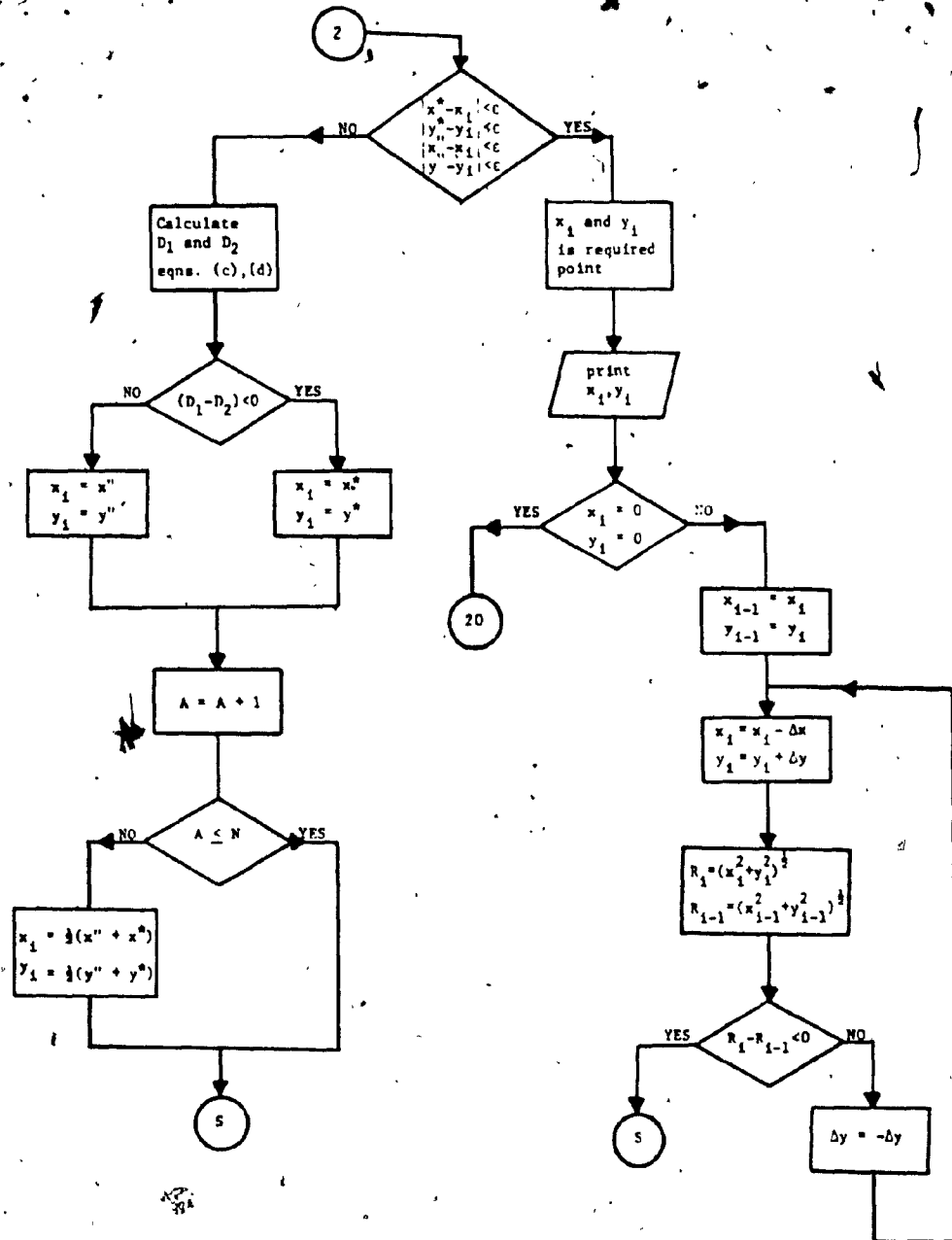
20. Lighthill, M.J., "On the Diffraction of Blast I", Proc. Royal Society, V.A192, 1449, p. 454.
21. Ludloff, H.F. and Friedman, M.B., "Difference Solution of Shock Diffraction Problems", Journal of the Aeronautical Science, 22, No. 2, 1955.
22. Smith, L.G., "Photographic Investigation of the Reflection of Plane Shock in Air", OSRD Report No. 6271, 1945.
23. Whitham, G.B., "A New Approach to Problems of Shock Wave Dynamics, Part I, Two Dimensional Problems", Journal of Fluid Mechanics, 2, 1957, p. 145.
24. Whitham, G.B., "On the Propagation of Shock Waves Through Regions of Non-Uniform Area or Flow", Journal of Fluid Mechanics, 4, 1958, p. 337.
25. Whitham, G.B., "A New Approach to Problems of Shock Wave Dynamics, Part II, Three Dimensional Problems", Journal of Fluid Mechanics, 5, 1959, p. 369.
26. Bryson, A.E. and Gross, R.W.F., "Diffraction of Strong Shocks by Cones, Cylinders and Spheres", Journal of Fluid Mechanics, 10, 1961, p. 1.
27. Heiling, W.H., "A Result Concerning the Transition from Regular Reflection to Mach Reflection of Strong Shock Waves", Proceeding of the 11th International Symposium on Shock Tube Waves, London, 1977, p. 288.
28. Itoh, S. and Itaya, M., "On the Transition between Regular and Mach Reflection", Proceedings of the 10th International Symposium on Shock Tube, Jerusalem, 1979, p. 314.

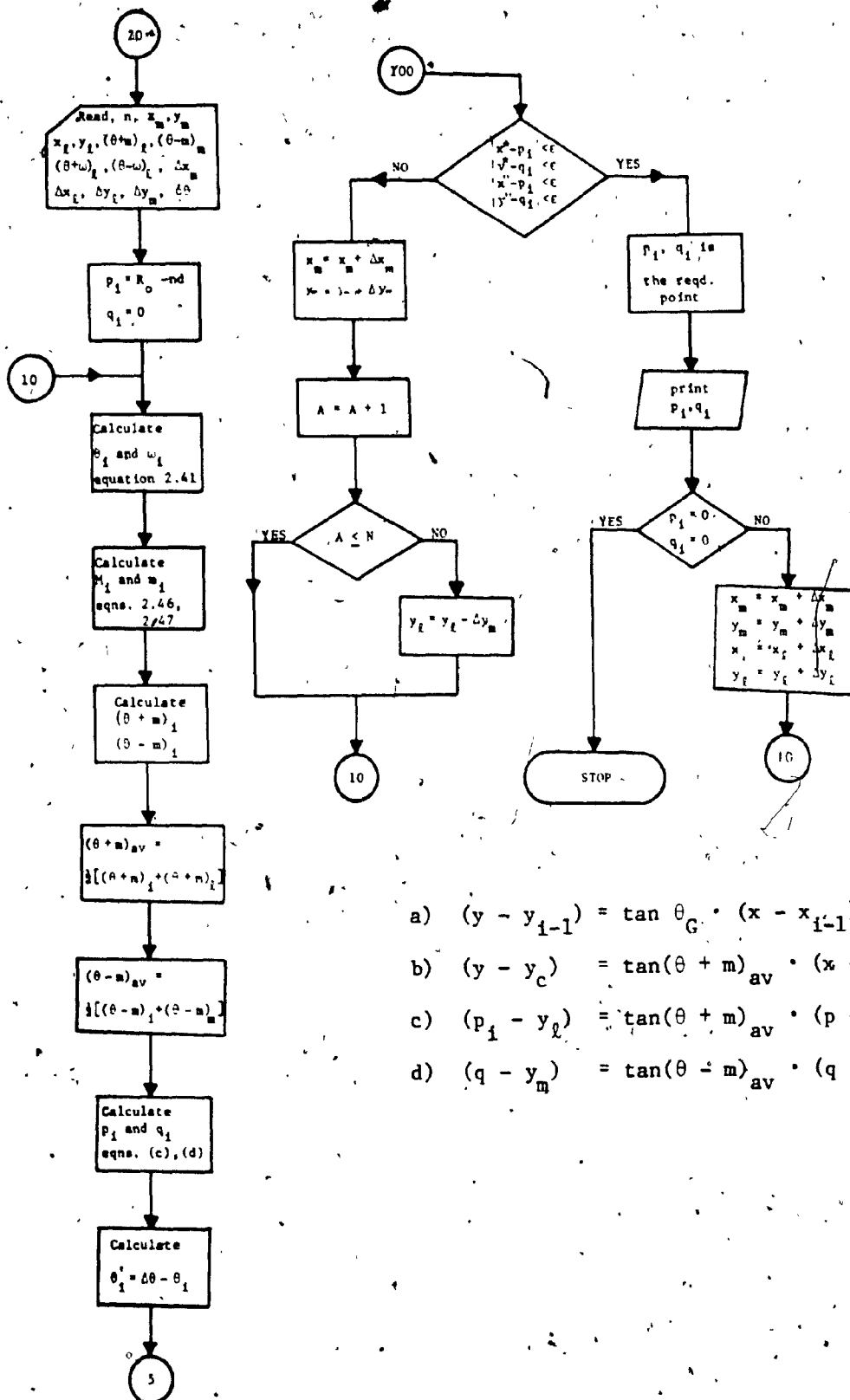
29. Glass, I.I. and Shirouzu, M., "An Assessment of Recent Results on Pseudo-Stationary Oblique Shock Wave Reflections", UTIAS Report No. 264, 1982.
30. Nagrath, I.J. and Gopal, M., "System Modelling and Analysis", Tata McGraw-Hill Publishing Ltd., New Delhi, 1982.
31. Freeman, N.C., "A Theory of the Stability of Plane Shock Waves", Proc. Royal Society, London, 2281, 1954, p. 341.
32. Freeman, N.C., "On the Stability of Plane Shock Waves", Journal Fluid Mechanics, 2, 1957, p. 397.
33. Briscoe, M.G. and Kovitz, A.A., "Experimental and Theoretical Study of the Stability of Plane Shock Waves Reflected Normally from Perturbed Flat Walls", Journal of Fluid Mechanics, Vol. 31, 1968, p. 529.
34. Neemeh, R.A. et al., "Stability of Normal Shock Reflected from a Concave Wedge - Shaped Wall", Canadian Aeronautic Space Journal, May, 1981, p. 376.
35. Neemeh, R.A. et al., "Experiments on the Stability of Converging Cylindrical Shock Waves", AIAA Journal, Vol. 19, March, 1981, p. 257.
36. Glass, I.I. and Sharma, S.P., "Production of Diamonds From Graphite using Explosive-Driven Implosion," AIAA Journal, Vol. 14, No. 3, 1976, p. 402.
37. Glass, C.M. et al., "Response of Metals to High Velocity Deformation," International Publication, New York, 1960, p. 115.

38. Murakami, T. and Nagayama, K., "Numerical Experiments of Converging Shock Waves in Solids", Proceedings of the 10th International Symposium on Shock Tube and Waves, Japan, 1979.
39. Chester, W., "The Propagation of Shock Wave in a Channel of Non-Uniform Width", J. Mech. and Appl. Math., Vol. , Part 4, 1953, p. 440.
40. Payne, R.B., "A Numerical Method for a Converging Cylindrical Shock", Journal of Fluid Mechanics, Vol. 2, 1957, p. 185.
41. Rudinger, G., "Wave Diagrams for Non Steady Flow in Ducts," D: van Nostrand Company, Inc., Toronto, 1955.
42. Von Neumann, J., "Oblique Reflection of Shocks", Report No. 12, Department of the Navy, Bureau of Ordnance, 1943.
43. Milton, B.E., "Shock Wave Motion and Focusing in Area Construction", Ph.D., Thesis, University of New South Wales, Australia, 1971.
44. Ladenburg, R.W., "Physical Measurements in Gas Dynamics and Combustion", Princeton University Press, New Jersey, 1954.
45. Wu, J.H.T., Ostrowski, P.P. and Lee, P., "Construction of Time Delayed Spark System", Tech. Note No. -71, Dept. of Mechanical Engineering, McGill University, Montreal, 1971.

APPENDIX 'A'







- a) $(y - y_{i-1}) = \tan \theta_G \cdot (x - x_{i-1})$
- b) $(y - y_c) = \tan(\theta + m)_{av} \cdot (x - x_c)$
- c) $(p_1 - y_l) = \tan(\theta + m)_{av} \cdot (p - x_l)$
- d) $(q - y_m) = \tan(\theta - m)_{av} \cdot (q - y_l)$

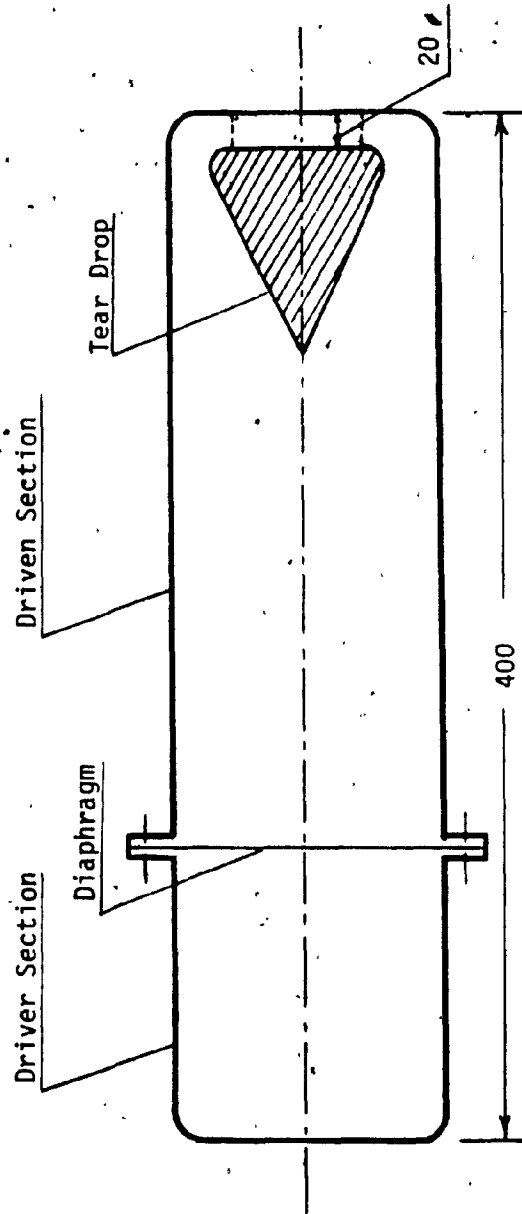
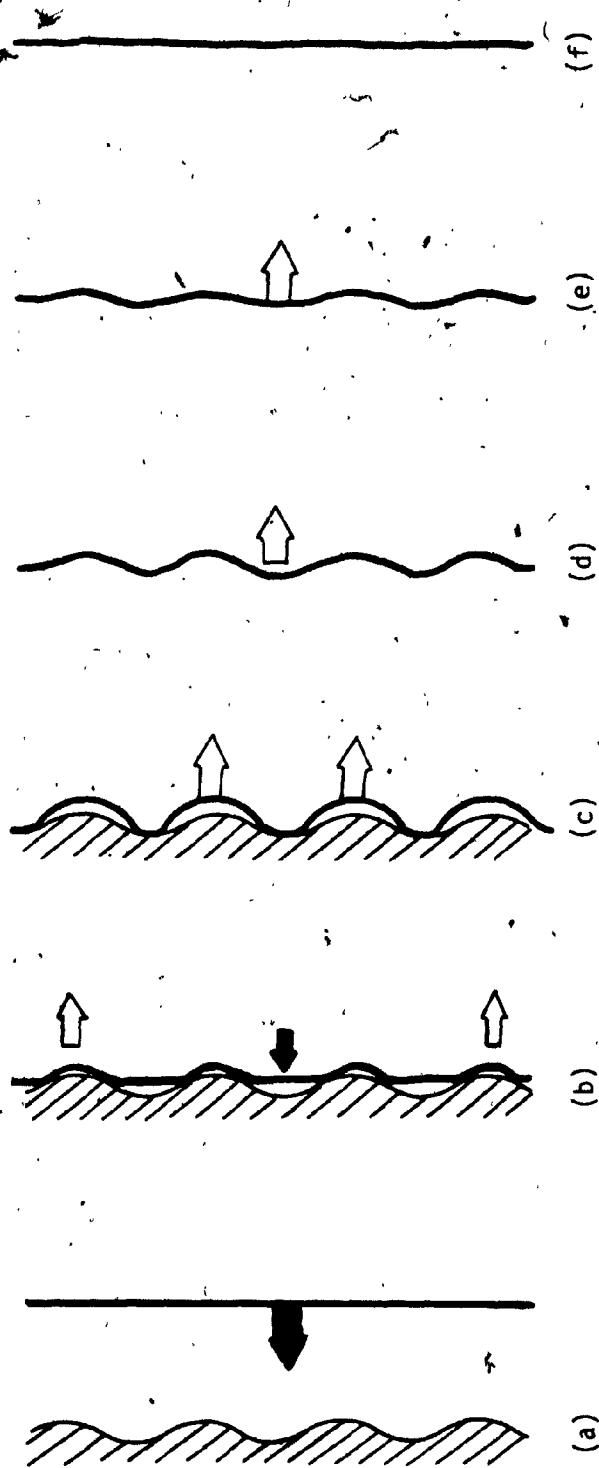


Fig. 1.1. Perry and Kontrowitz Cylindrical Shock Tube



- a) incident shock prior to reflection
- b) early period of reflection, containing both incident and reflected shock fronts
- c), d) perturbed reflected shock
- e), f) almost flat reflected shock

Fig. 1.2. Schematic Representation of Stability of Reflected Shock from a Wavy Wall

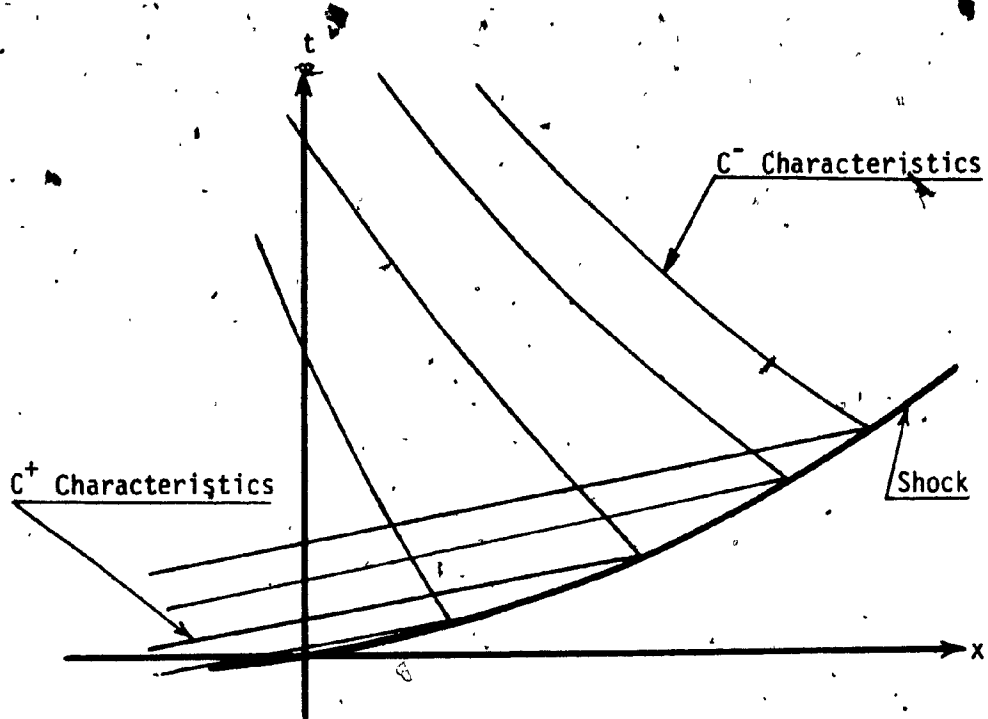


Fig. 2.1. Shock Propagation in $x - t$ plane

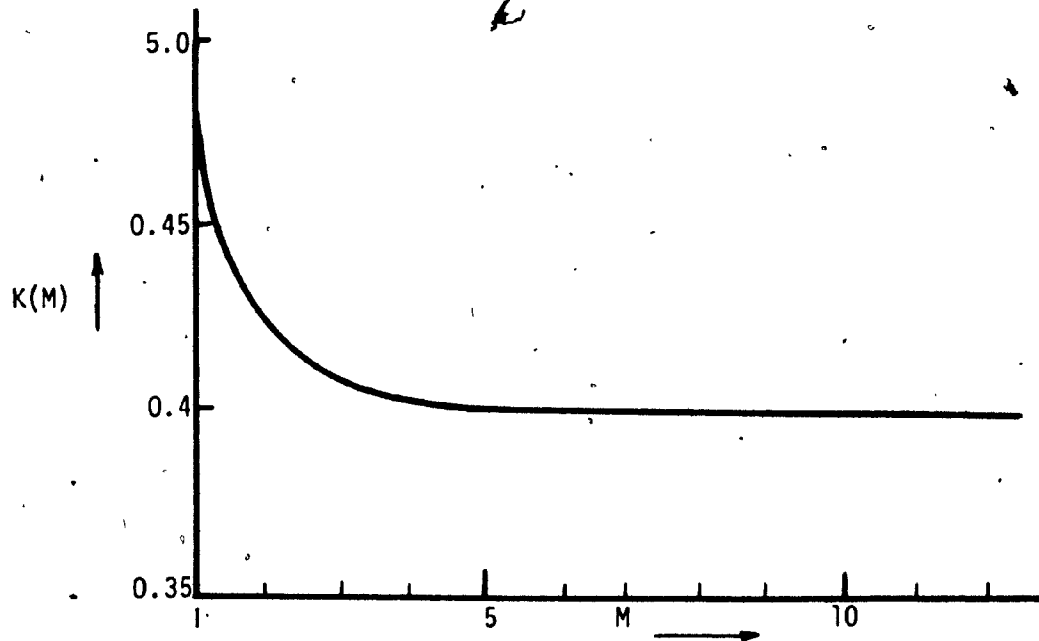


Fig. 2.2. The Graph of Chester's Function

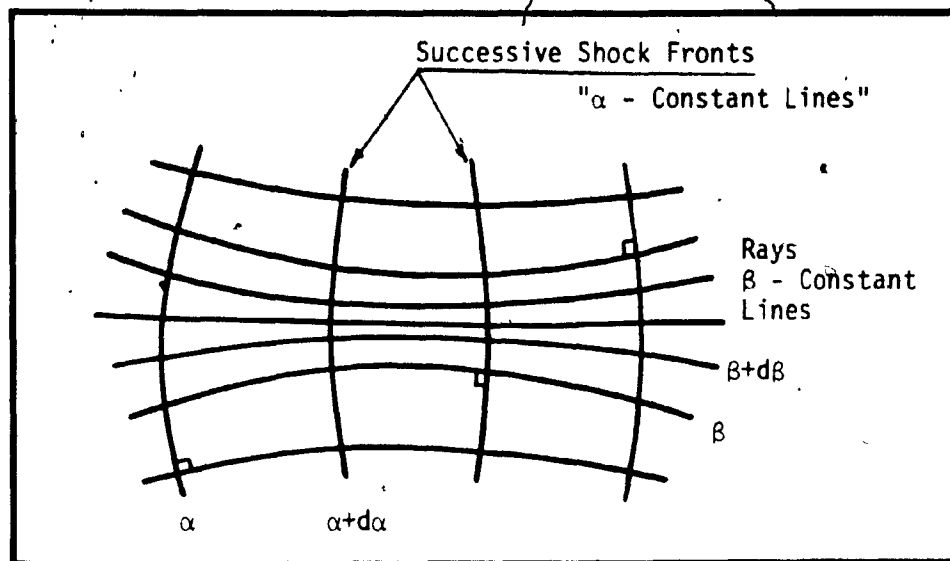


Fig. 2.3. Orthogonal Ray-Shock Coordinates

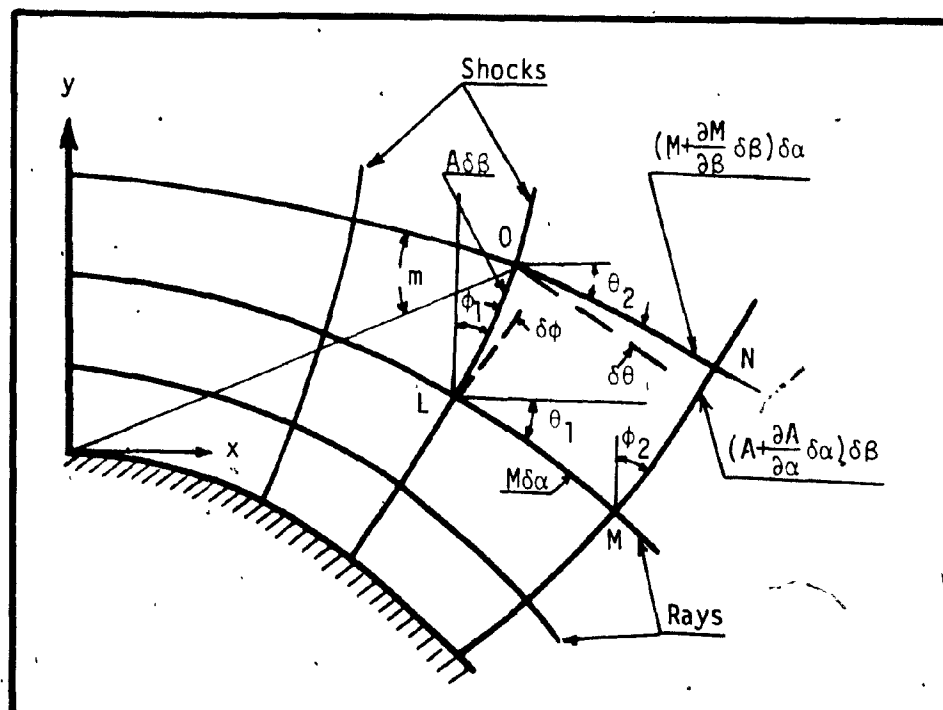


Fig. 2.4. Geometry of Ray Shock Coordinates

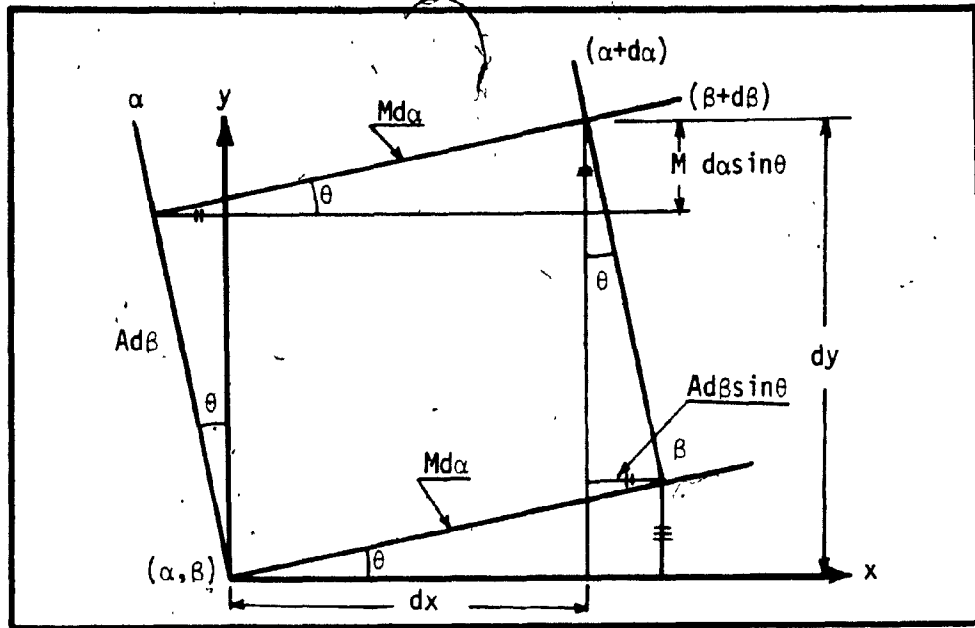


Fig. 2.5. Transformation Between Curvilinear and Cartesian Coordinates

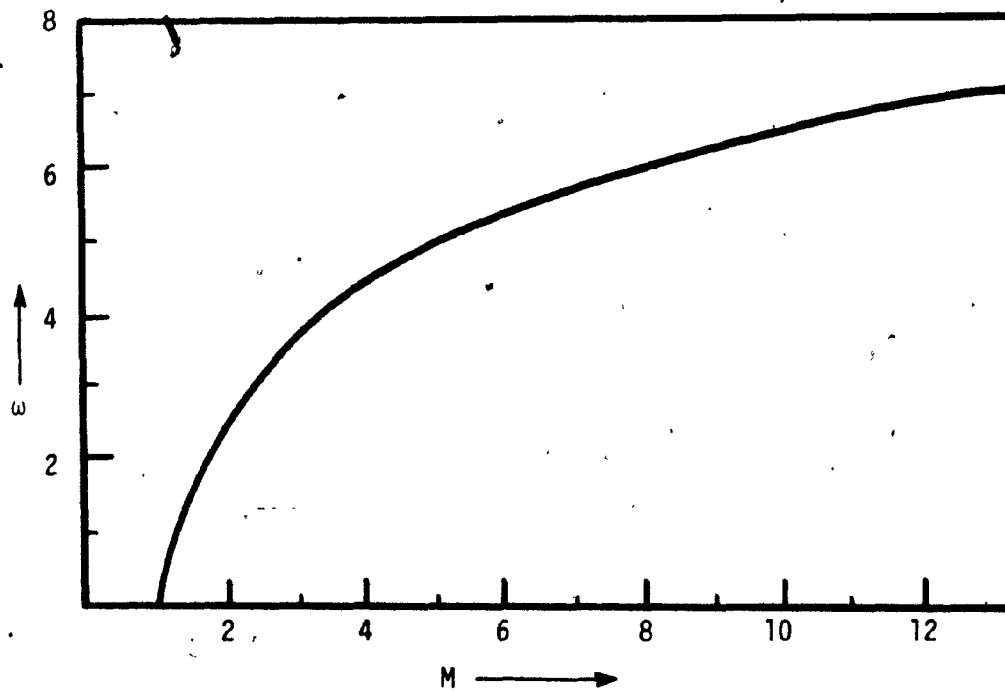


Fig. 2.6. Variation of ' ω ' verses Mach number

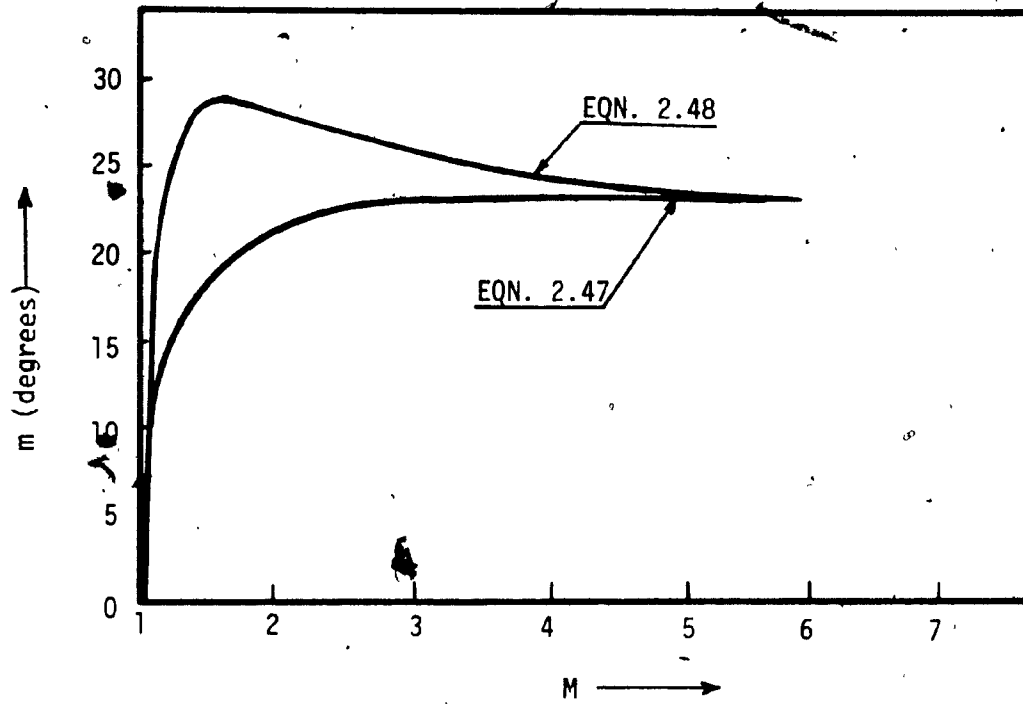


Fig. 2.7. Characteristic Angle versus Mach Number

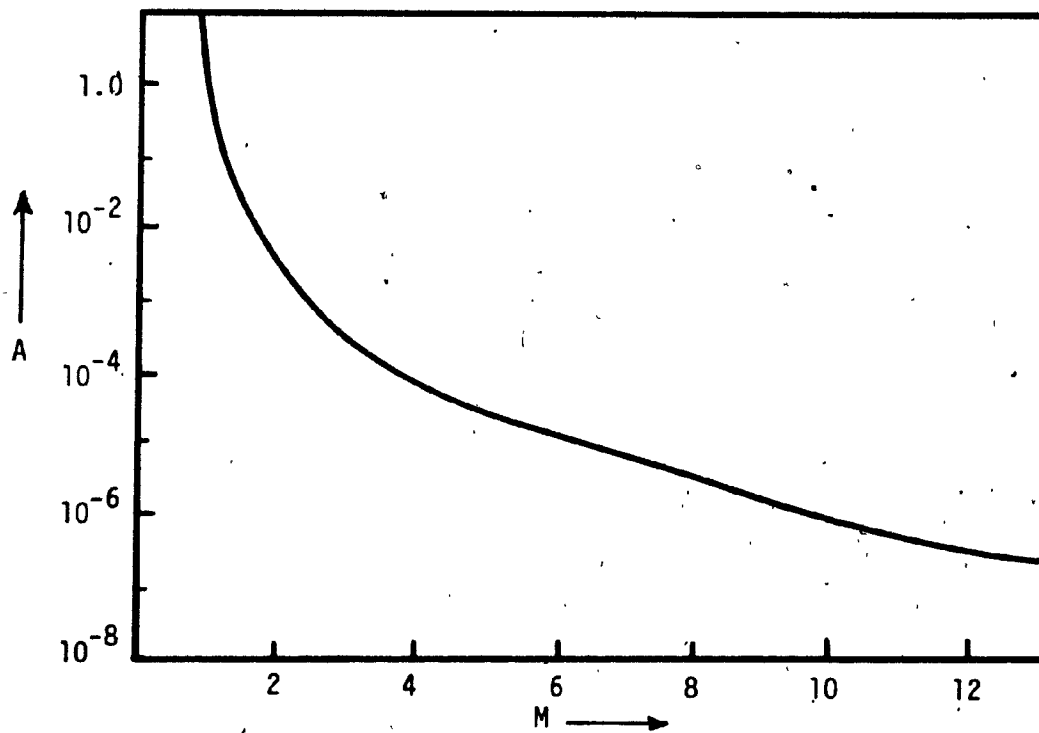
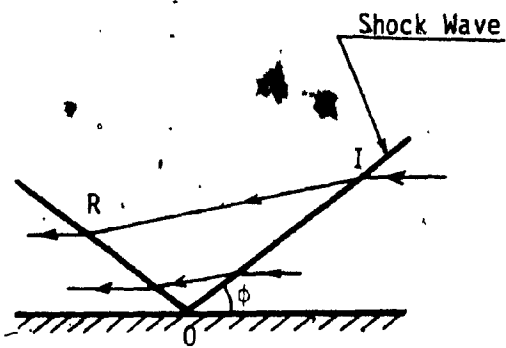
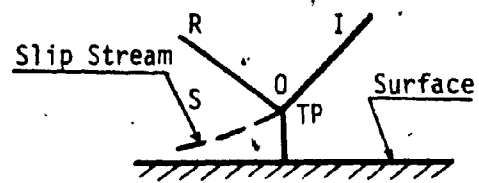


Fig. 2.8. Mach Number versus Ray Tube Area



a) Regular Reflection



b) Mach Reflection

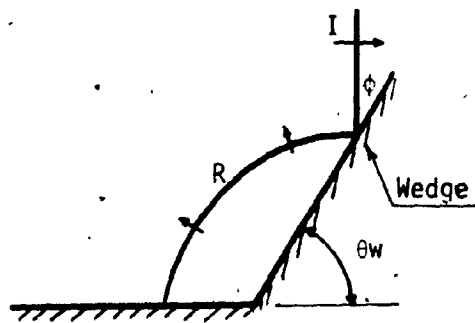
Stationary Shock

I = Incident Shock

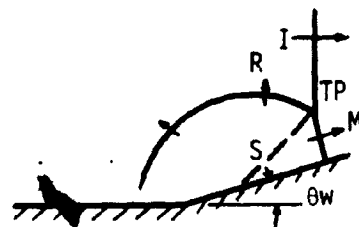
R = Reflected Shock

TP = Triple Point

M = Mach Stem



c) Regular Reflection



d) Mach Reflection

Non Stationary Shock

Fig. 2.9. Types of Reflection for Shock Wave

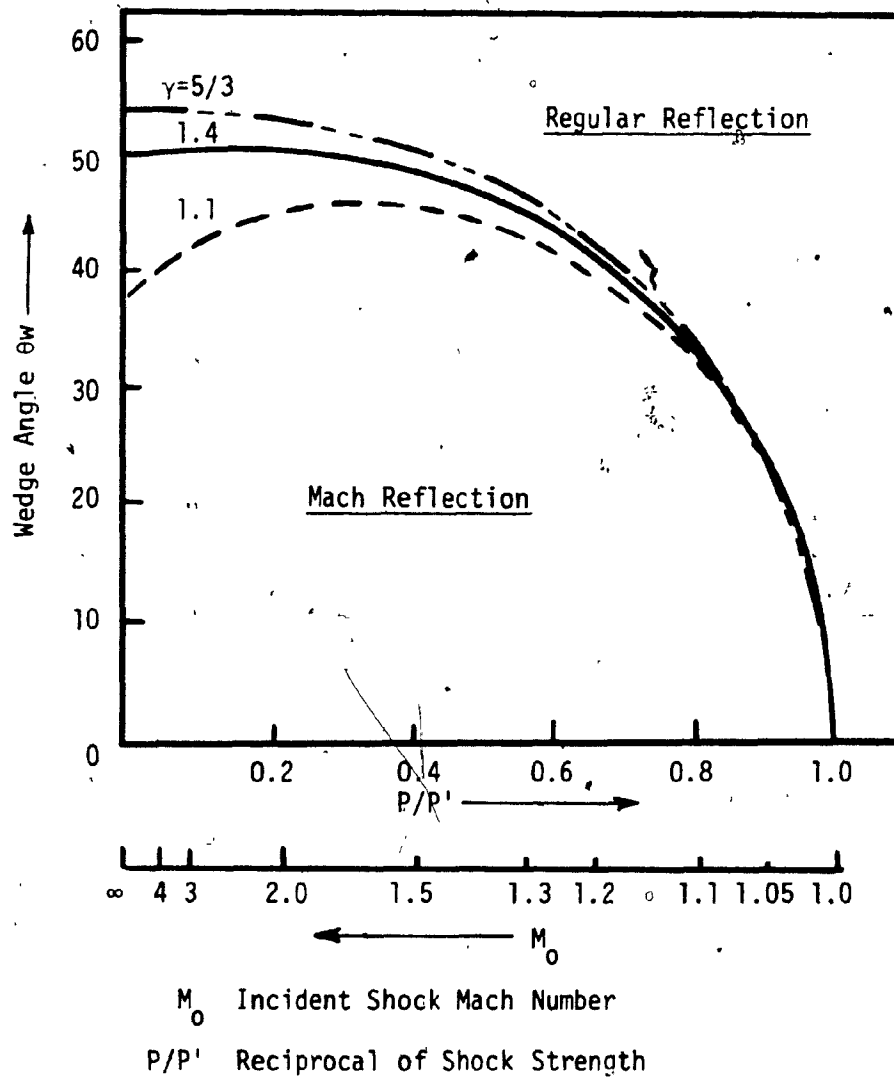


Fig. 2.10. Type of Reflection Possible for a Given Wedge Angle and Incident Shock Strength

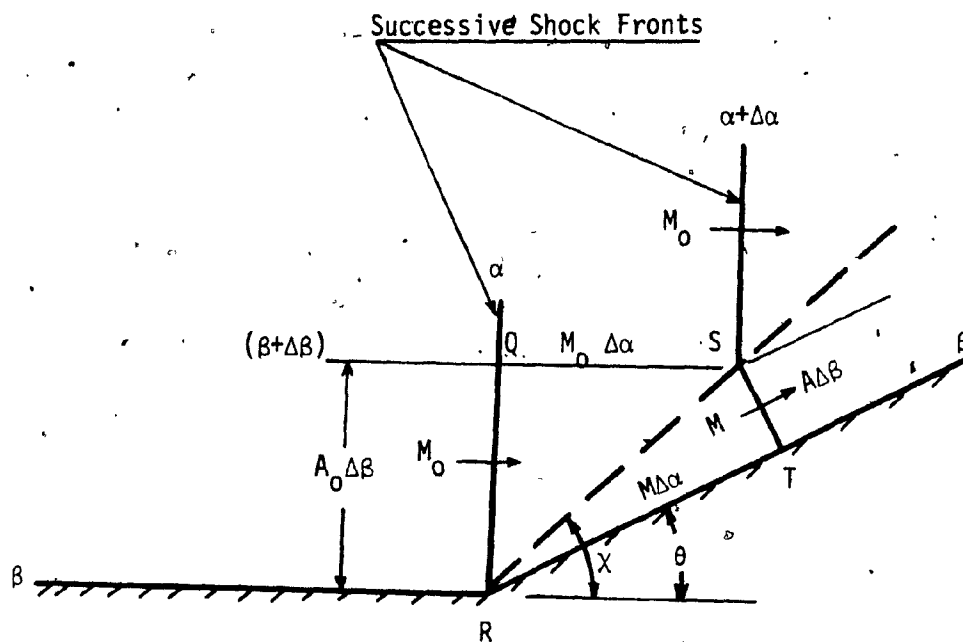


Fig. 2.11. Mach Reflection at a Concave Corner

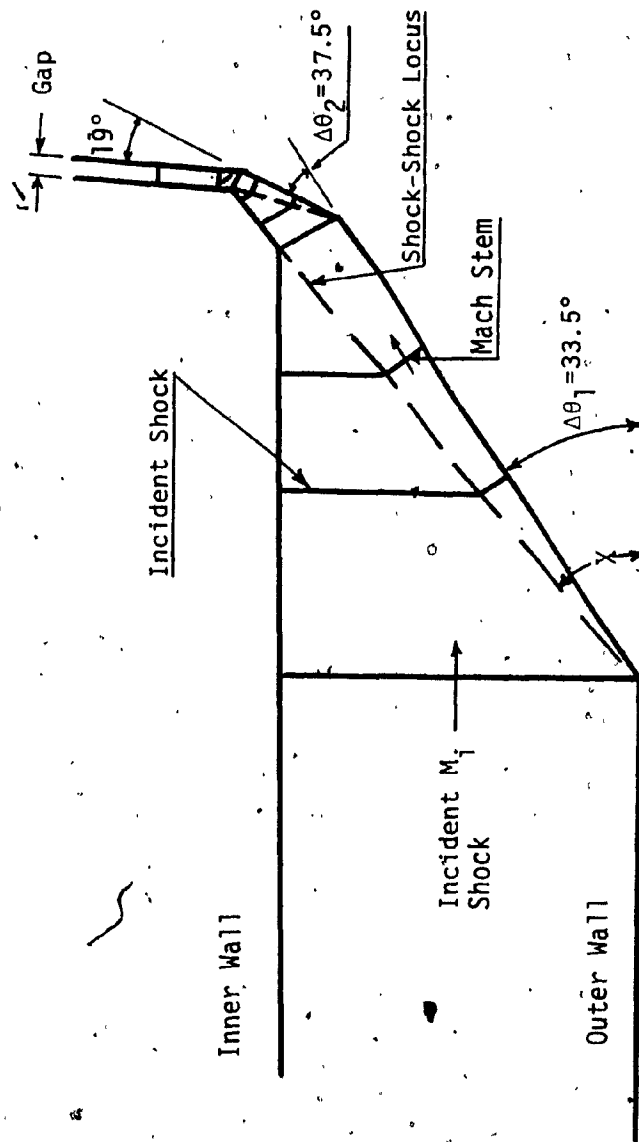


Fig. 2.13. Schematic Diagram of a Three Incremental Area Contraction

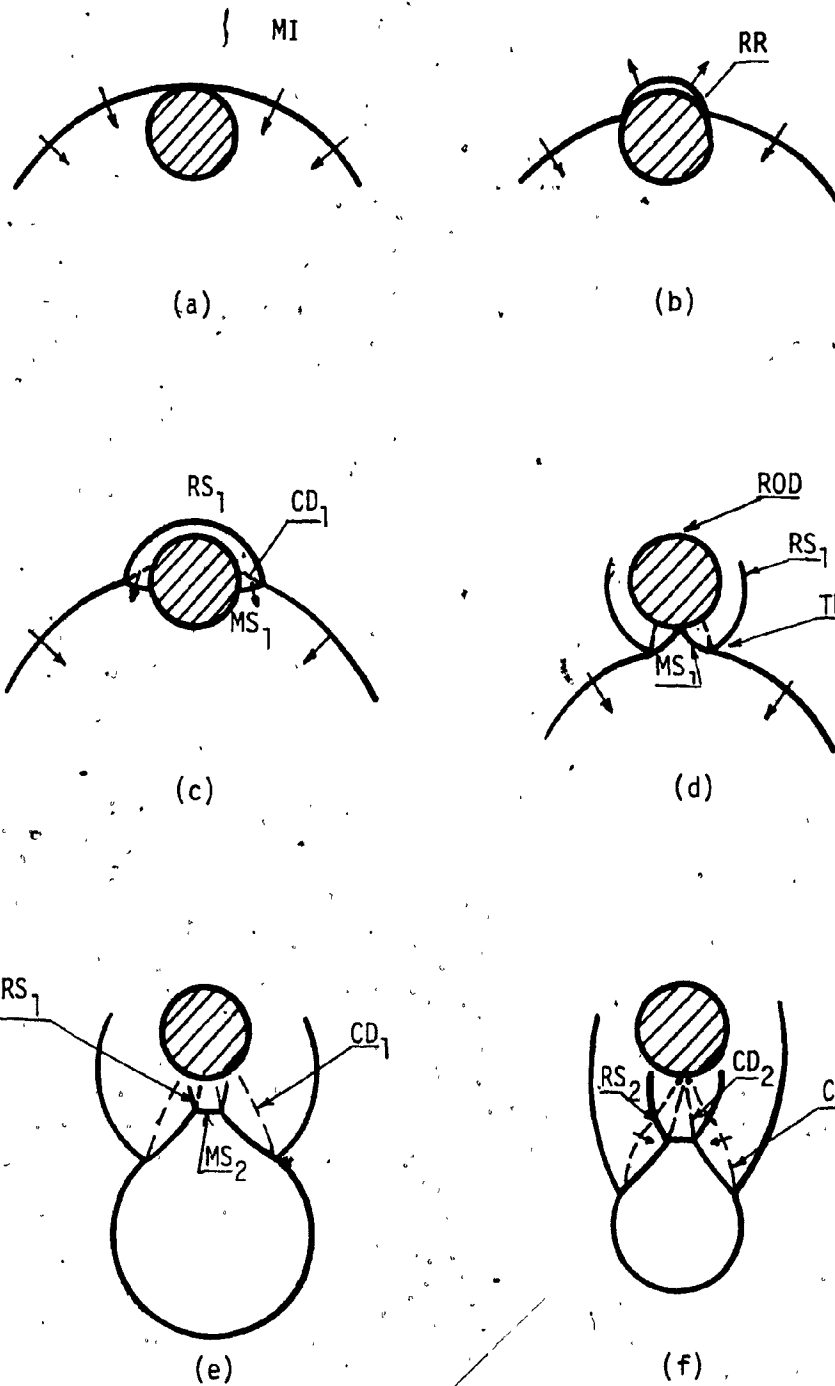


Fig. 2.14. Schematic Illustration for the Interaction of a Converging Shock with a Cylindrical Rod

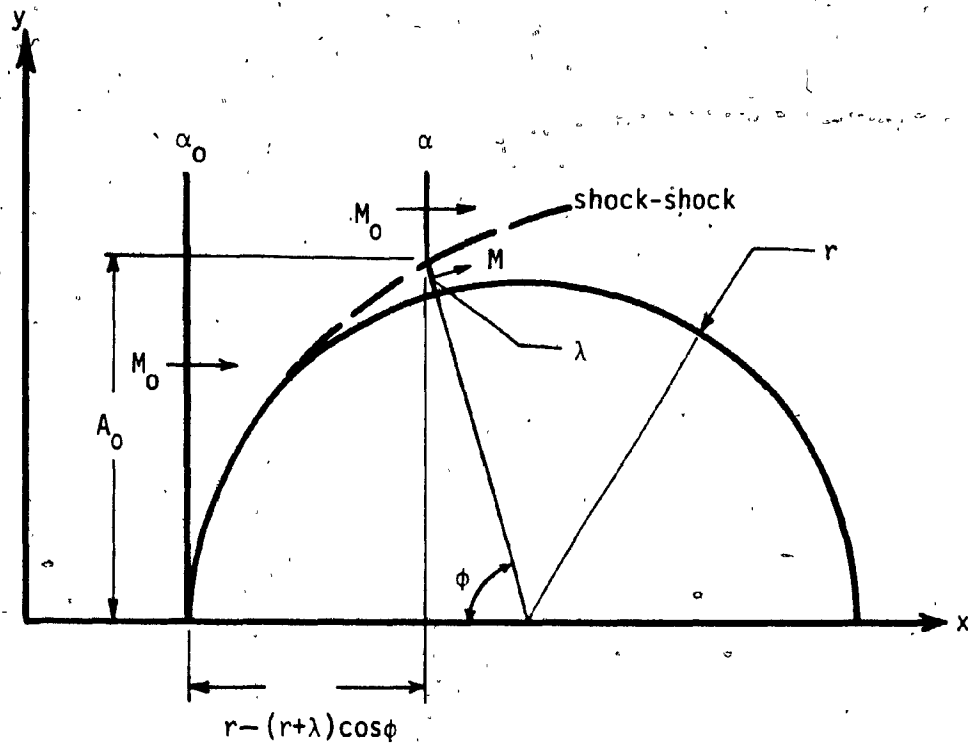


Fig. 2.15. Shock-Shock Locus on the Front of a Cylindrical Rod

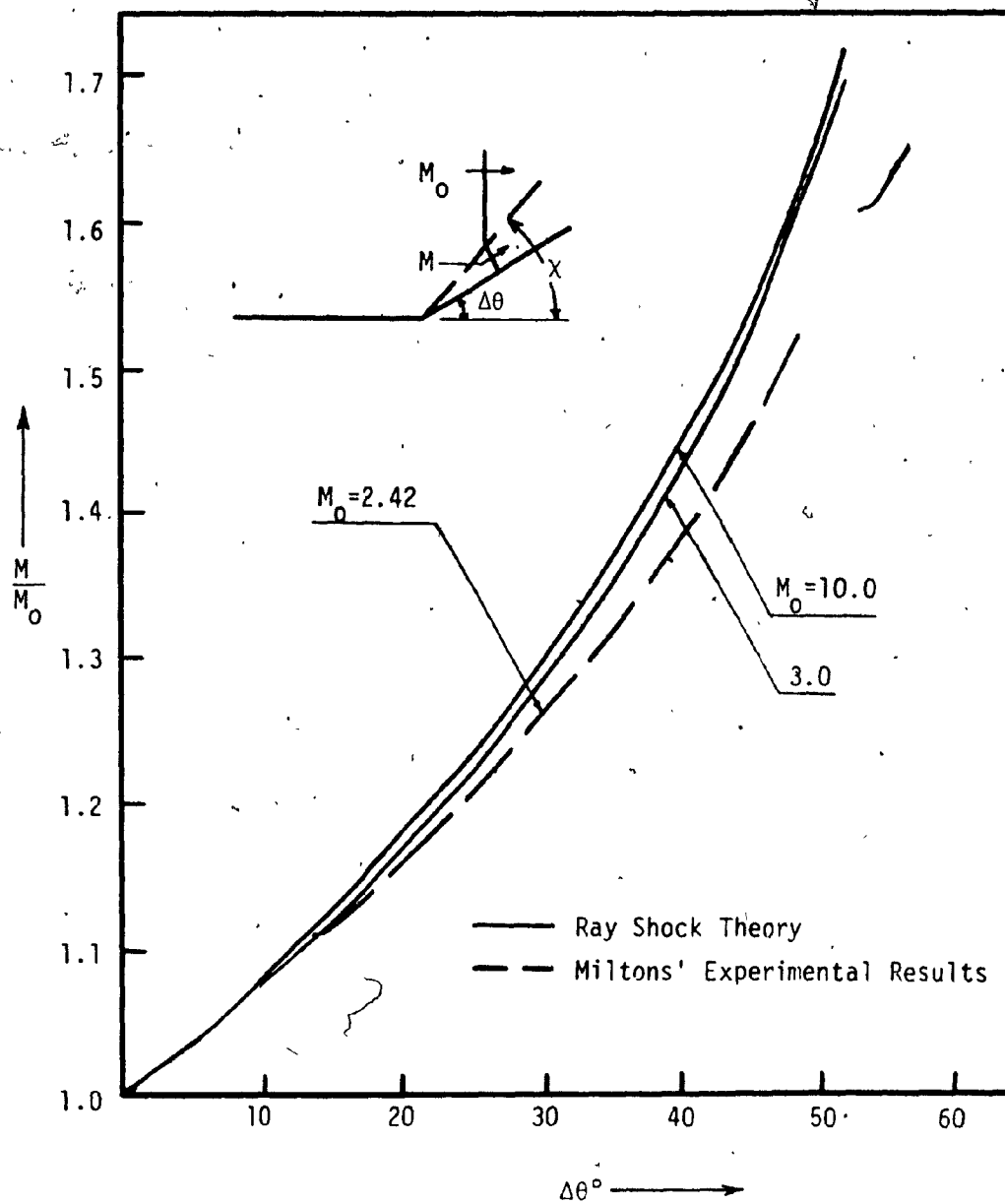


Fig. 2.16. Mach Number Ratio Across Shock-Shock Versus Deflection Angle

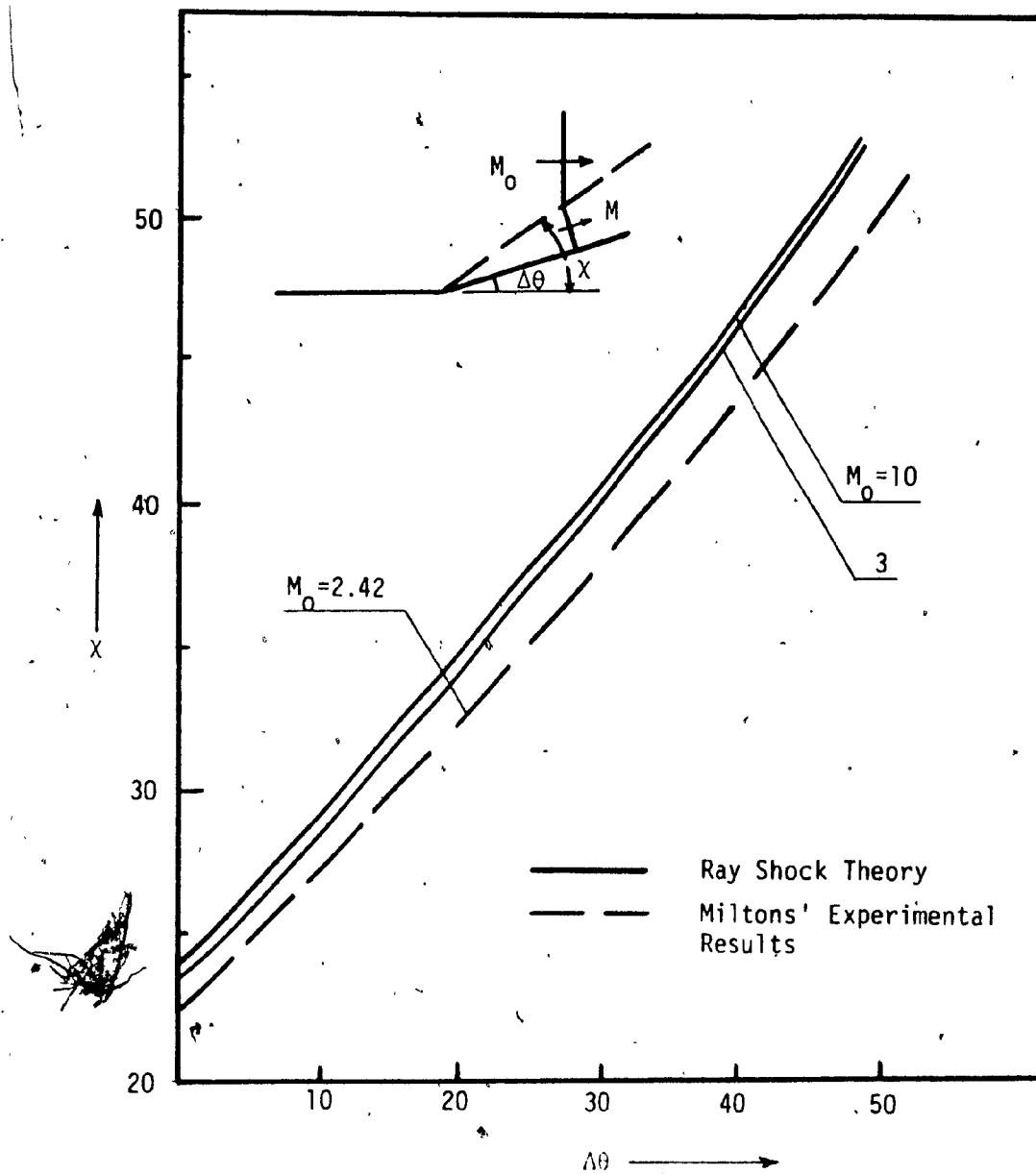


Fig. 2.17. Triple-Point Locus Angle Versus Deflection Angle

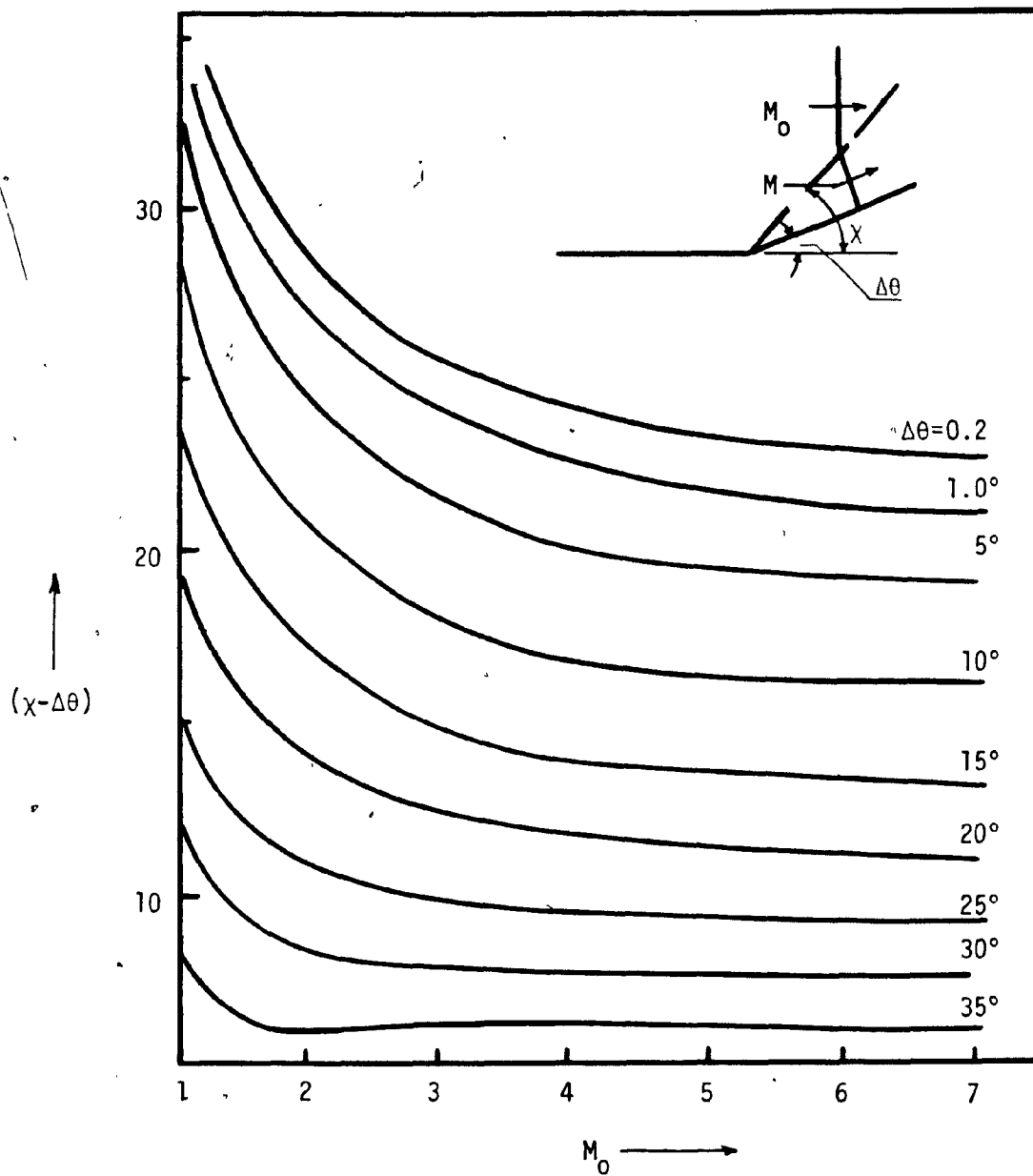


Fig. 2.18. Triple-Point Trajectory Angle Versus Incident Shock Mach number

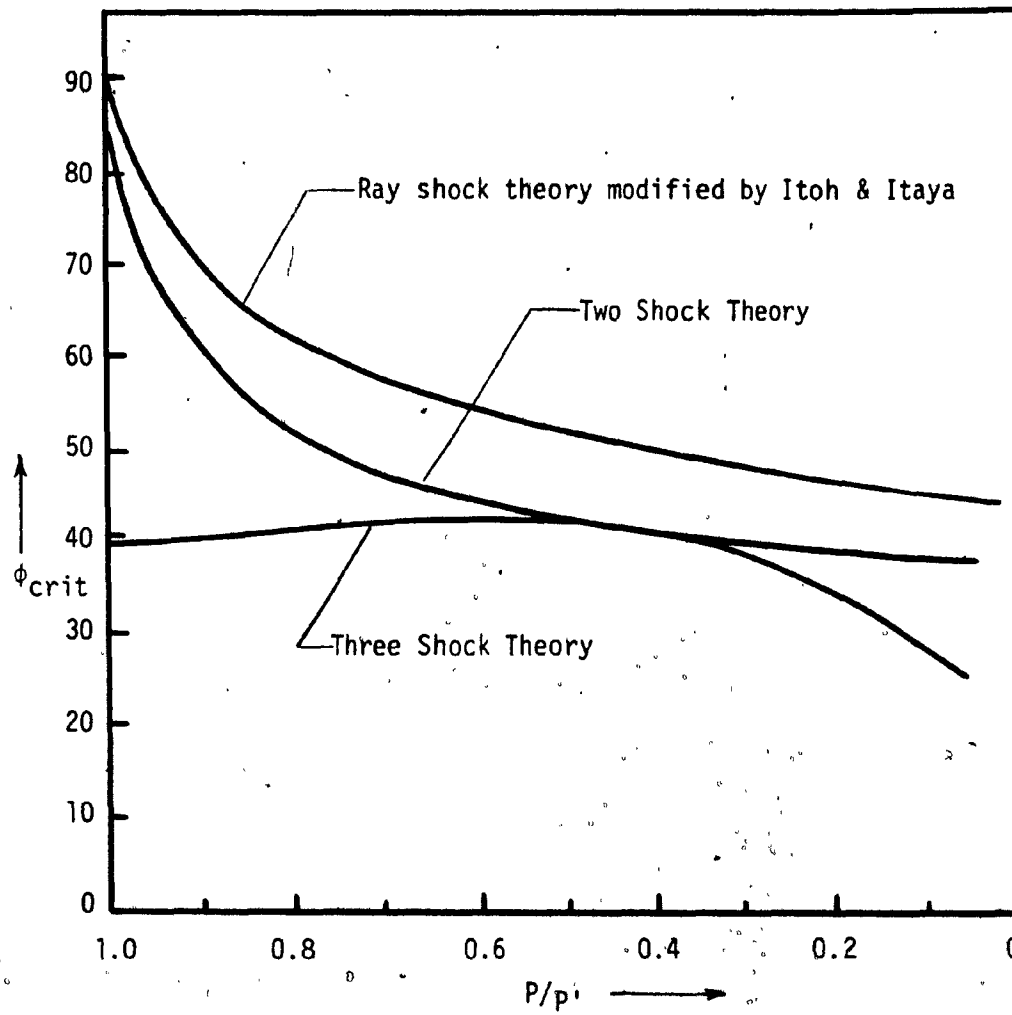
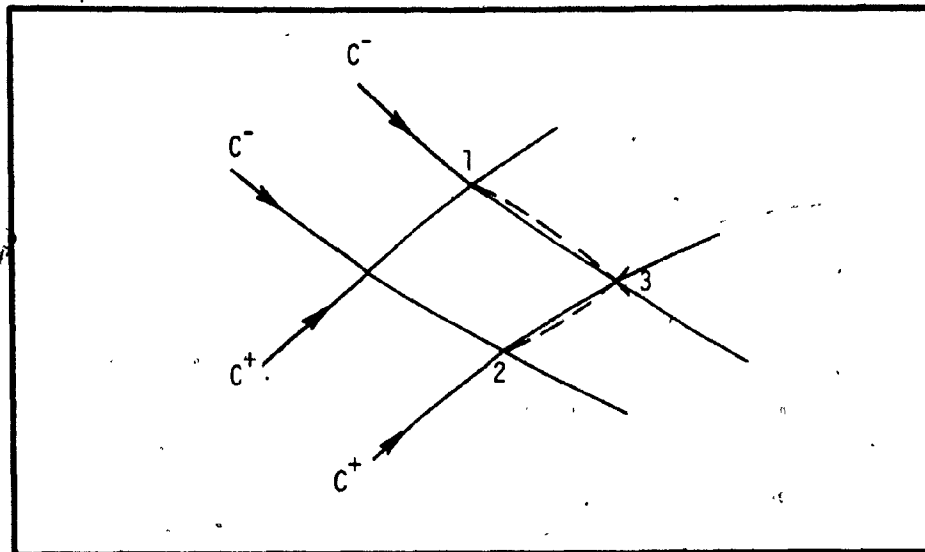
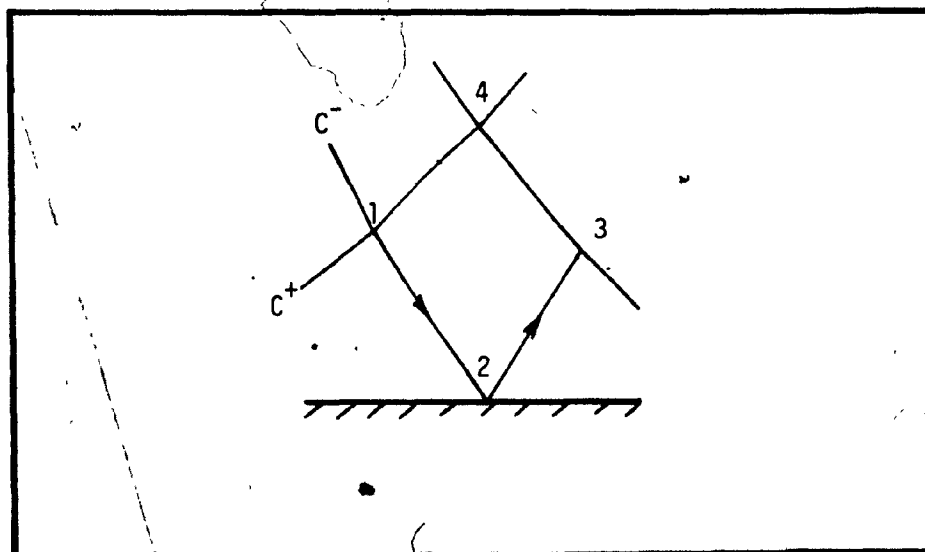


Fig. 2.19. Critical Angle Versus Pressure Ratio Ahead to Rear of the Incident Shock



a) Interaction of Two characteristics



b) Interaction of Characteristic with Plane of Symmetry

Fig. 2.20. Interaction of Characteristics

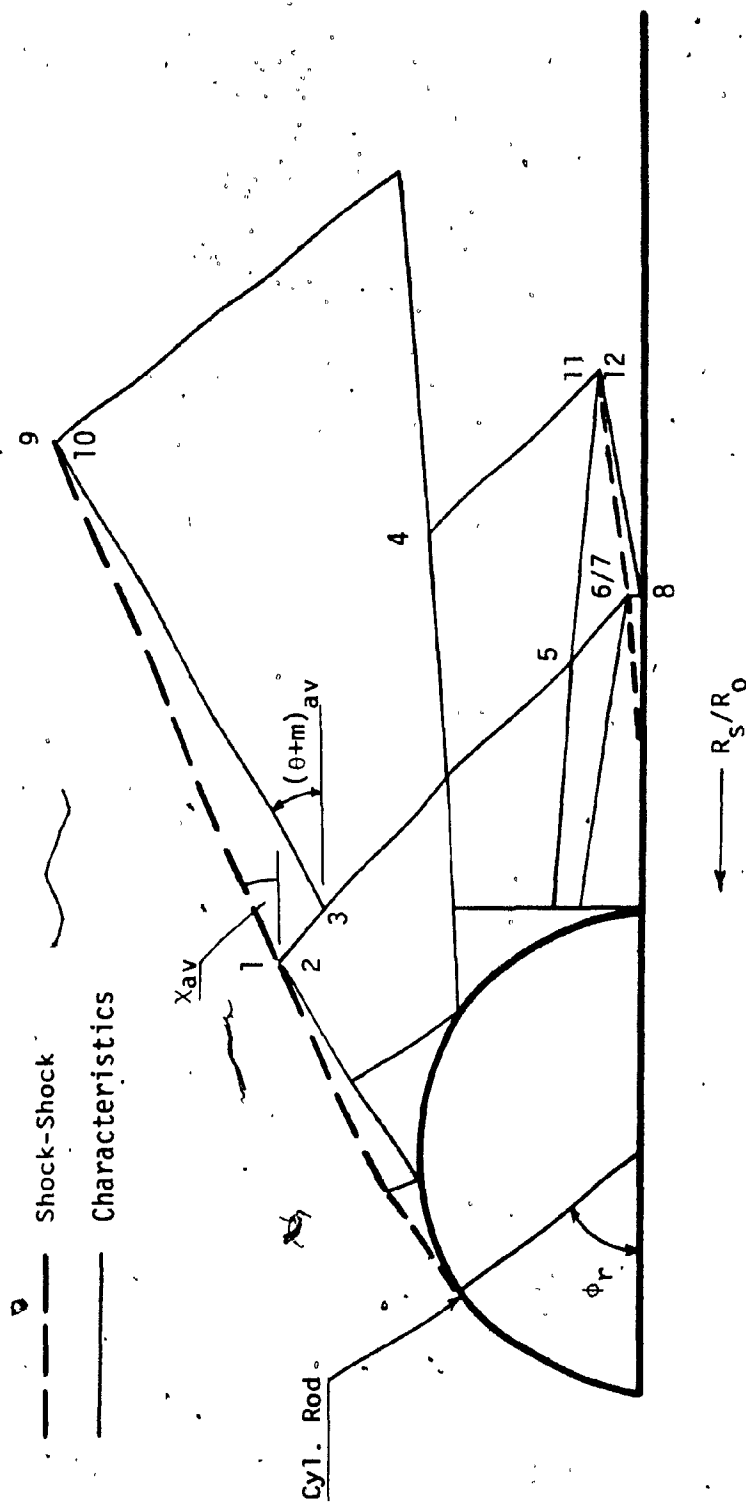


Fig. 2.21. Interaction of Shock Shock with Characteristics

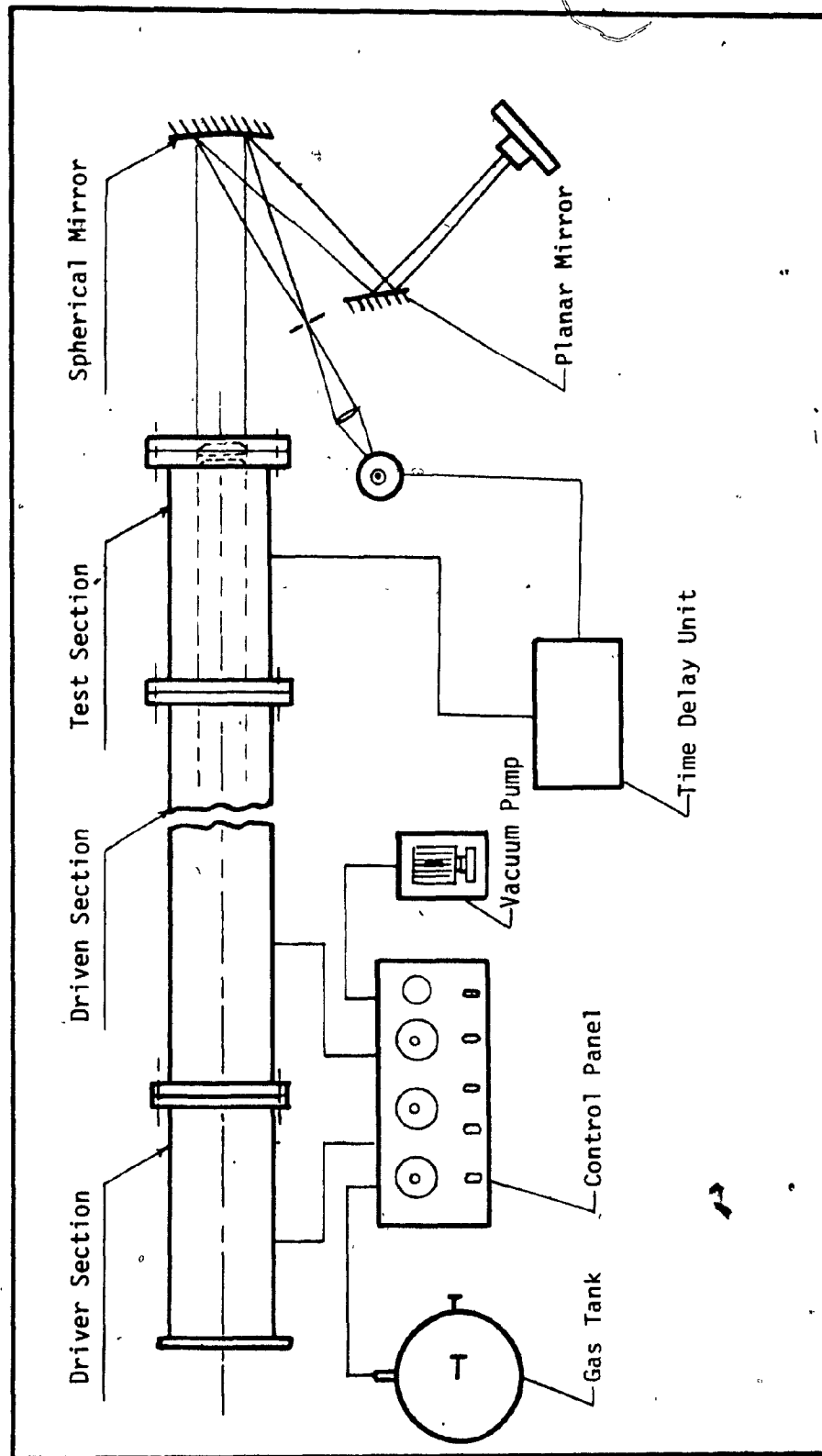


Fig. 3.1. A Schematic Diagram of the Experimental set up

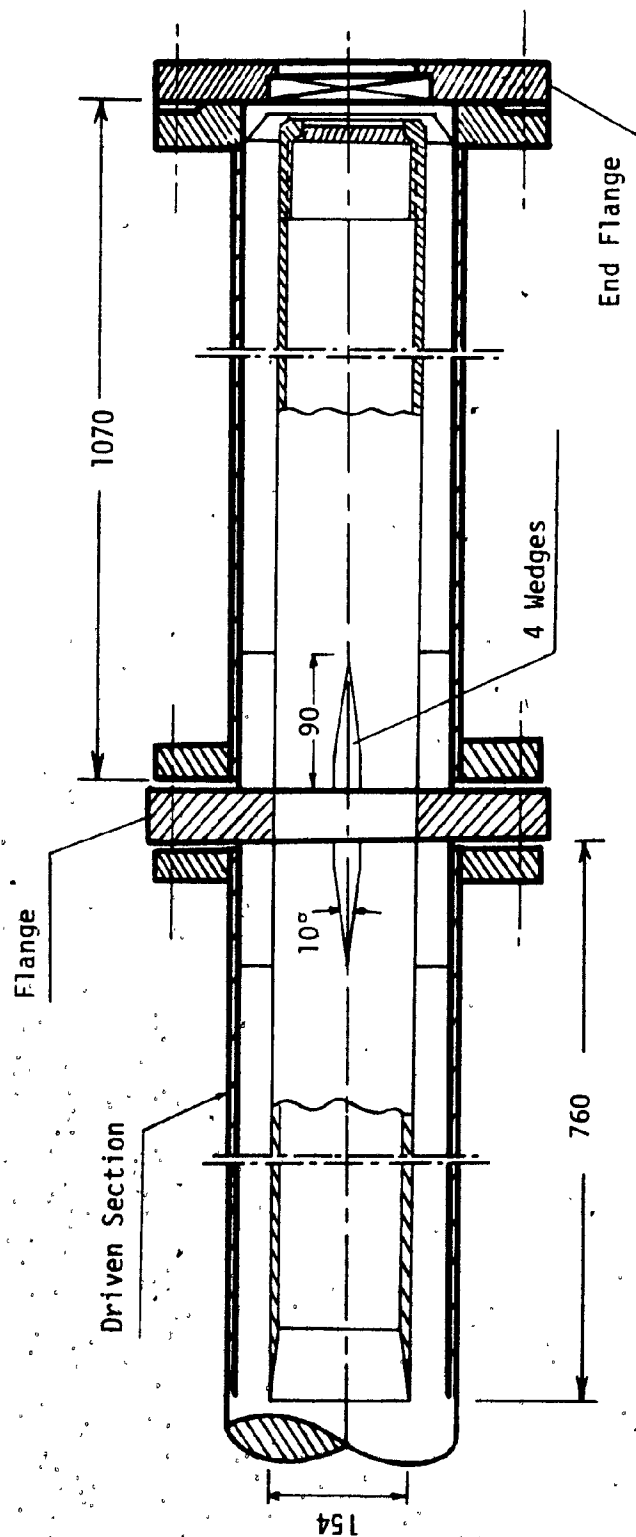


Fig. 3.2. Sectional View of the Test Section

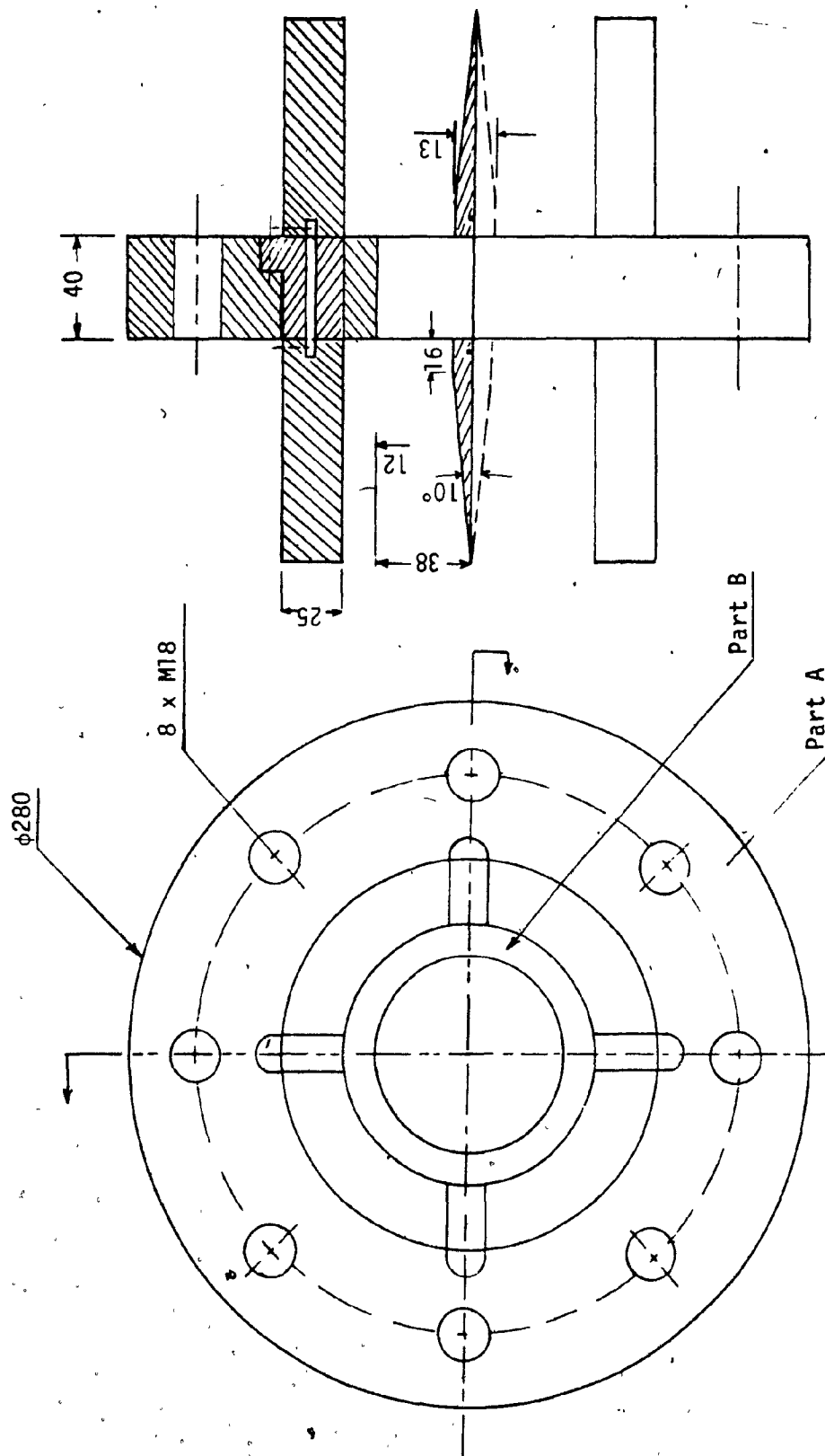


Fig. 3.3. Sectional View of the Flange

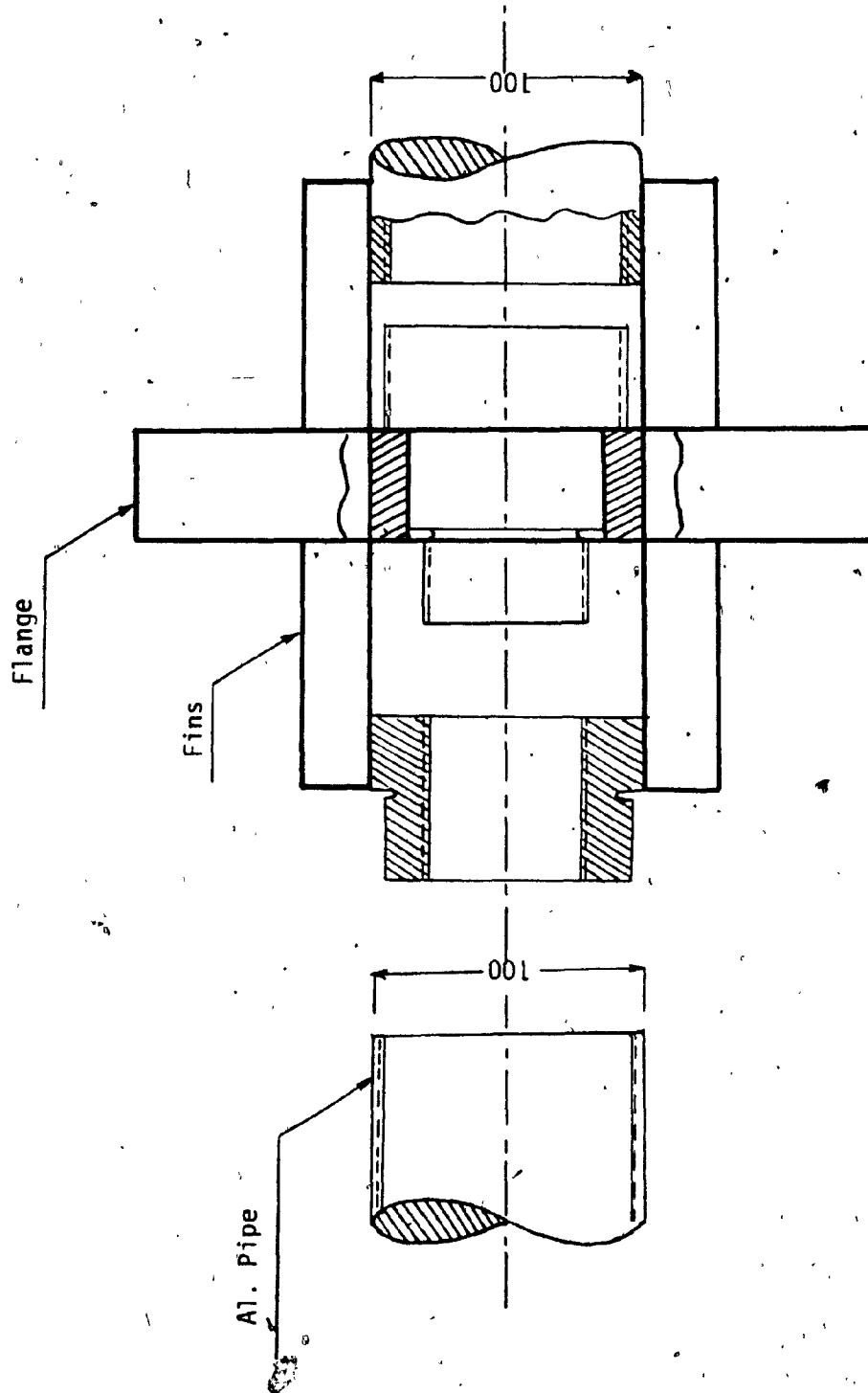


Fig. 3.4. Schematic Sectional View of the Support

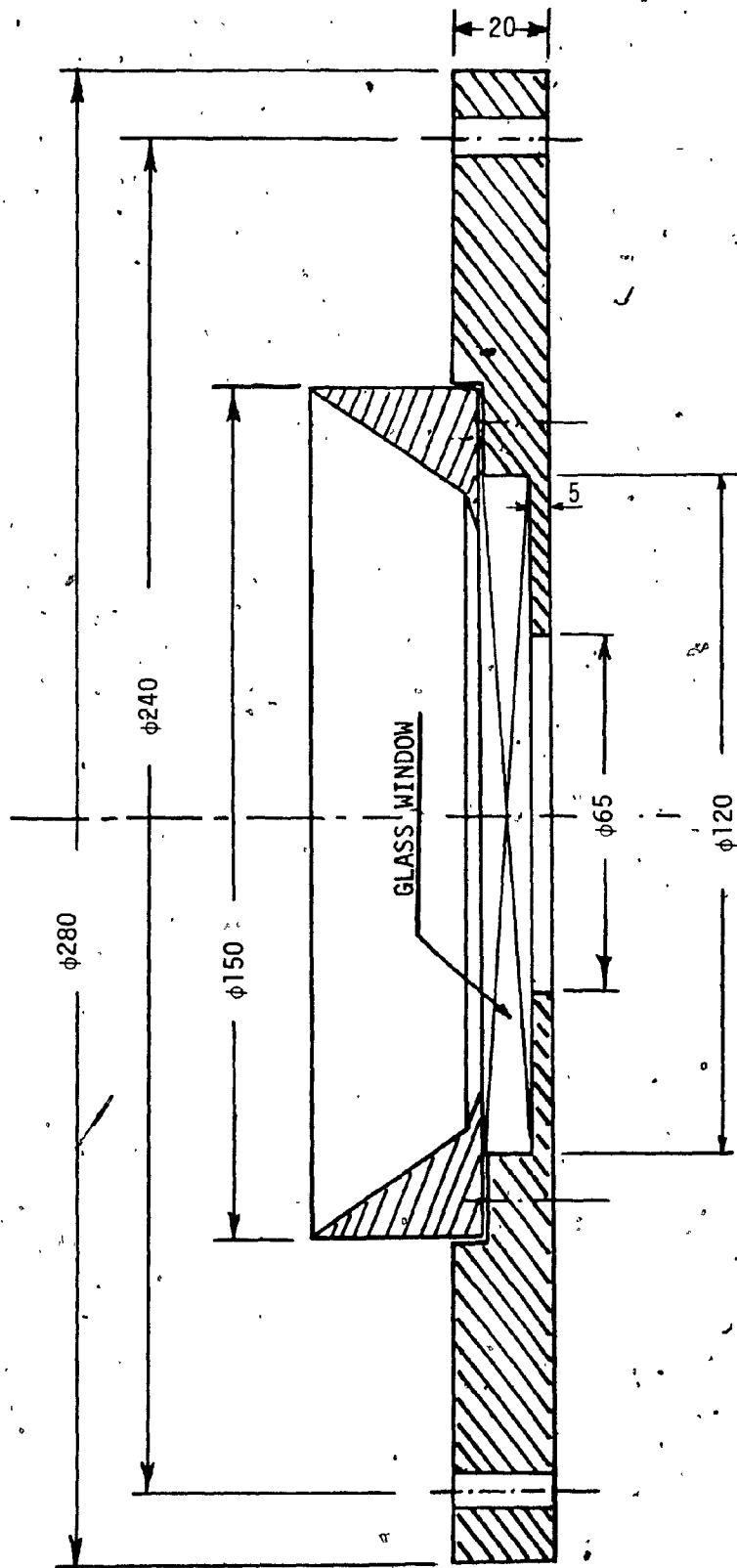


Fig. 3.5. Sectional View of Rear End Plate and Area Contraction..

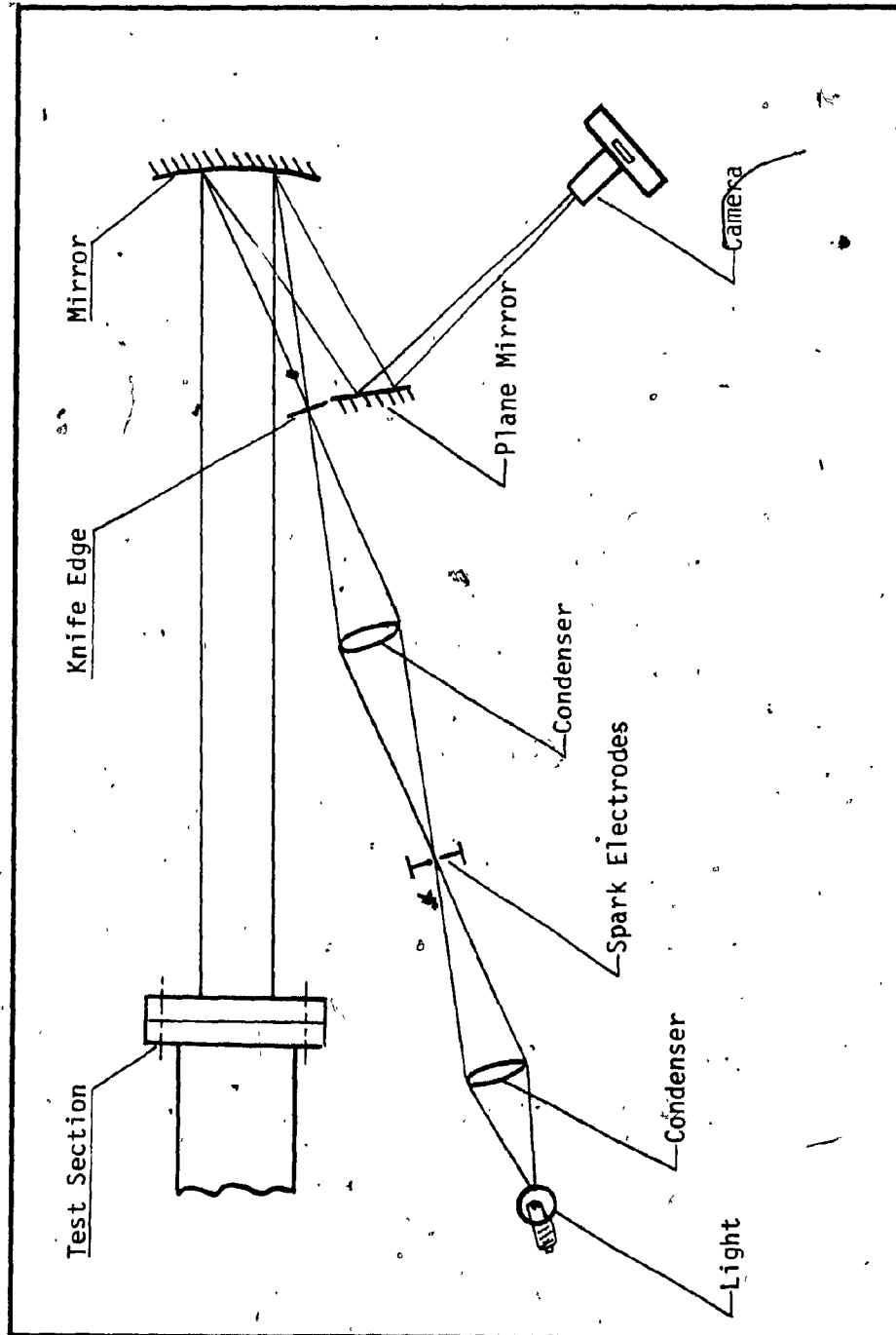


Fig. 3.6. Schematic View of Shadowgraph Photography System

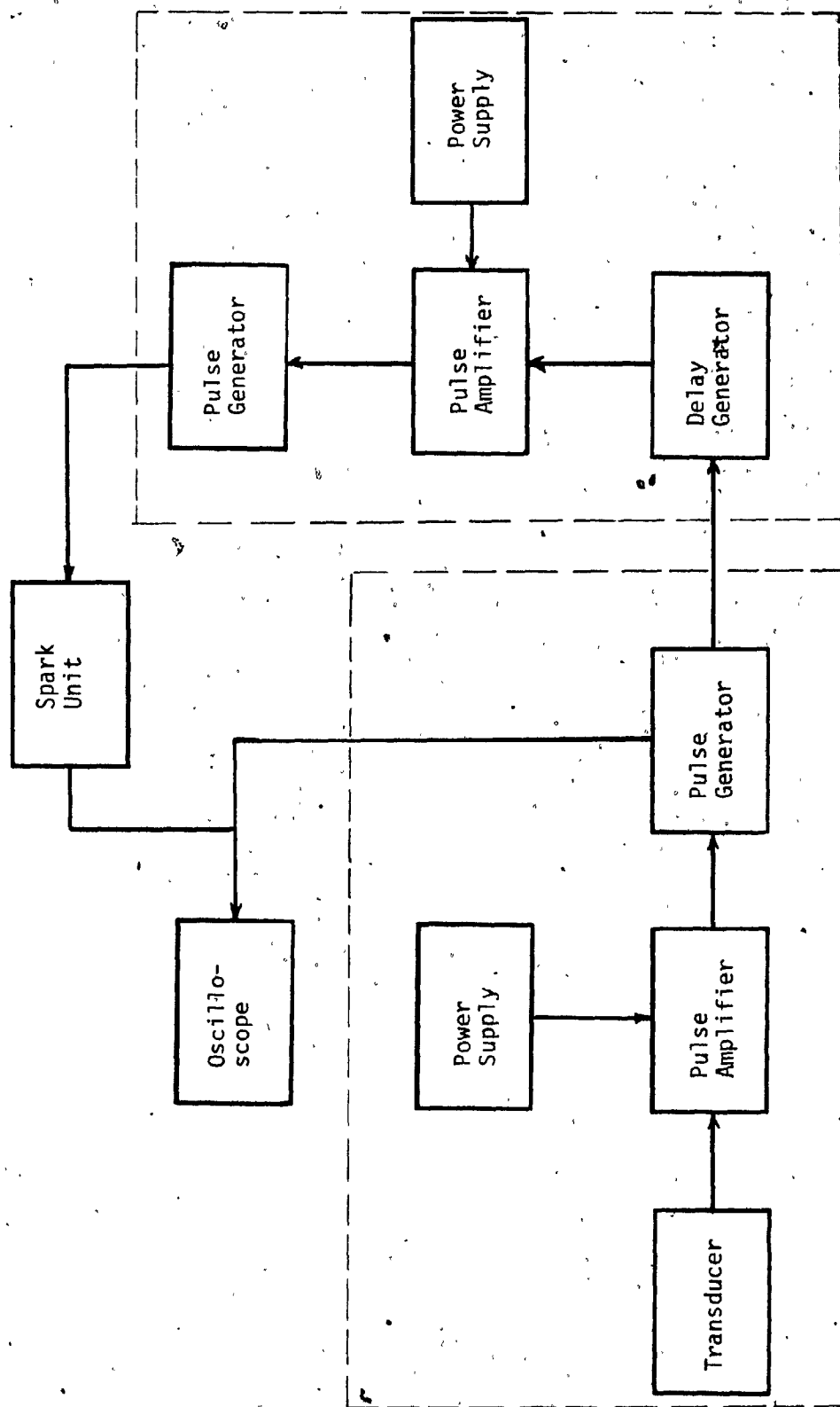
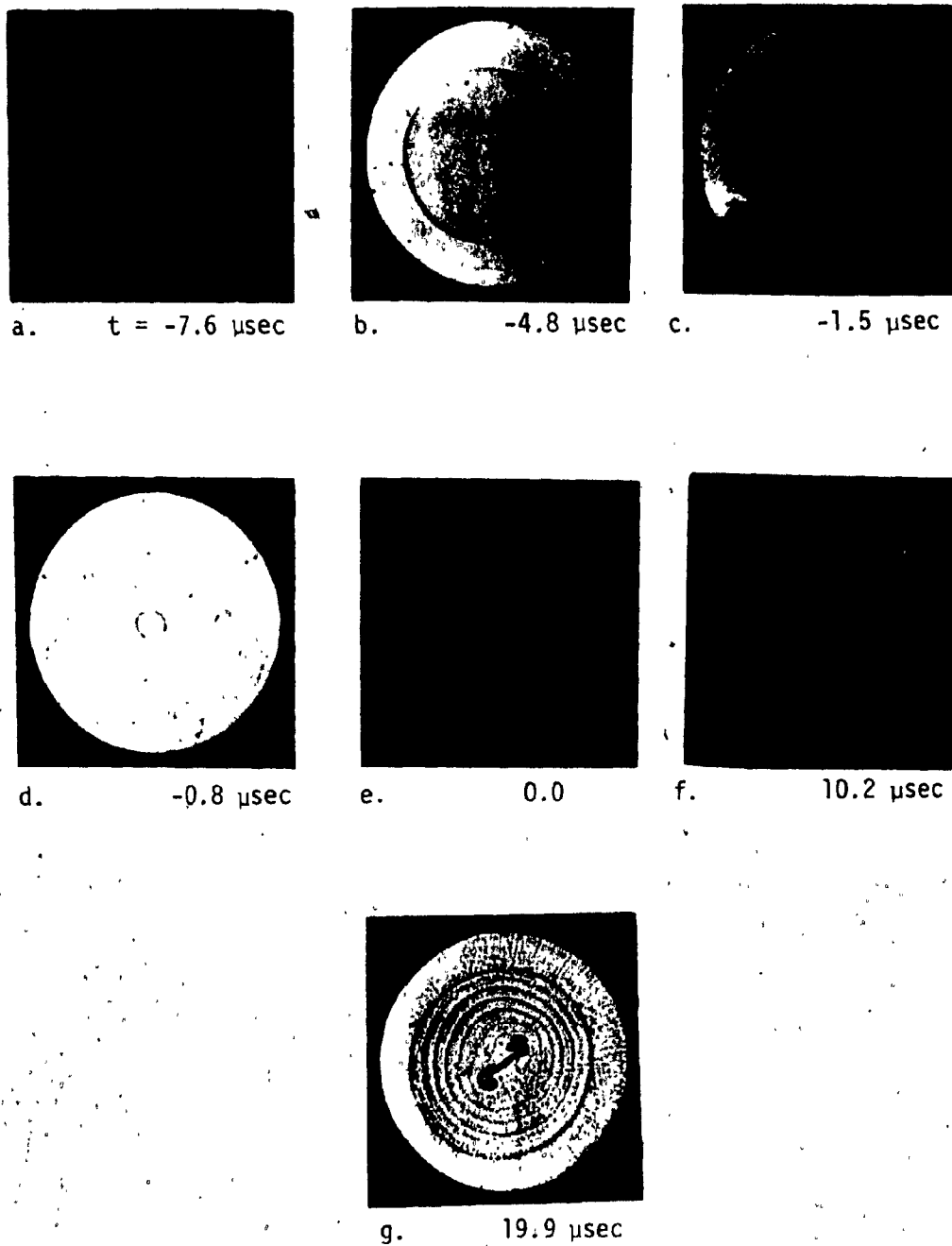


Fig. 3.7. The Time-Delay Spark System




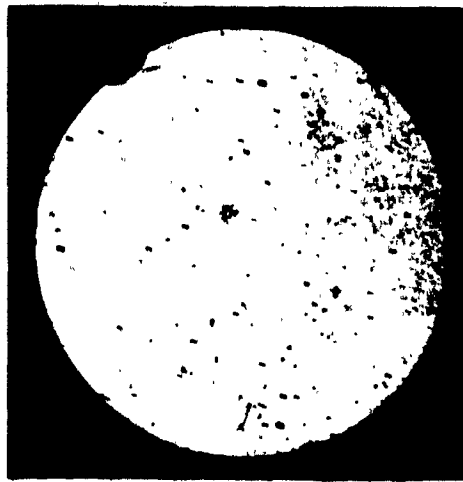
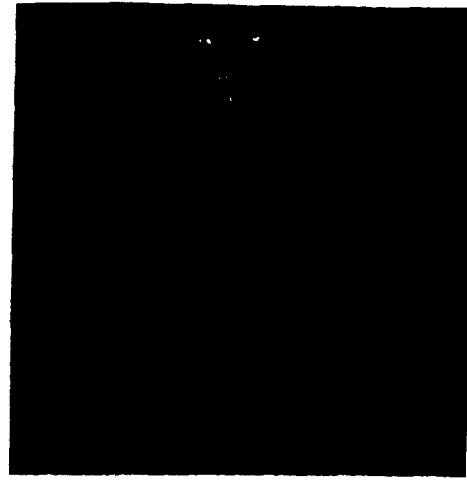
scale:  25 mm

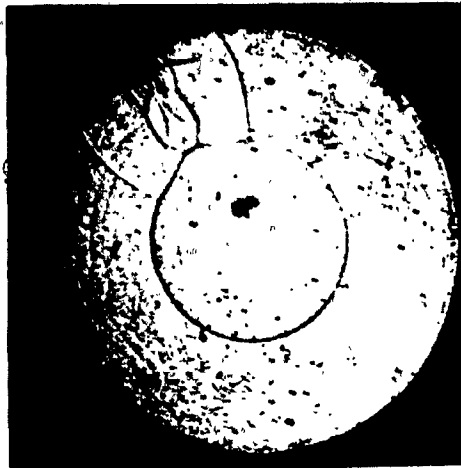
Fig. 4.1. Spark Shadowgraphs Illustrating the propagation of Cylindrical Shock Wave without External perturbations.



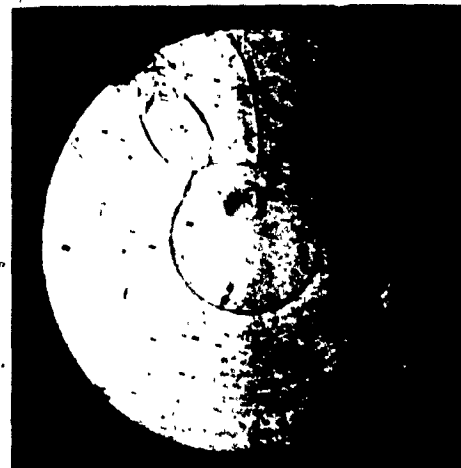
a. No Flow



b. $t = -11 \mu\text{sec}$



c. $-7.3 \mu\text{sec}$



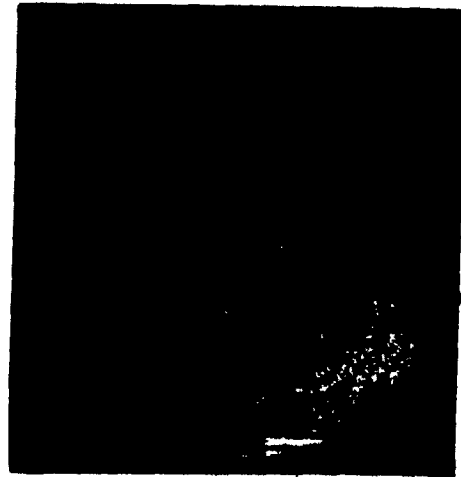
d. $-5.5 \mu\text{sec}$

Fig. 4.2. Spark Shadowgraphs Illustrating the propagation of Cylindrical Shock Wave perturbed by a Rod of Diameter 5 mm, placed at 25 mm from the Geometric Centre.



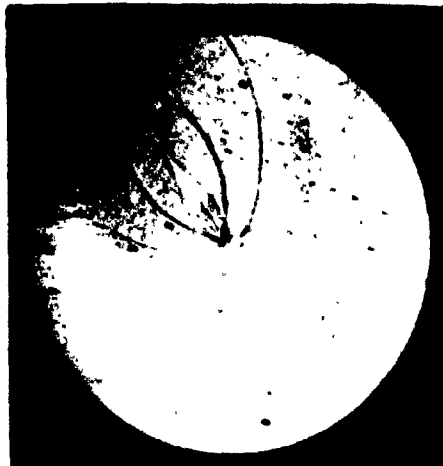
e.

-2 μ sec



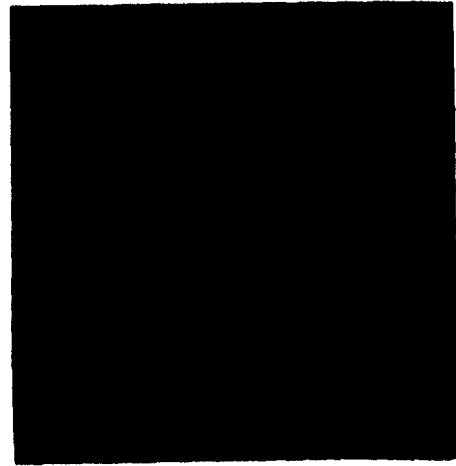
f.

-1.2 μ sec



g.

0.0



h.

8 μ sec


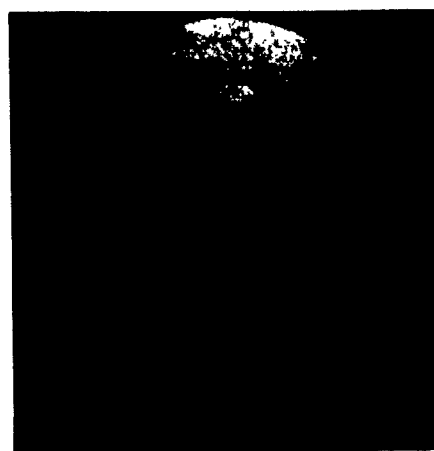
scale:  25 mm

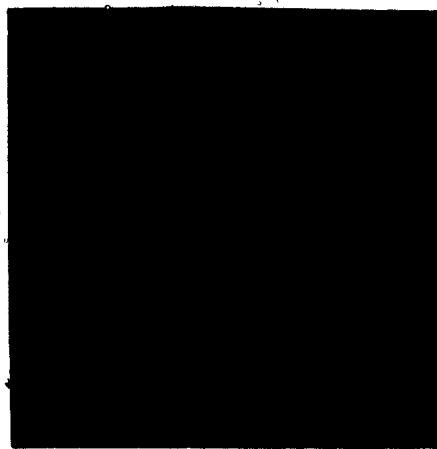
Fig. 4.2. (continued).



a. No Flow



b. $t = -13 \mu\text{sec}$



c. $-10.4 \mu\text{sec}$

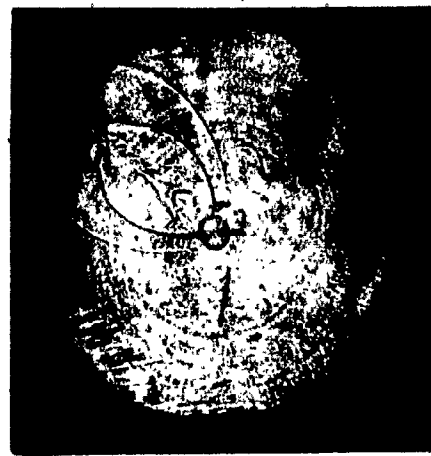


d. $-6.2 \mu\text{sec}$

Fig. 4.3. Spark Shadowgraphs Illustrating the propagation of Cylindrical Shock Wave perturbed by a Rod of Diameter 1.75 mm, placed at 25 mm from the Geometric Centre.



e. -1.7 μ sec



f. -1.1 μ sec



g. 0.0



h. 8 μ sec


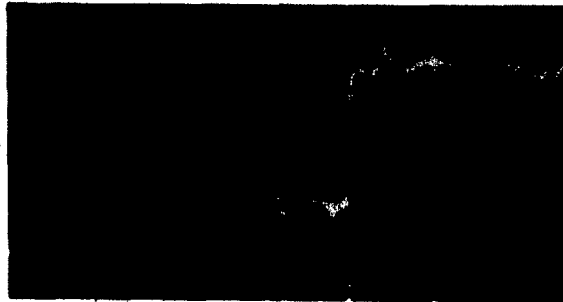
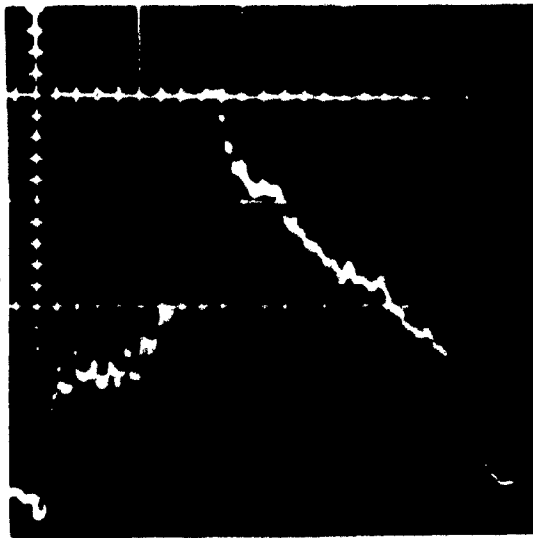
scale:  25 mm

Fig. 4.3. (continued).



a. Plane Shock

500 mV/cm
42.5 mV/psia
vac. pressure = 3.288 psia



b. Cylindrical Shock

1 volt/cm
32.5 mV/psia
vac. pressure = 3.288 psia

Fig. 4.4. Pressure Traces by a Transducer to determine the Local Mach numbers.

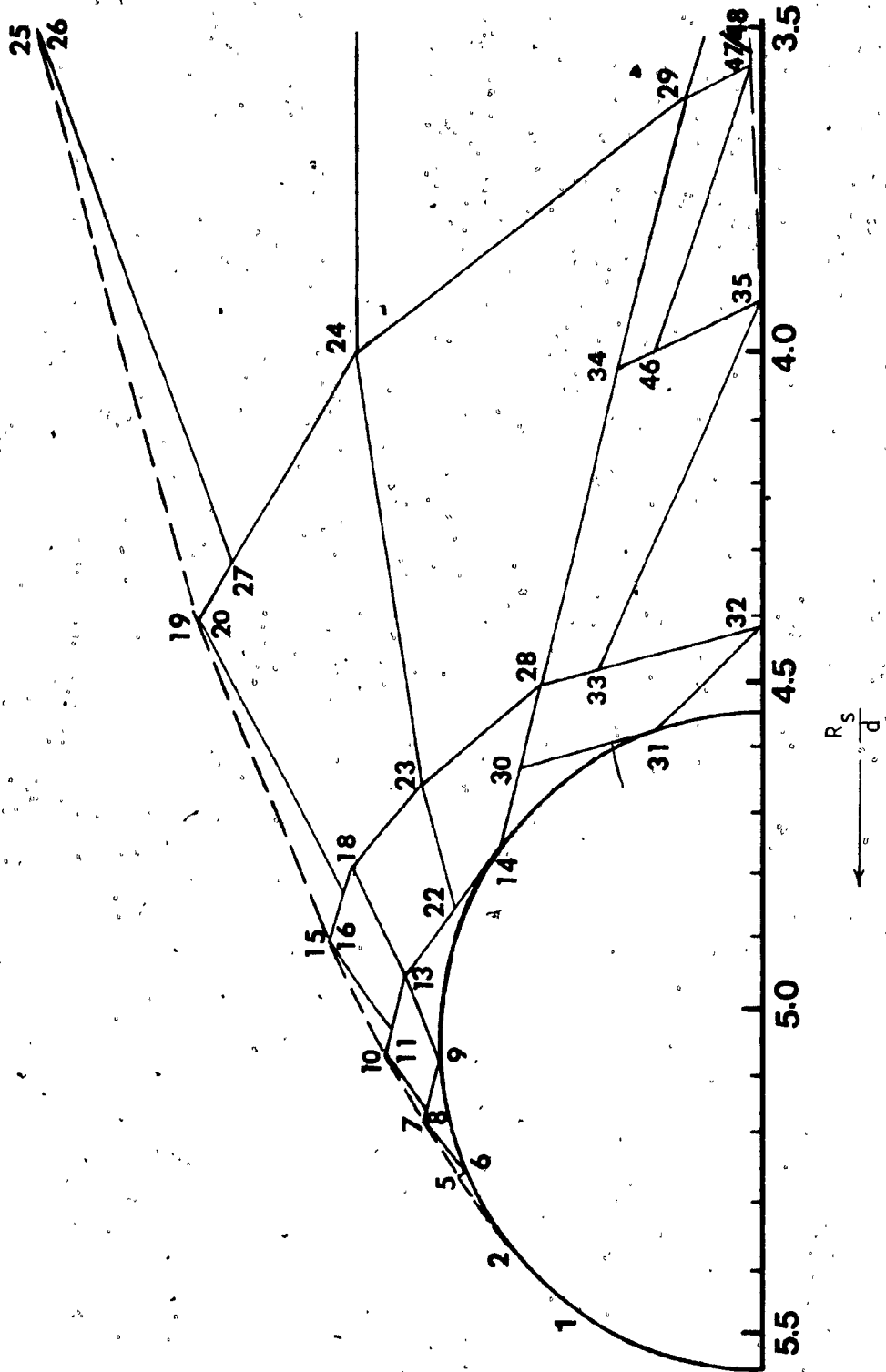


Fig. 4.5. Upper Half of the Wave Diagram Illustrating the Initial Construction for Initial Mach Number 3 and Rod Diameter 5 mm.

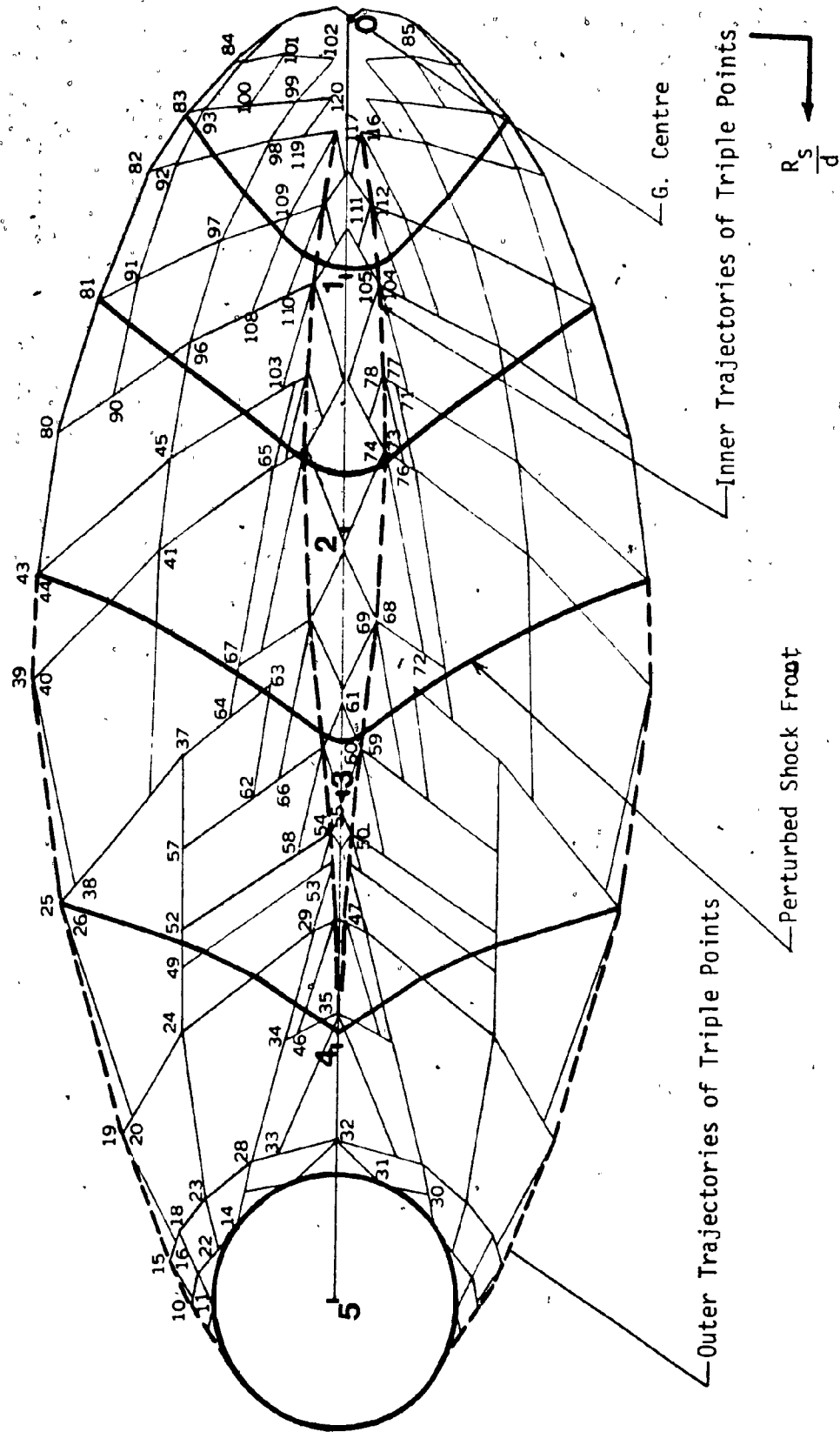


Fig. 4.6. The Wave Diagram Illustrating the Successive Positions of a Strong Shock Perturbed by a Cylindrical Rod of a Diameter 5 mm.

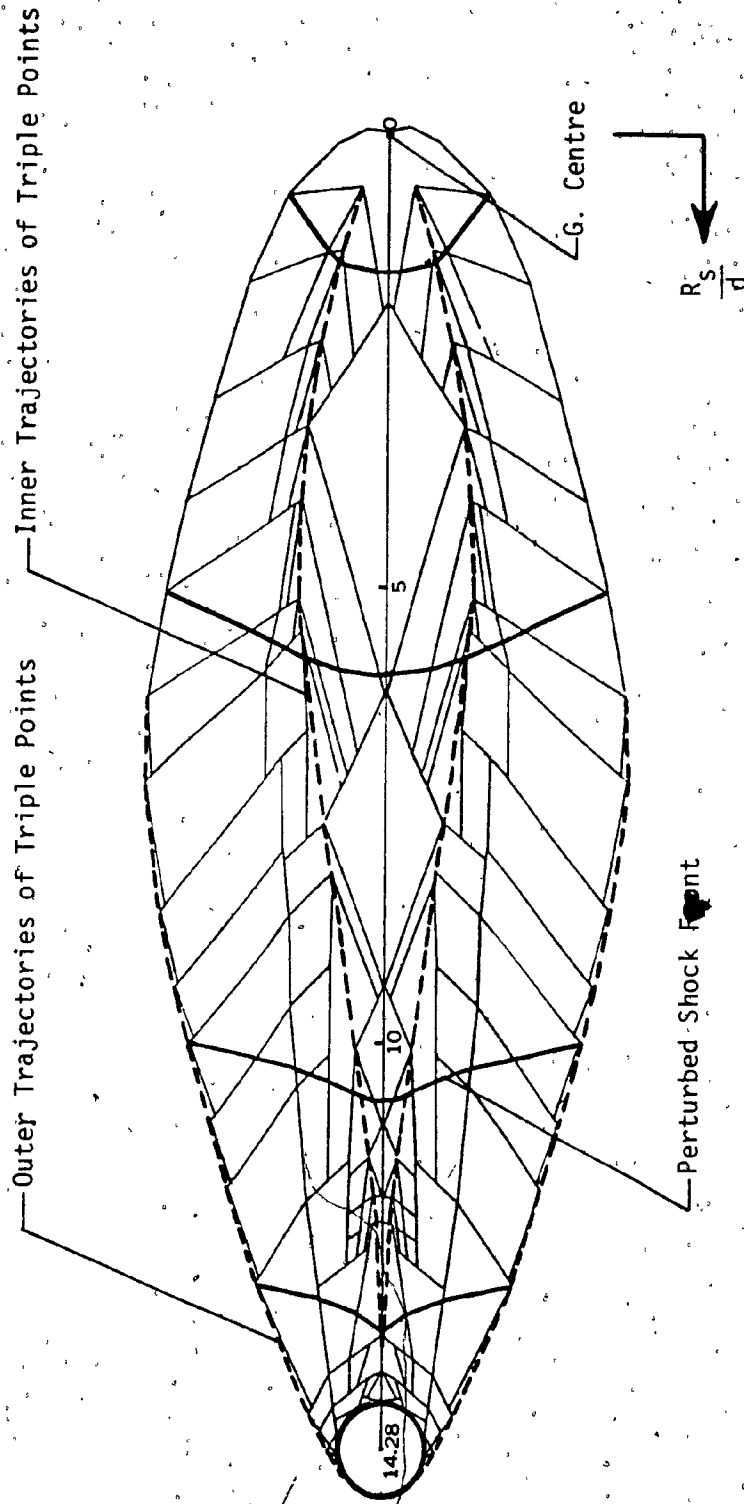


Fig. 4:7. Wave Diagram Illustrating the Successive Positions of a Strong Cylindrical Shock Wave Perturbed by a Rod of Diameter 1.75 mm.

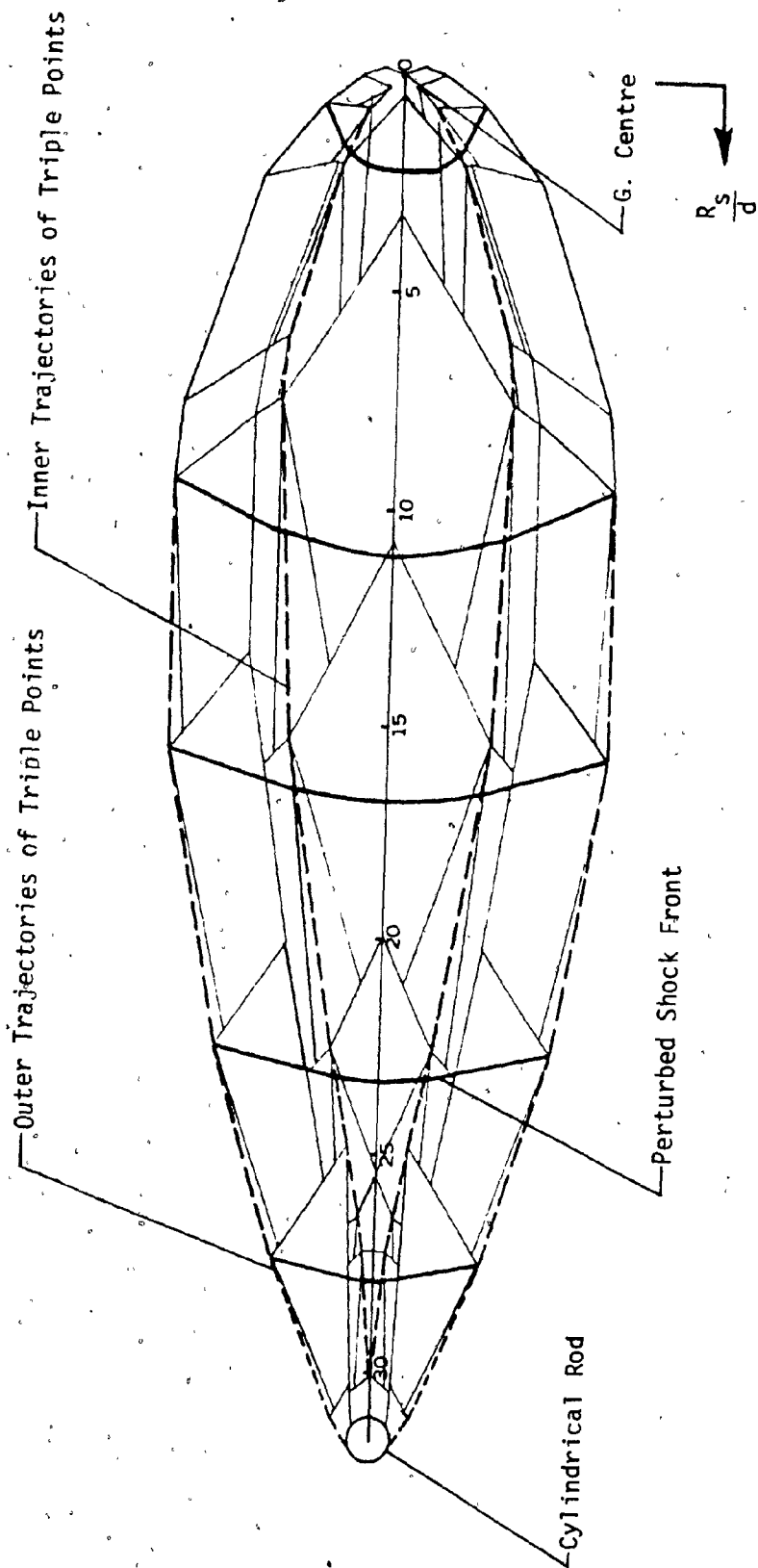


Fig. 4.8. Wave Diagram Illustrating the Successive Positions of a Strong Cylindrical Shock Perturbed by a Cylindrical Rod of Diameter 0.8 mm.

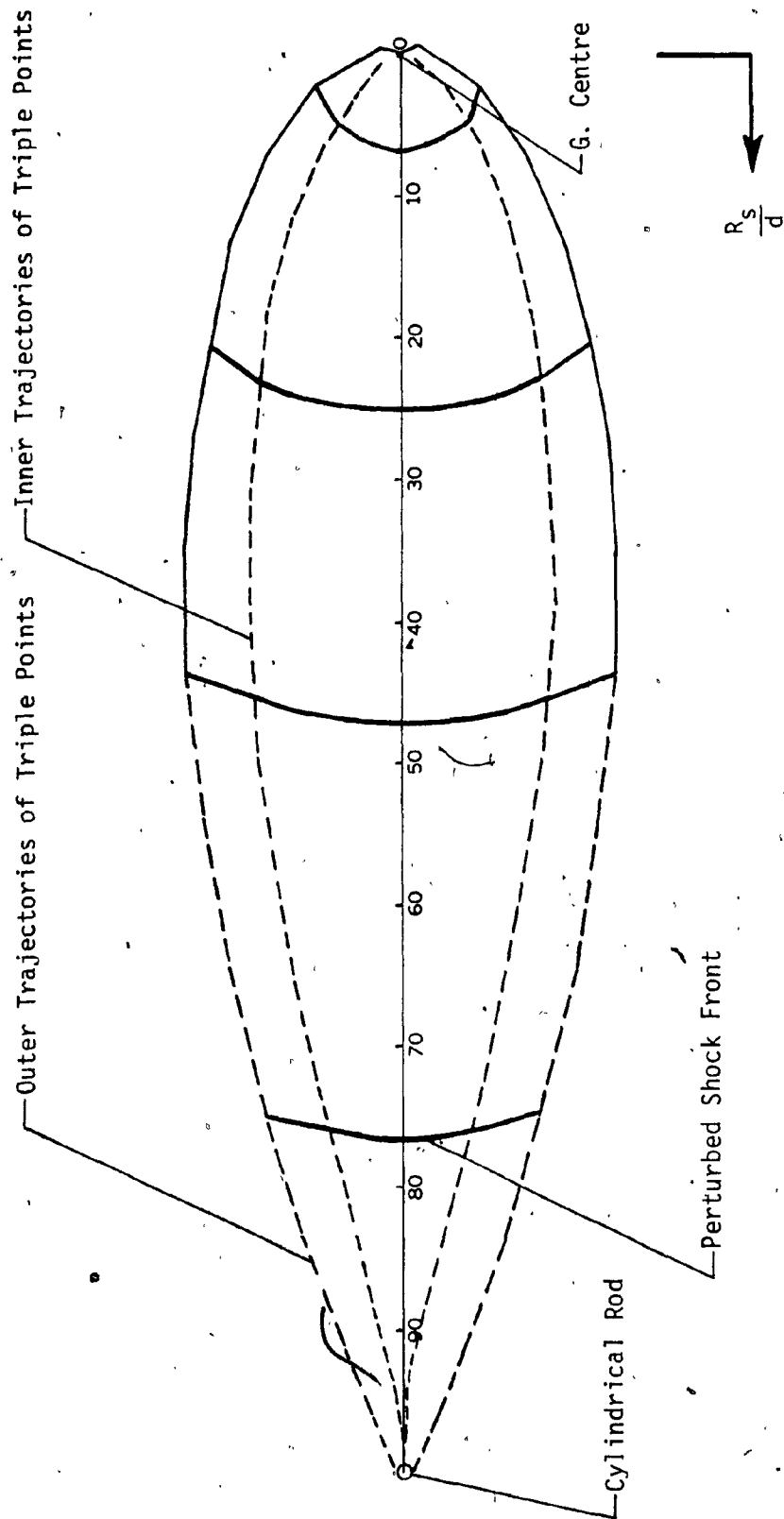


Fig. 4.9. Wave Diagram Illustrating the Successive Positions of a Strong Shock Perturbed by a Cylindrical Rod of Diameter 0.25 mm.

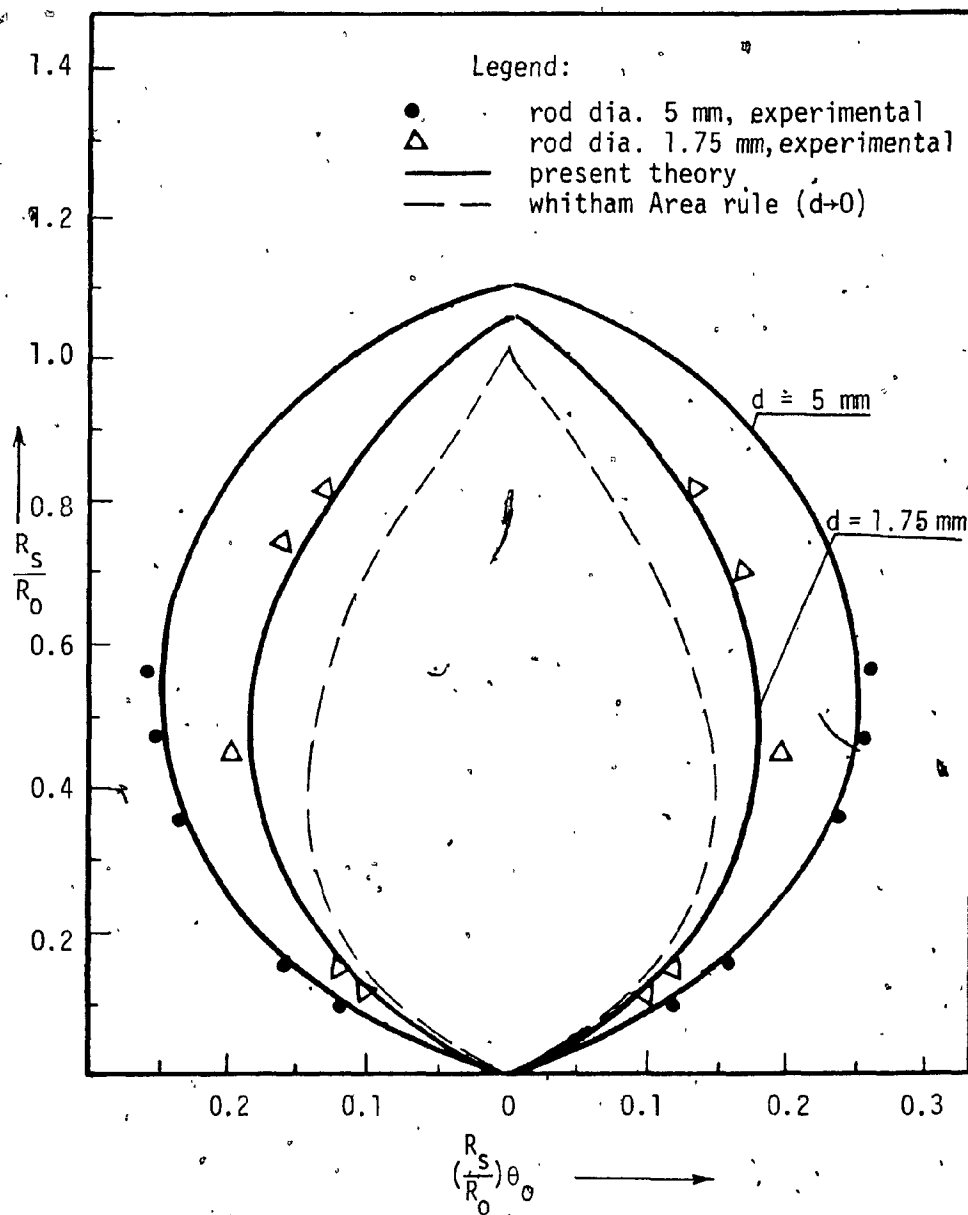


Fig. 4.10. Outer trajectories of the Triple Points of Converging Cylindrical Shocks, Perturbed by Various sizes of Rod Diameter.

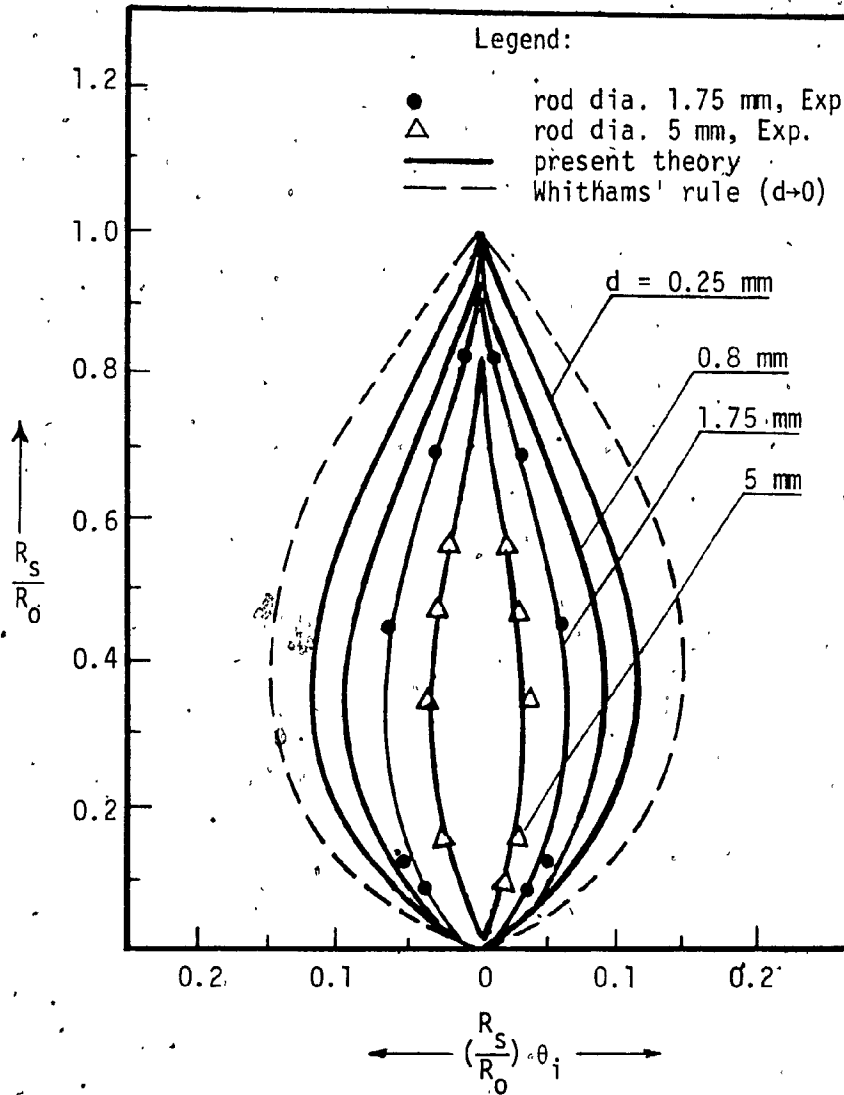


Fig. 4.11. Inner Trajectories of the Triple Points of Converging Cylindrical Shocks, Perturbed by various sizes of Rod Diameters.

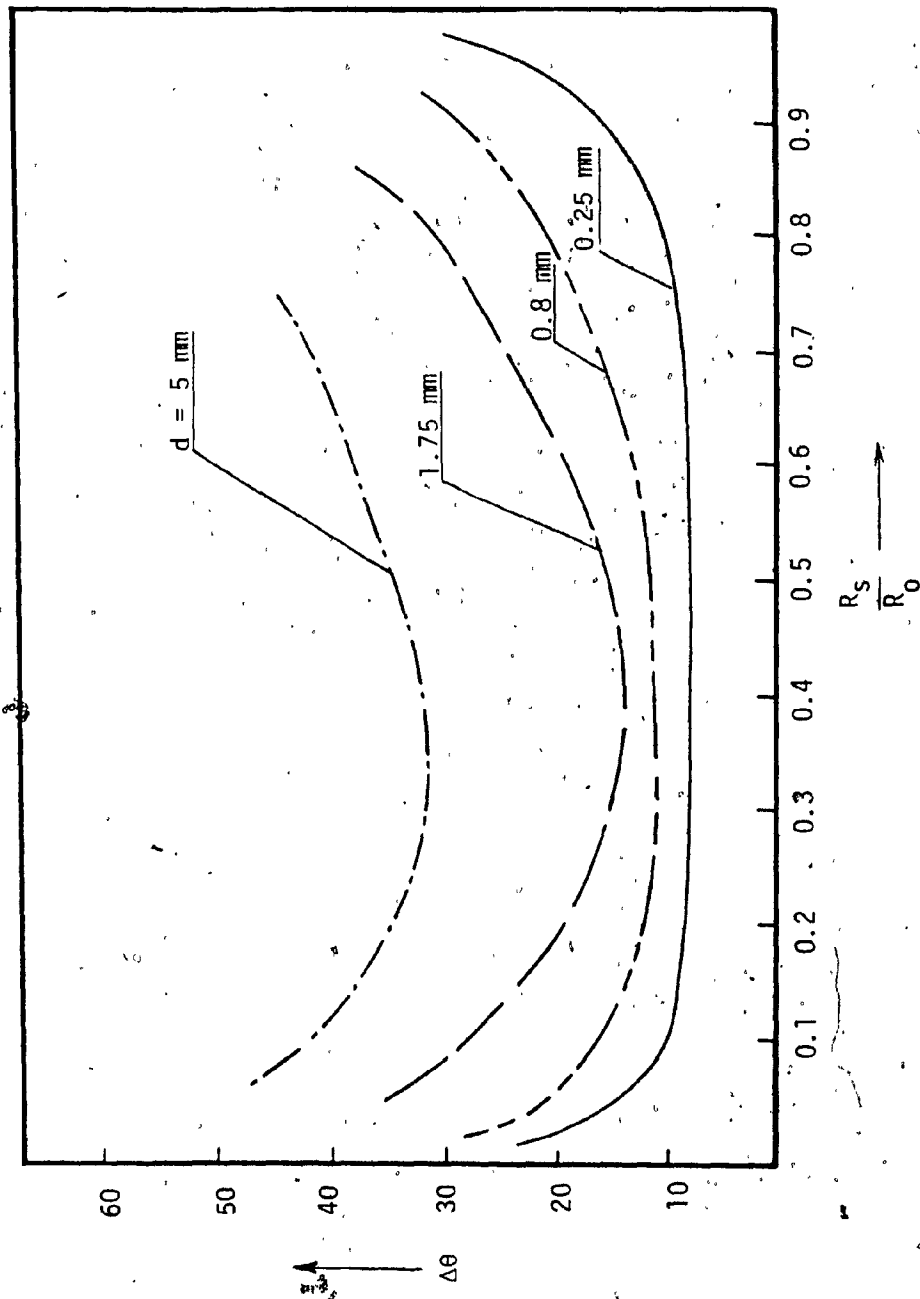


Fig. 4.12. Flow Deflection at the Inner Triple Point vs Shock Radius

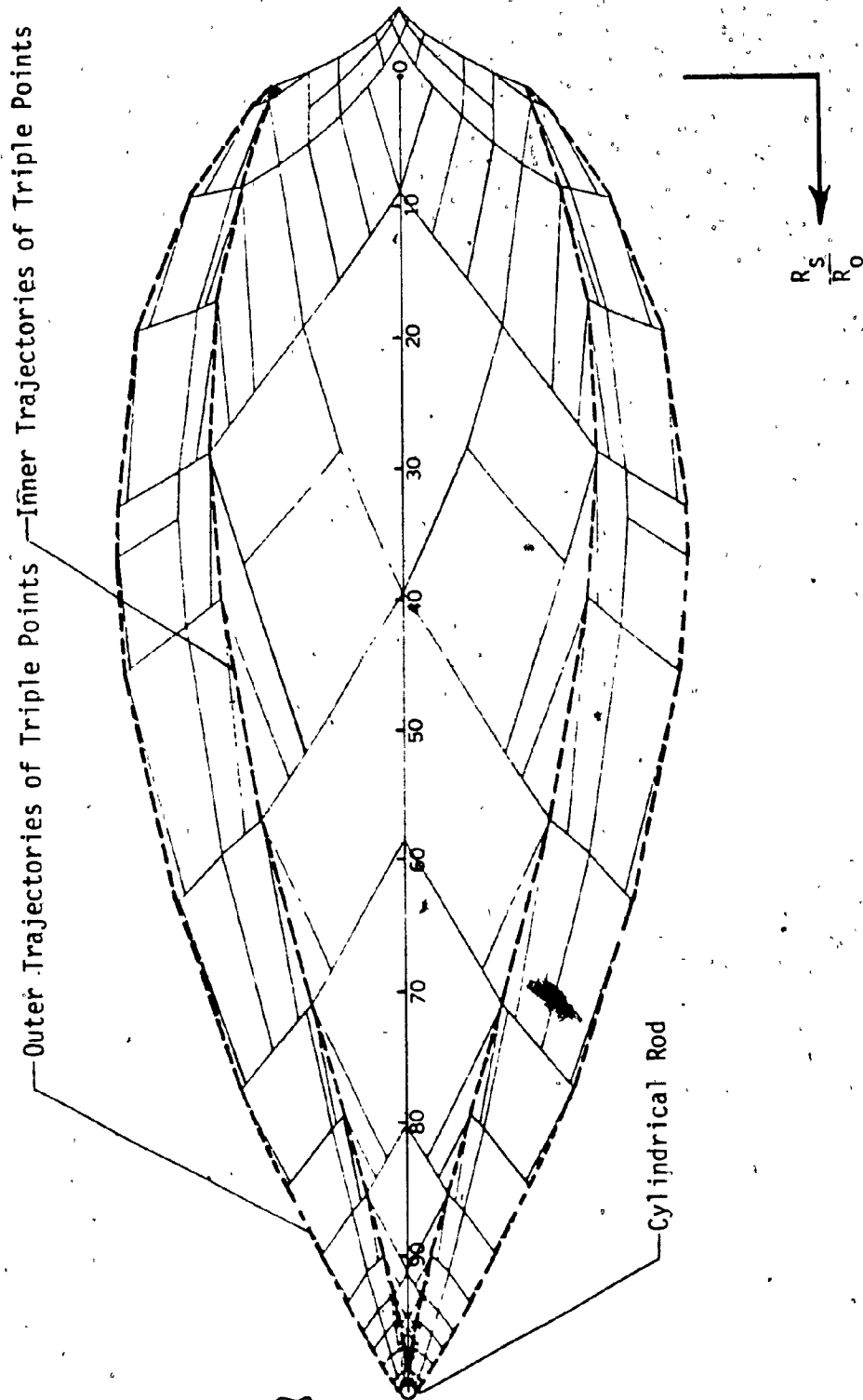


Fig. 4.13. Wave Diagram for the Initially Weak Cylindrical Shock, Perturbed by a Rod of Diameter 0.25 mm.

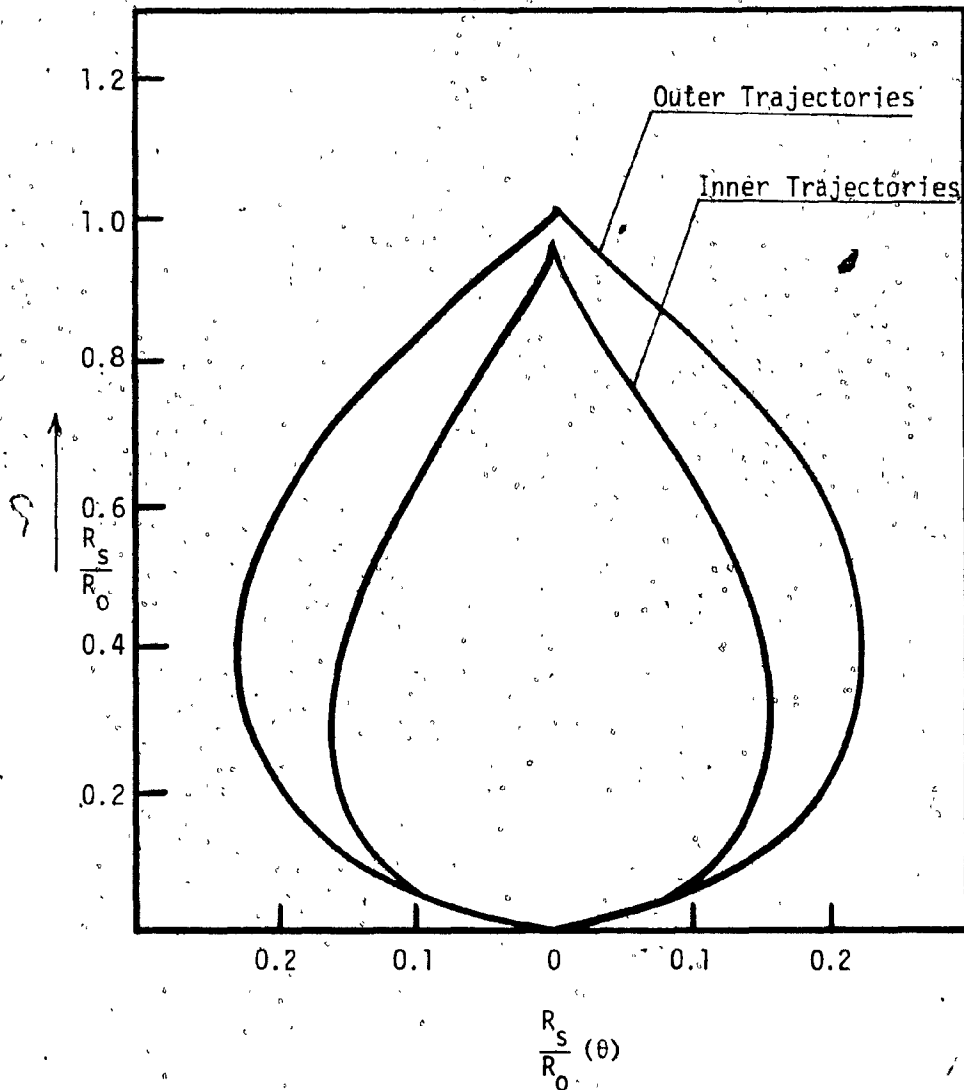


Fig. 4.14. Outer and Inner Trajectories of the Weak Cylindrical Shock Perturbed by a Rod of Diameter 0.25 mm.

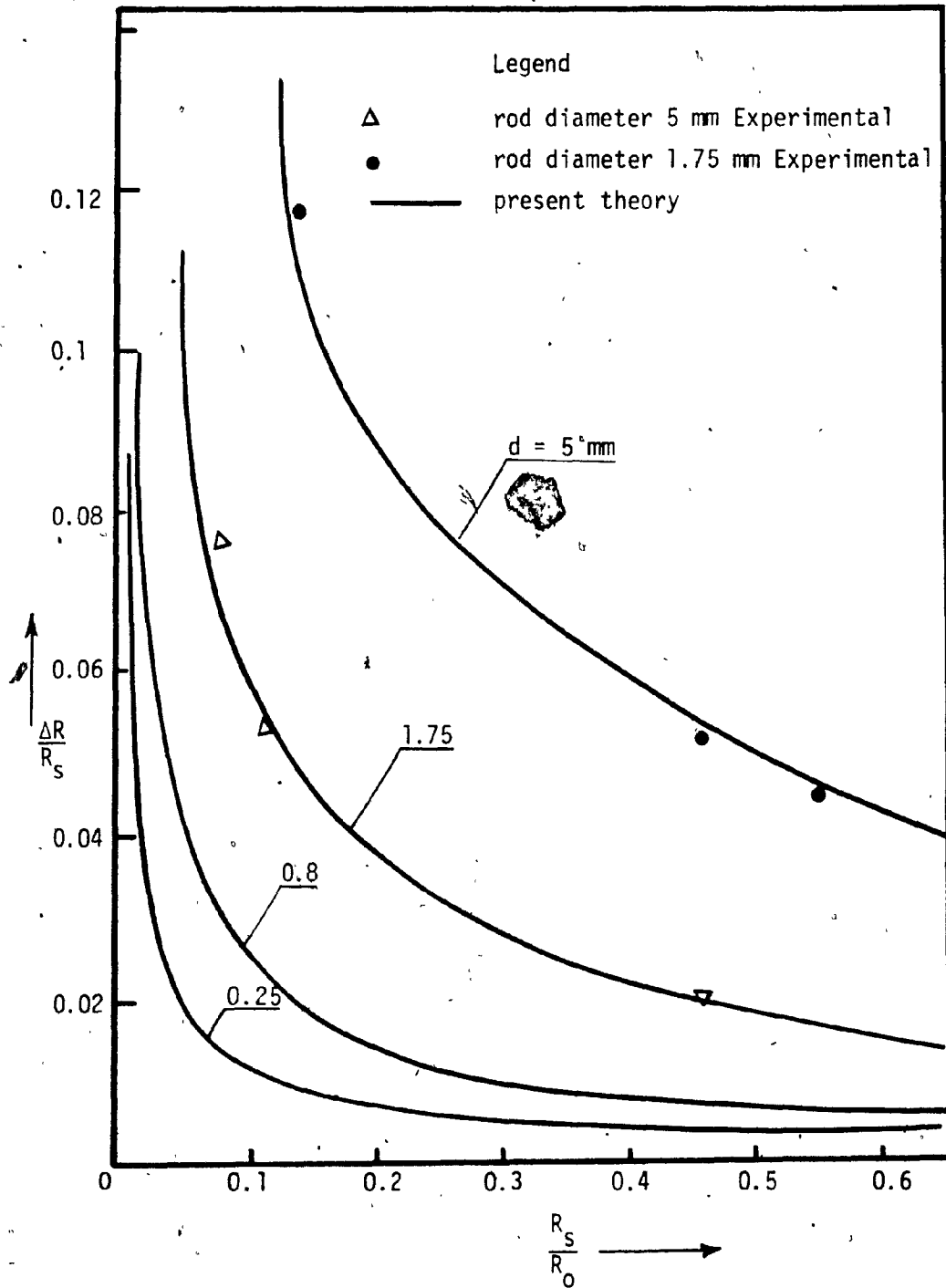


Fig. 4.15. Rate of Growth of Perturbation of Cylindrical Shock, Perturbed by various Sizes of Rod Diameters.

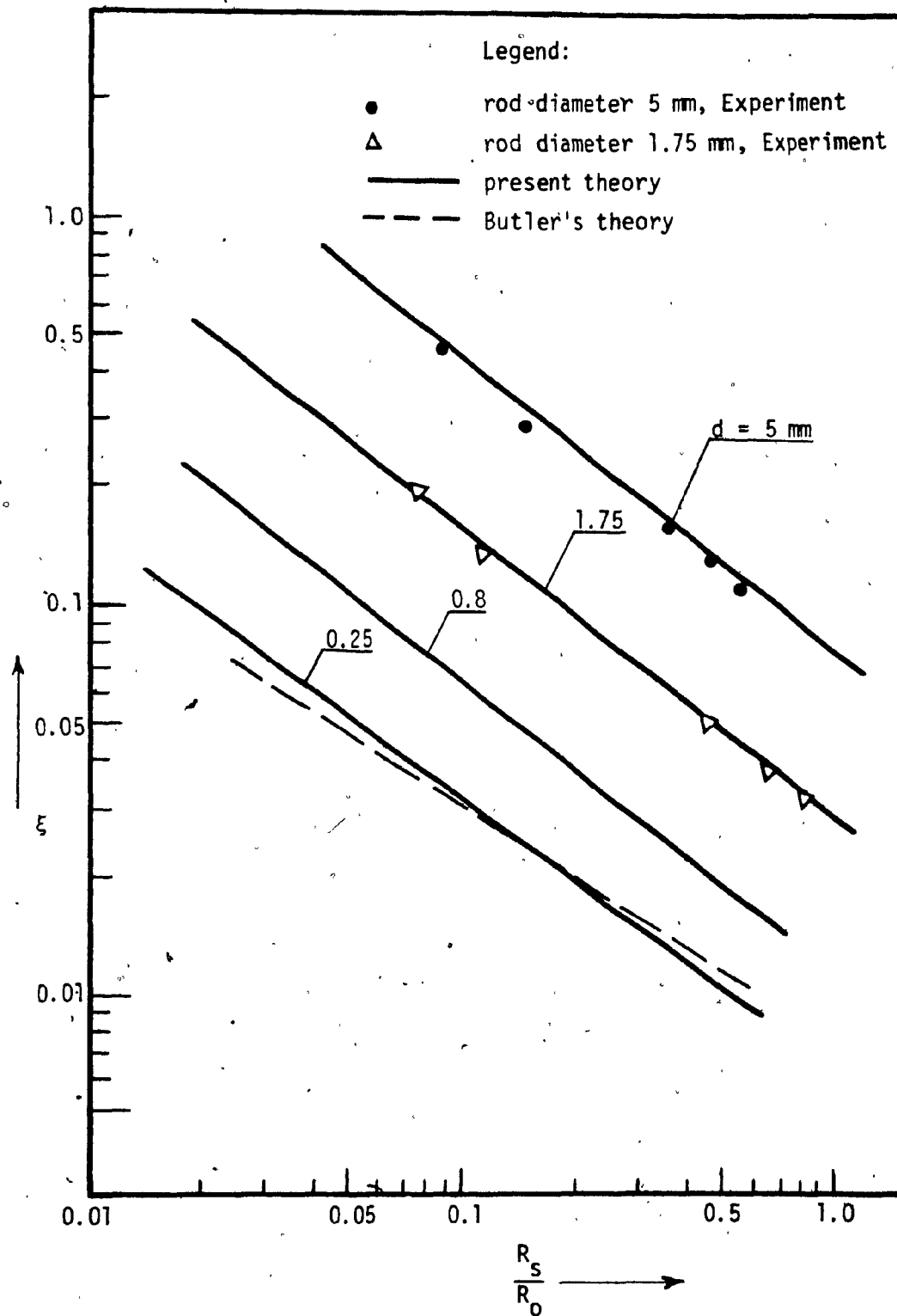
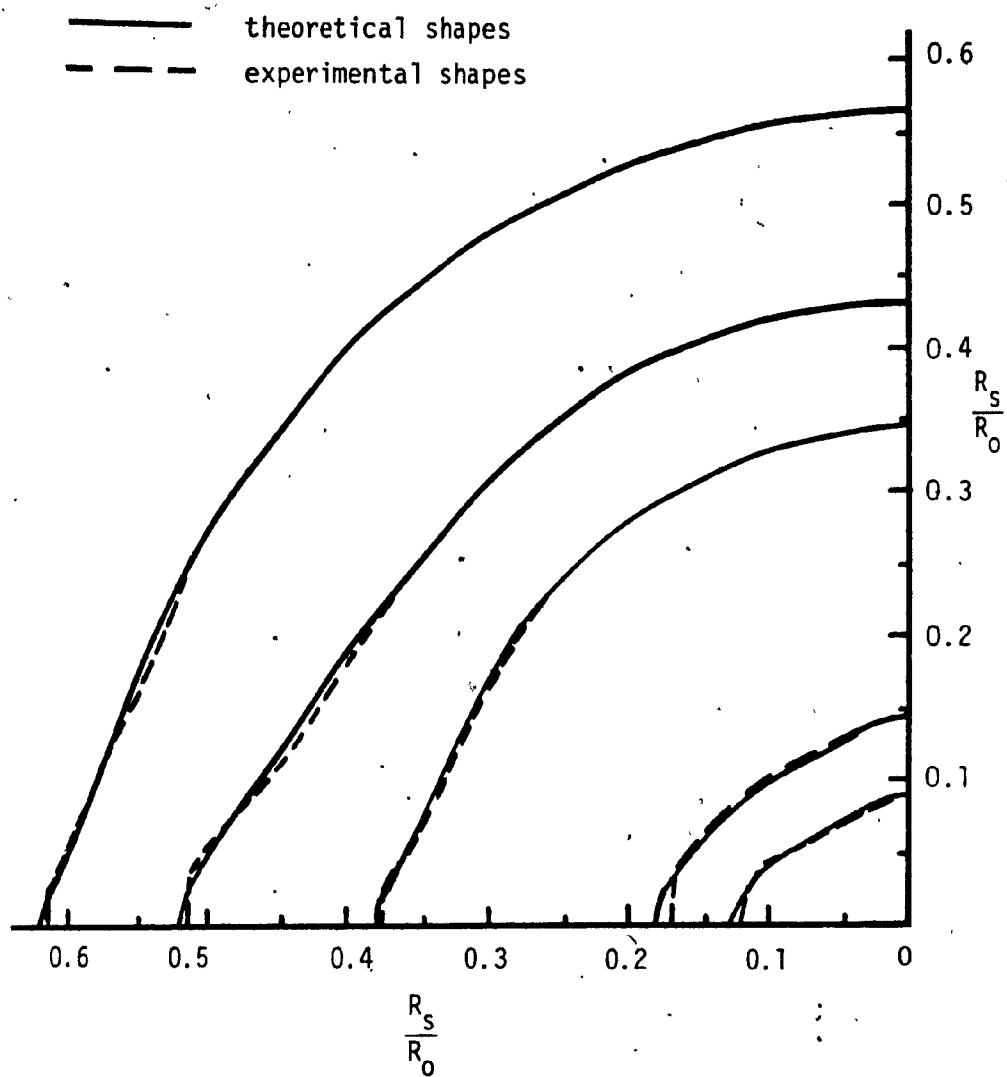
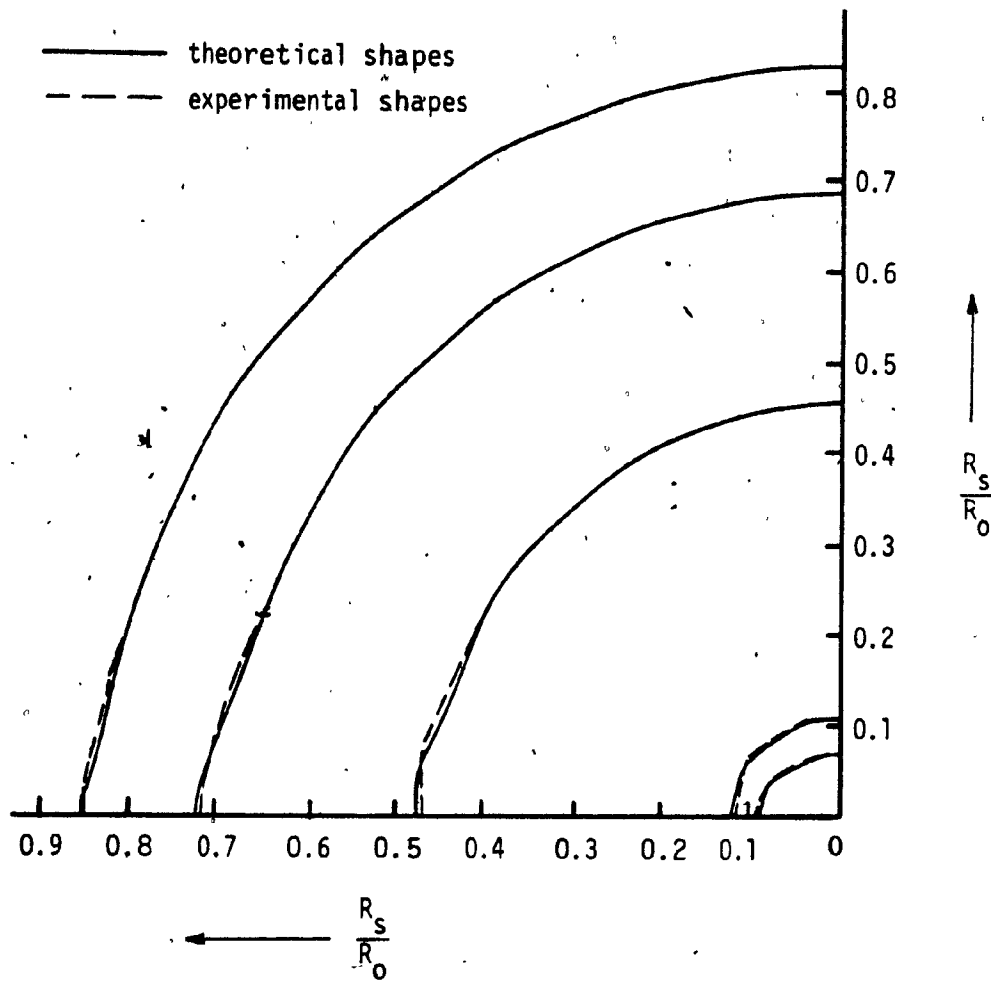


Fig. 4.16. Perturbation Growth Rate - Comparison with Butler's Small Perturbation Analysis.



a) rod diameter = 5 mm

Fig. 4.17. Theoretical and Experimental Shapes of the Perturbed Cylindrical Shock Waves.



(b) rod diameter = 1.75 mm

Fig. 4.17.

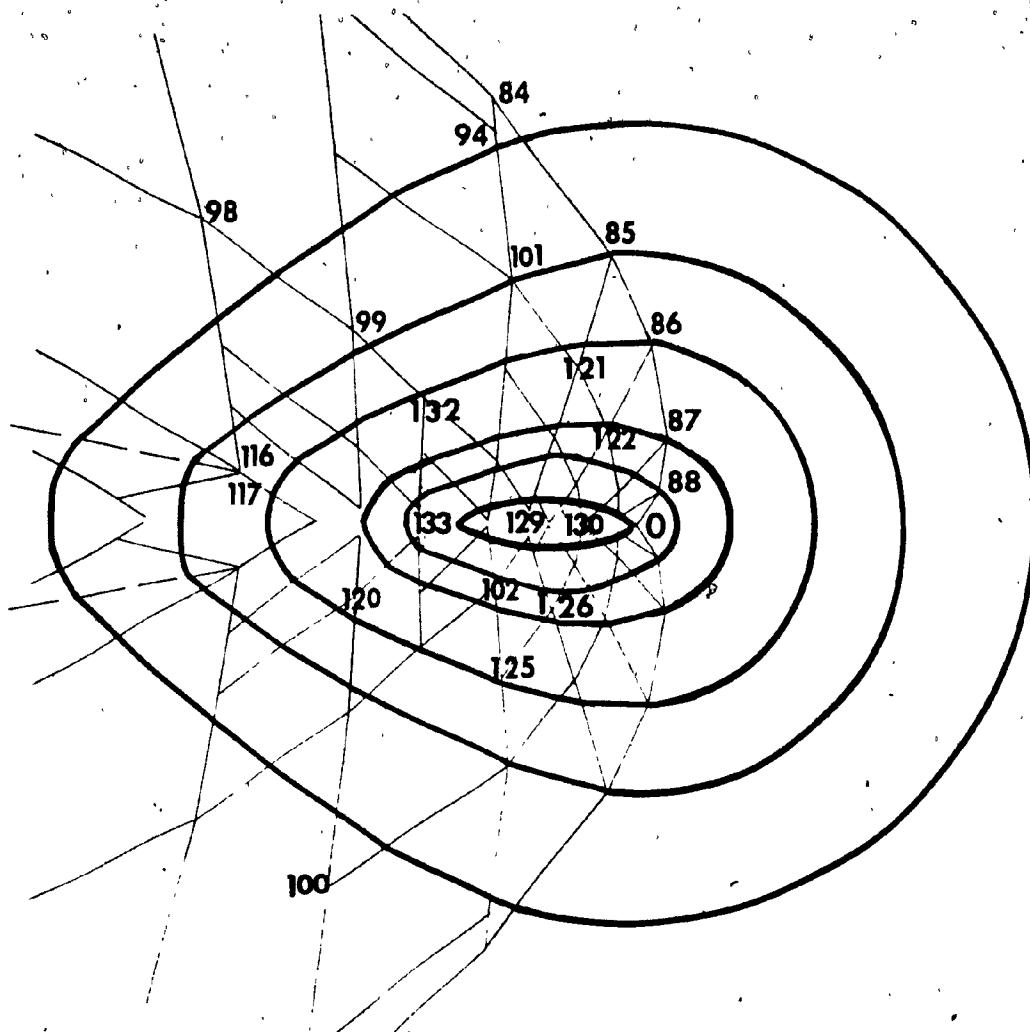


Fig. 4.18. The Collapsing of Initially Strong Cylindrical Shock Perturbed by a Rod of Diameter 5 mm.

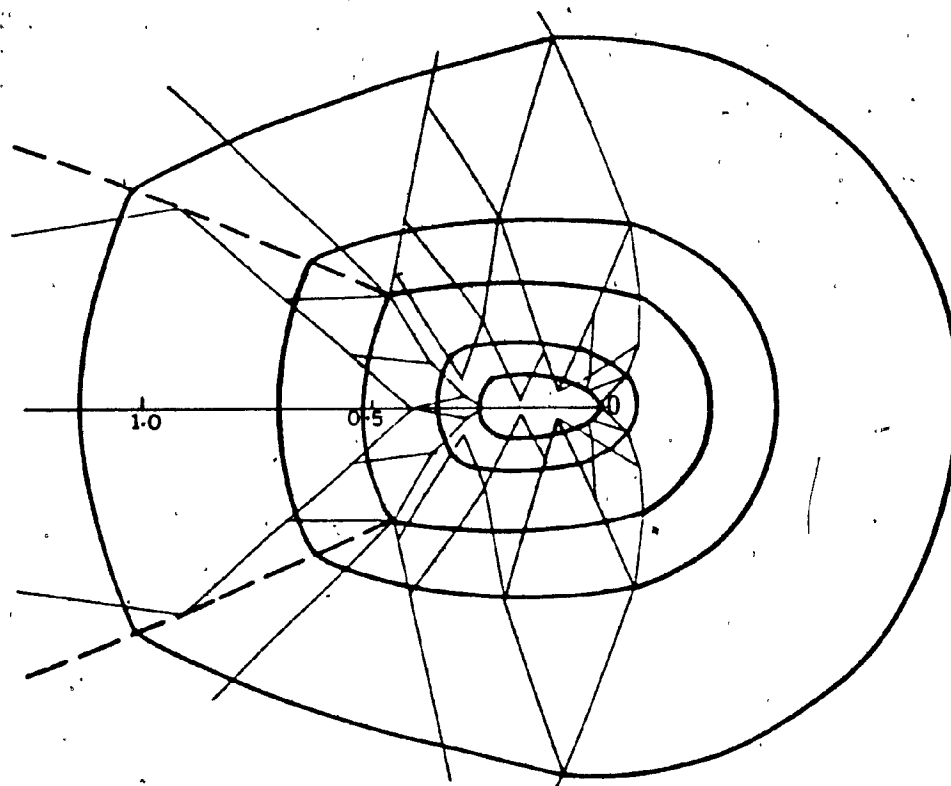


Fig. 4.19. The Collapsing of Initially Strong Cylindrical Shock Perturbed by a Rod of Diameter 1.75 mm.

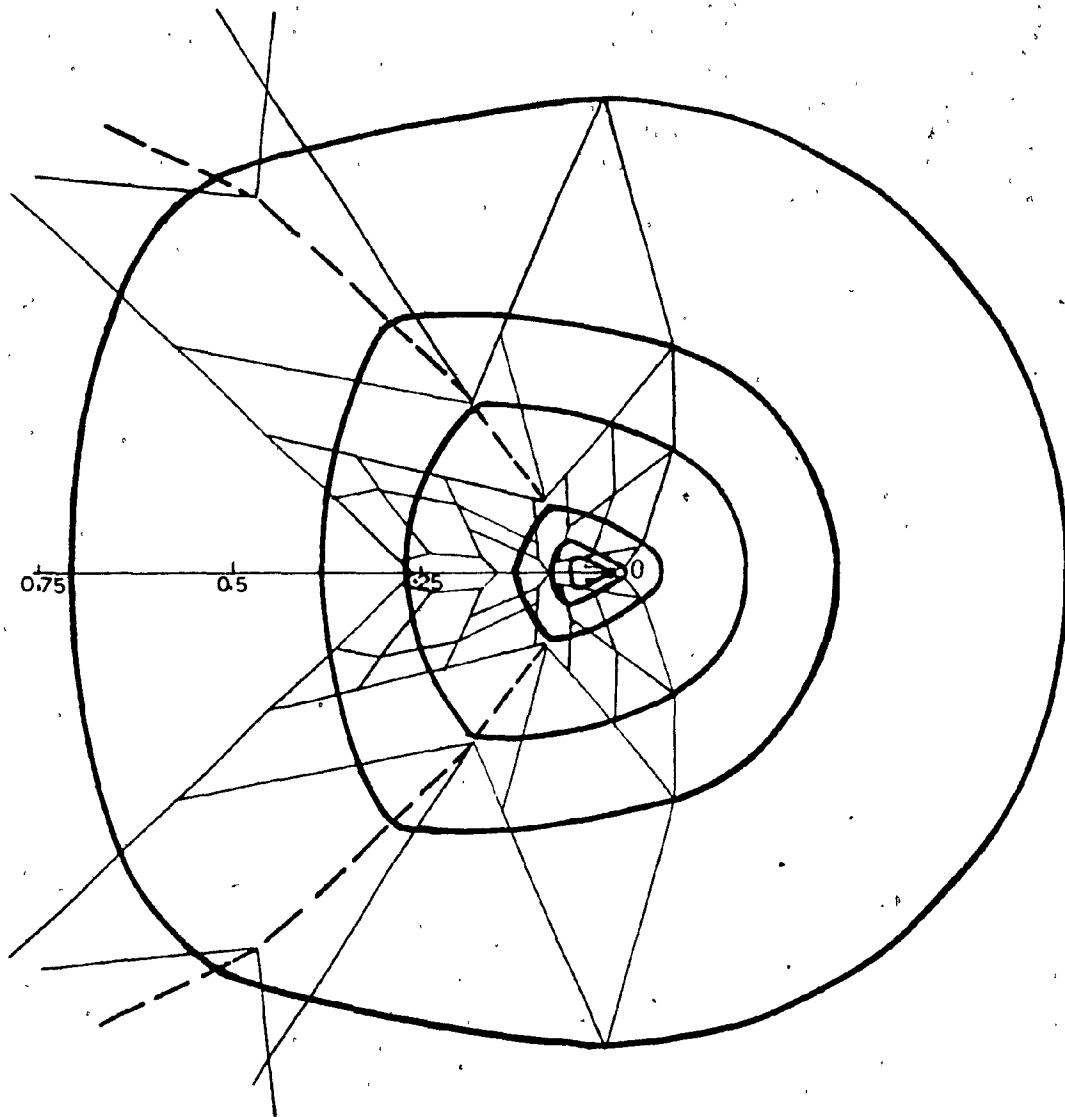


Fig. 4.20. The Collapsing of Initially Strong Shock Perturbed by a Cylindrical Rod of Diameter 0.8 mm.

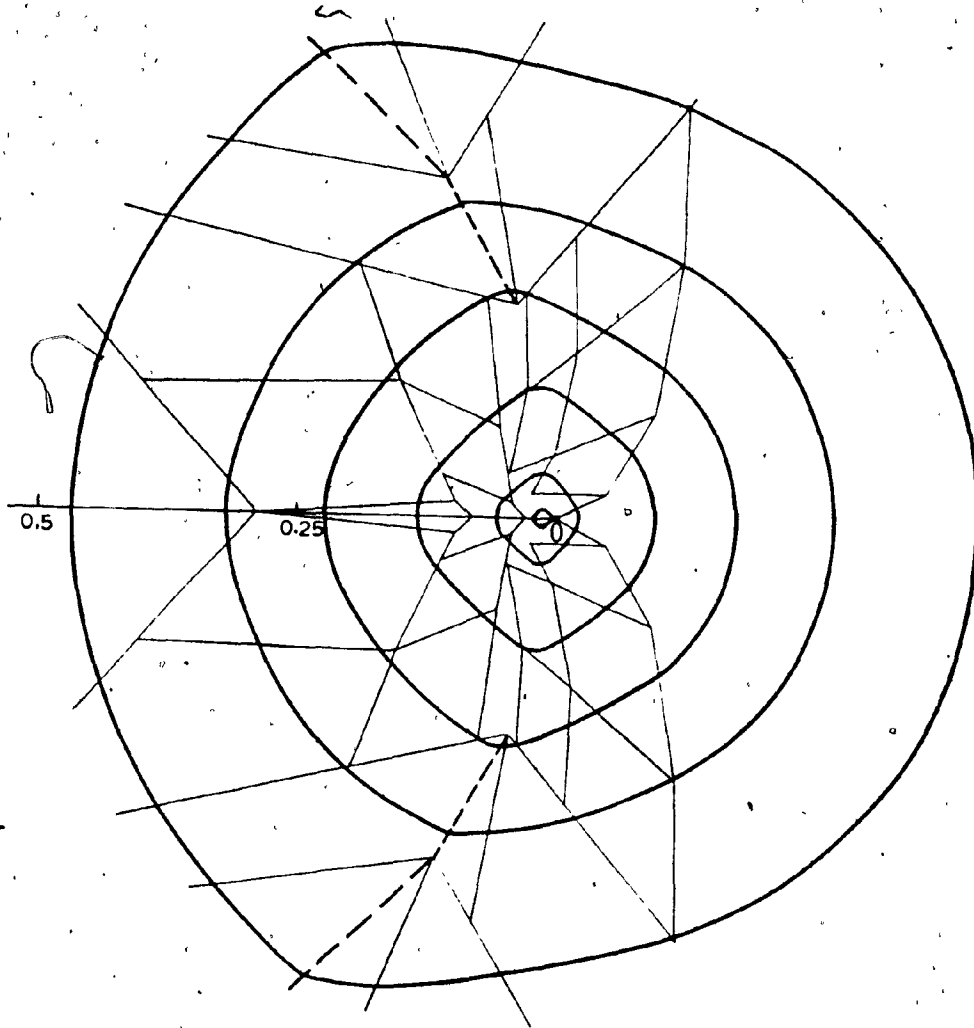


Fig. 4.21. The Collapsing of Initially Strong Cylindrical Shock Perturbed by a Rod of Diameter 0.25 mm.

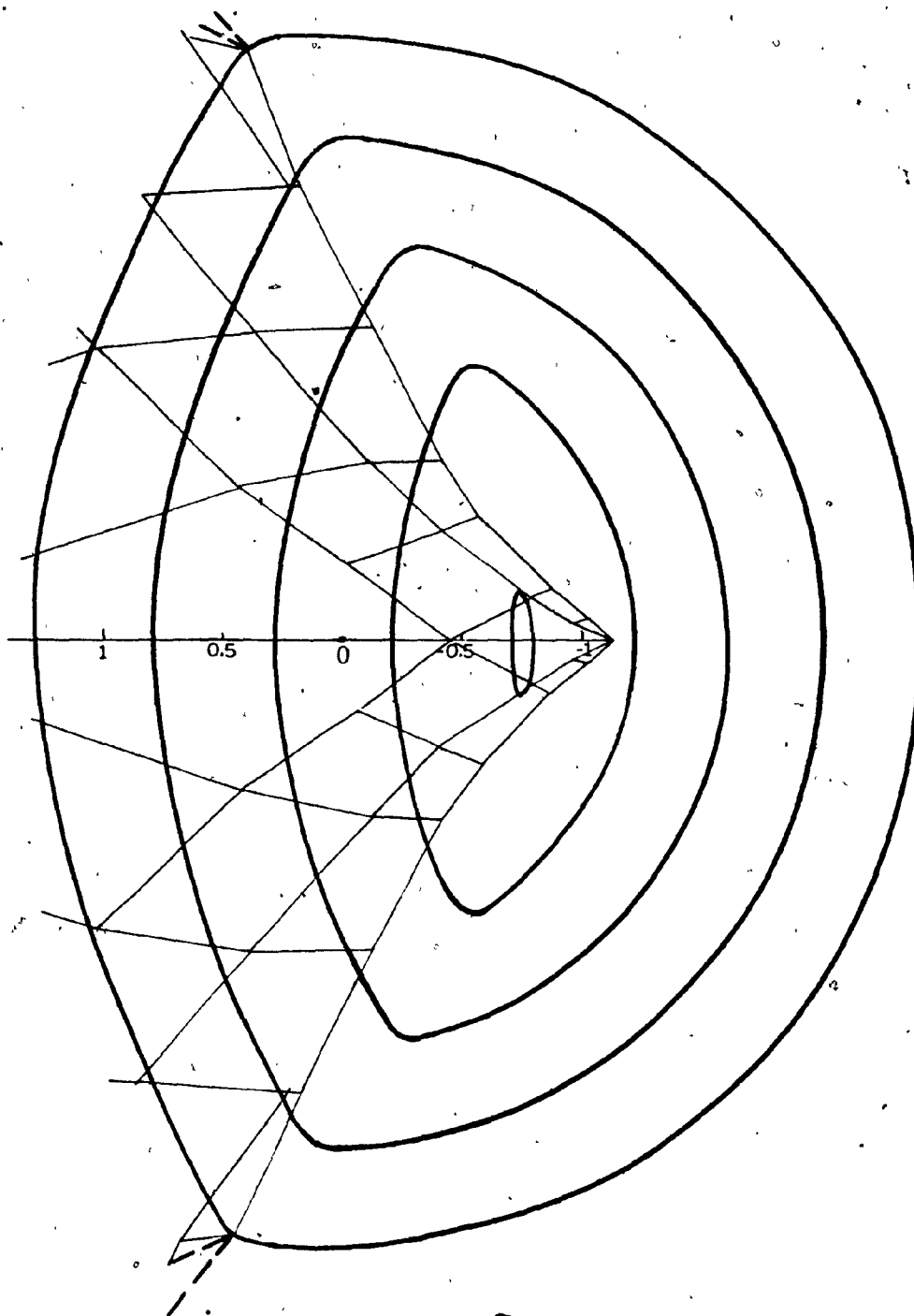


Fig. 4.22. The collapsing of Initially Weak Cylindrical Shock Wave Perturbed by a Rod of Diameter 0.25 mm.

TABLE 2.1

Mach No. 'M'	Ray Area $A \times 10^n$	w Equation (2.46)
1.00	∞	0
1.01	$3.5846 + 2$	0.283
1.05	$1.3107 + 0$	0.633
1.10	$2.9462 + 0$	0.806
1.15	$1.1841 + 0$	1.007
1.20	$6.0536 - 1$	1.266
1.25	$3.5366 - 1$	1.414
1.30	$2.2507 - 1$	1.547
1.35	$1.5206 - 1$	1.669
1.40	$1.0740 - 1$	1.728
1.45	$7.8507 - 2$	1.887
1.50	$5.8981 - 2$	1.984
1.55	$4.5319 - 2$	2.077
1.60	$3.5481 - 2$	2.165
1.65	$2.8225 - 2$	2.249
1.70	$2.2764 - 2$	2.330
1.75	$1.8580 - 2$	2.406
1.80	$1.5326 - 2$	2.480
1.85	$1.2760 - 2$	2.551
1.90	$1.0713 - 2$	2.619
1.95	$9.0632 - 3$	2.685
2.00	$7.7194 - 3$	2.749
2.05	$6.6158 - 3$	2.811
2.10	$5.7023 - 3$	2.871

Mach No. 'M'	Ray Area $A \times 10^n$	w Equation (2.46)
2.15	4.9407 - 3	2.920
2.20	4.3015 - 3	2.985
2.25	3.7617 - 3	3.010
2.30	3.3034 - 3	3.094
2.40	2.5765 - 3	3.203
2.50	2.0370 - 3	3.302
2.60	1.6300 - 3	3.388
2.70	1.3183 - 3	3.477
2.80	1.0765 - 3	3.563
2.90	8.8681 - 4	3.645
3.00	7.3630 - 4	3.724
3.20	5.1842 - 4	3.875
3.40	3.7409 - 4	4.015
3.60	2.7570 - 4	4.148
3.80	2.0696 - 4	4.272
4.00	1.5789 - 4	4.308
4.50	8.5195 - 5	4.660
5.00	4.9260 - 5	4.900
6.00	1.9213 - 5	5.314
7.00	8.7059 - 6	5.672
8.00	4.3952 - 6	5.966
9.00	2.4032 - 6	6.232

Mach No. M	Ray Area $A \times 10^n$	w Equation (2.46)
10.00	1.4070 - 6	6.470
15.00	1.7863 - 7	7.385
20.00	4.1414 - 8	8.033
100.00	1.1724 - 11	11.670
∞	0	∞

TABLE 2.2

Mach No. 'M'	Characteristic Angle 'm' (degrees) Equation (2.47)	Characteristic Angle 'm' (degrees) Equation (2.48)
1.00	0.000	0.000
1.01	4.002	7.925
1.05	8.544	16.323
1.10	11.474	21.071
1.15	13.142	23.787
1.20	14.843	25.512
1.25	15.958	26.656
1.30	16.859	27.429
1.35	17.604	27.952
1.40	18.231	28.298
1.45	18.766	28.517
1.50	19.228	28.644
1.55	19.630	28.701
1.60	19.983	28.707
1.65	20.295	28.674
1.70	20.572	28.612
1.75	20.820	28.528
1.80	21.042	28.428
1.85	21.242	28.316
1.90	21.423	28.195
1.95	21.587	28.068
2.00	21.736	27.938
2.05	21.872	27.805

Mach No. 'M'	Characteristic Angle 'm' (degrees) Equation (2.47)	Characteristic Angle 'm' (degrees) Equation (2.48)
2.10	21.997	27.672
2.15	22.111	27.538
2.20	22.216	27.406
2.25	22.312	27.275
2.30	22.401	27.146
2.40	22.560	26.895
2.50	22.696	26.656
2.60	22.814	26.429
2.70	22.916	26.214
2.80	23.006	26.012
2.90	23.085	25.822
3.00	23.154	25.643
3.20	23.271	25.318
3.40	23.364	25.033
3.60	23.439	24.781
3.80	23.501	24.559
4.00	23.552	24.363
4.50	23.647	23.963
5.00	23.710	23.731
6.00	23.788	23.704
7.00	23.832	23.702
8.00	23.859	23.702

Mach No. 'M'	Characteristic Angle 'm' (degrees) Equation (2.47)	Characteristic Angle 'm' (degrees) Equation (2.48)
9.00	23.876	23.701
10.00	23.889	23.700
15.00	23.917	23.704
20.00	23.926	23.708
100.00	23.937	23.803
∞	23.938	23.900

TABLE 4.1

$M_o = 3.0^\circ$
 $d = 5 \text{ mm}$

Points	$(\theta + \omega)$	$(\theta - \omega)$	θ°	ω	M	$(\theta + m)$	$(\theta - m)$	X_h
1	3.677	-3.784	-3.04	3.731	3.010	20.10	-26.14	
2	3.665	-3.812	-4.22	3.739	3.020	18.93	-27.37	38.00
3	3.662	-3.827	-4.74	3.745	3.028	18.41	-27.89	35.75
4	4.880	-3.833	30.00	4.357	3.930	53.50	6.50	
5	3.662	-3.840	-5.11	3.751	3.036	18.04	-28.25	32.40
6	4.665	-3.832	23.90	4.250	3.764	47.50	0.40	
7	3.655	-3.855	-5.73	3.755	3.041	17.40	-28.83	32.00
8	4.660	-3.846	23.27	4.253	3.769	46.77	-0.20	
9	3.942	-3.846	3.00	3.890	3.210	26.27	-20.27	
10	3.614	-3.841	-6.52	3.728	3.050	18.60	-29.67	28.50
11	4.512	-3.867	18.48	4.190	3.660	41.80	-4.90	
12	4.512	-3.846	19.00	4.179	3.651	42.70	-4.40	
13	3.942	-3.867	2.13	3.904	3.300	25.43	-21.20	
14	2.645	-3.867	-35.00	3.256	3.770	-12.30	-57.70	

Points	($\theta + w$)	($\theta - w$)	θ°	w	M	($\theta + m$)	($\theta - m$)	X_h
15	3.641	-3.917	-7.90	3.779	3.073	15.25	-31.05	24.60
16	4.315	-3.892	12.10	4.104	3.533	35.40	-11.40	
17	4.315	-3.867	12.80	4.138	3.570	36.20	-10.60	
18	3.942	-3.892	1.54	3.915	3.300	24.80	-21.80	
19	3.619	-4.010	-11.20	3.814	3.120	12.00	-34.36	19.80
20	4.161	-3.993	4.80	4.077	3.914	28.16	-18.56	
21	4.161	-3.892	7.72	4.025	3.421	31.00	-15.64	
22	3.293	-3.867	-16.40	3.580	2.870	6.60	-39.40	
23	3.293	-3.892	-17.16	3.590	2.810	5.80	-40.16	
24	3.293	-3.993	-20.00	3.643	2.900	3.10	-43.10	
25	3.595	-4.216	-17.80	3.905	3.241	5.40	-41.00	15.27
26	4.018	-4.221	-5.80	4.124	3.565	17.80	-29.30	
27	4.041	-3.993	0.70	4.005	3.399	24.00	-22.60	
28	2.645	-3.892	-35.70	3.268	2.477	-13.12	-58.30	
29	2.645	-3.993	-38.60	3.319	2.543	-15.80	-61.40	
30	2.645	-3.879	-35.36	3.262	2.475	-12.76	-57.96	
31	1.435	-3.879	-70.00	2.657	1.945	-48.50	-91.50	

Points	($\theta + w$)	($\theta - w$)	θ°	w	M	($\theta + m$)	($\theta - m$)	x_h
32	1.435	-3.892	-70.38	2.663	1.950	-48.80	-91.88	
33	2.306	-3.892	-45.40	3.099	2.310	-23.00	-67.80	
34	2.645	-3.945	-37.26	3.295	2.485	-14.76	-59.70	
35	2.306	-3.945	-46.90	3.122	2.340	-24.40	-69.40	
36	2.282	-3.957	-48.00	3.120	2.340	-24.84	-71.16	
37	3.293	-4.221	-26.58	3.757	3.063	-3.38	-49.78	
38	3.928	-4.221	-8.37	4.074	3.492	15.02	-32.70	
39	3.698	-4.594	-25.67	4.146	3.388	0.50	-23.80	2.33
40	3.928	-4.440	-14.67	4.184	3.659	8.73	-38.07	
41	3.513	-4.440	-26.55	3.977	3.200	-3.31	-49.75	
42	3.892	-4.440	-15.70	4.166	3.650	7.78	-39.20	
43	3.553	-4.580	-29.40	4.067	3.479	-6.10	-62.70	-2.30
44	3.892	-4.569	-19.40	4.230	3.733	4.10	-42.90	
45	3.513	-4.569	-30.25	4.031	3.470	-6.95	-53.55	
46	2.522	-3.945	-40.70	3.230	2.480	-18.23	-63.20	
47	2.522	-3.993	-42.10	3.257	2.460	-19.50	-64.70	3.90
48	4.044	-4.044	0.00	4.044	3.444	23.30	-23.30	

Points	($\theta + w$)	($\theta - w$)	θ°	w	M	($\theta + m$)	($\theta - m$)	x_h
49	3.293	-4.044	-21.83	3.670	2.943	1.30	-44.90	5.80
50	2.645	-4.044	-40.00	3.344	2.550	-17.00	-63.00	
51	4.094	-4.094	00.00	4.094	3.510	23.30	-23.30	
52	3.293	-4.086	-22.72	3.689	2.951	0.40	-45.80	
53	2.715	-4.044	-38.80	3.366	2.589	-9.00	-68.60	5.80
54	2.715	-4.086	-39.20	3.400	2.614	-16.40	-62.00	
55	4.079	-4.121	-1.20	4.100	3.528	22.10	-24.50	
56	4.121	-4.121	00.00	4.121	3.530	23.40	-23.40	
57	3.293	-4.148	-24.30	3.724	3.000	-1.20	-47.40	6.00
58	2.839	-4.086	-35.70	3.462	2.684	-12.70	-58.70	
59	2.839	-4.148	-37.50	3.493	2.710	-14.50	-60.50	
60	4.120	-4.125	-0.50	4.134	3.570	22.50	-23.50	
61	4.125	-4.125	0.00	4.125	3.550	23.50	-23.50	6.00
62	3.066	-4.148	-30.90	3.607	2.850	-7.90	-53.90	
63	3.066	-4.221	-33.00	3.643	2.900	-10.00	-56.00	
64	3.179	-4.221	-29.83	3.700	2.962	-6.80	-52.80	
65	3.179	-4.440	-36.10	3.810	3.050	-13.10	-59.20	

Points	($\theta + w$)	($\theta - w$)	θ°	w	M	($\theta + m$)	($\theta - m$)	x_h
66	2.973	-4.148	-33.60	3.559	2.787	-10.60	-56.60	
67	3.179	-4.265	-31.10	3.721	2.999	-8.00	-54.10	
68	2.973	-4.265	-37.00	3.619	2.840	-14.00	-60.00	
69	4.126	-4.231	-3.00	4.179	3.650	20.40	-26.40	
70	4.231	-4.231	0.00	4.231	3.710	23.50	-23.50	
71	3.179	-4.569	-39.80	3.864	3.200	-16.60	-63.00	
72	3.091	-4.205	-31.90	3.643	2.901	-8.90	-54.90	
73	3.091	-4.440	-38.10	3.765	3.055	-15.50	-61.70	
74	4.240	-4.438	-5.60	4.341	3.920	17.90	-28.90	
75	4.438	-4.438	0.00	4.438	4.210	23.50	-23.50	
76	3.146	-4.440	-37.00	3.791	3.090	-13.90	-60.10	
77	3.141	-4.569	-40.70	3.857	3.176	-17.50	-64.20	-1.40
78	4.290	-4.433	-8.20	4.433	4.073	15.20	-31.50	
79	4.290	-4.438	-4.23	4.364	3.950	19.10	-27.63	
80	3.554	-4.779	-35.10	4.166	3.630	-12.70	-58.50	
81	3.554	-5.030	-42.30	4.292	3.832	-18.80	-65.80	
82	3.554	-5.423	-53.56	4.488	4.173	-30.00	-77.10	

Points	($\theta + w$)	($\theta - w$)	θ°	w	M	($\theta + m$)	($\theta - m$)	x_h
83	3.554	-5.663	-60.40	4.608	4.401	-36.80	-84.00	
84	3.554	-6.016	-70.50	4.785	4.762	-46.90	-94.10	
85	3.554	-6.506	-84.58	5.030	5.315	-60.80	-108.20	
86	3.554	-6.872	-95.06	5.213	5.756	-71.30	-118.70	
87	3.554	-7.479	-112.45	5.516	6.566	-88.60	-136.20	
88	3.554	-7.931	-125.40	5.742	7.197	-101.60	-149.20	
89	3.702	-4.569	-24.80	4.136	3.570	-1.40	-48.20	
90	3.702	-4.779	-30.80	4.241	3.720	-7.43	-54.20	
91	3.702	-5.030	-38.03	4.366	3.930	-14.50	-61.50	
92	3.702	-5.423	-49.30	4.563	4.280	-25.70	-72.90	
93	3.702	-5.663	-56.15	4.682	4.510	-32.50	-79.70	
94	3.702	-6.016	-66.20	4.859	4.700	-42.56	-66.20	
95	3.702	-6.506	-80.32	5.104	5.200	-56.60	-104.00	
96	3.513	-4.779	-36.20	4.146	3.590	-12.80	-59.60	
97	3.513	-5.030	-43.45	4.272	3.800	-19.90	-66.90	
98	3.513	-5.423	-54.70	4.468	4.330	-31.10	-78.30	
99	3.513	-5.663	-61.57	4.588	4.400	-38.00	-85.20	

Points	($\theta + w$)	($\theta - w$)	θ°	w	M	($\theta + m$)	($\theta - m$)	X_h
100	3.608	-5.662	-58.80	4.635	4.410	-35.20	-82.40	
101	3.608	-6.016	-68.97	4.812	4.698	-45.20	-92.60	
102	3.513	-6.016	-71.70	4.764	4.695	-47.90	-95.30	
104	3.206	-4.779	-44.50	4.001	3.380	-21.20	-67.80	-4.50
105	4.412	-4.778	-10.50	4.595	4.377	13.10	-34.10	
106	4.412	-4.438	-0.80	4.425	4.198	22.70	-24.30	
107	4.778	-4.778	0.00	4.778	4.700	23.60	-23.60	
108	3.360	-4.779	-40.64	4.069	3.480	-17.34	-63.90	
109	3.360	-5.030	-47.85	4.195	3.680	-24.40	-71.25	
110	3.278	-4.779	-43.00	4.028	3.410	-19.70	-66.30	
111	3.278	-5.030	-50.20	4.154	3.591	-26.80	-73.60	-8.70
112	4.604	-5.030	-12.20	4.817	4.828	11.50	-35.80	
113	4.604	-4.778	-4.98	4.691	4.510	18.62	-28.58	
114	5.030	-5.030	00.00	5.030	5.300	23.70	-23.70	
115	3.349	-5.030	-48.17	4.189	3.650	-24.70	-71.50	
116	3.360	-5.423	-59.10	4.391	3.989	-35.60	-82.60	-13.40
117	4.910	-5.472	-16.10	5.191	5.704	7.60	-39.80	

Points	($\theta + w$)	($\theta - w$)	θ°	w	M	($\theta + m$)	($\theta - m$)	x_h
118	4.910	-5.030	-3.46	4.970	5.290	20.20	-27.16	
119	3.436	-5.424	-56.90	4.430	4.150	-33.30	-80.50	
121	3.608	-6.506	-83.03	5.057	5.150	-59.33	-106.73	
122	3.608	-6.872	-93.50	5.240	5.831	-69.70	-117.30	
123	3.608	-7.479	-110.90	5.543	6.552	-87.10	-134.70	
124	3.608	-7.931	-123.80	5.769	7.330	-100.00	-147.60	
125	3.561	-6.016	-70.30	4.788	4.750	-46.60	-94.00	
126	3.561	-6.506	-84.30	5.033	5.242	-60.60	-108.00	
127	3.561	-6.872	-94.80	5.216	5.810	-71.00	-118.60	
128	3.561	-7.479	-112.20	5.520	6.480	-88.40	-136.00	
129	3.513	-6.506	-85.70	5.010	5.120	-62.00	-109.40	
130	3.525	-6.506	-85.40	5.016	5.141	-61.70	-108.70	
131	3.525	-6.872	-95.80	5.198	5.698	-72.10	-119.50	
132	3.513	-5.839	-66.63	4.676	4.504	-43.06	-90.20	
133	3.437	-5.839	-68.80	4.638	4.452	-45.20	-92.40	
134	3.475	-5.839	-67.72	4.657	4.472	-44.12	-91.32	
135	3.475	-6.016	-72.78	4.745	4.710	-49.00	-96.50	

Points	($\theta + w$)	($\theta - w$)	θ°	w	M	($\theta + m$)	($\theta - m$)	x_h
136	3.398	-5.423	-58.10	4.411	4.150	-34.40	-81.60	
137	3.398	-5.663	-64.86	4.530	4.250	-41.20	-88.40	
138	5.472	-5.472	0.00	5.472	6.420	23.80	-23.80	